INVESTIGATION OF PLASMA DEPOSITED HEXAGONAL BORON NITRIDE THIN FILMS

A THESIS SUBMITTED TO
THE GRADUATE SCHOOL OF NATURAL AND APPLIED SCIENCES
OF
MIDDLE EAST TECHNICAL UNIVERSITY

BY

MUSTAFA ANUTGAN

IN PARTIAL FULFILLMENT OF THE REQUIREMENTS
FOR
THE DEGREE OF MASTER OF SCIENCE
IN
PHYSICS

JULY 2007

Approval of the Thesis

"INVESTIGATION OF PLASMA DEPOSITED HEXAGONAL BORON NITRIDE THIN FILMS"

Submitted by **MUSTAFA ANUTGAN** in partial fulfillment of the requirements for the degree of **Master of Science in Physics** by,

Prof. Dr. Canan Özgen
Dean, Graduate School of **Natural and Applied Sciences** _____

Prof. Dr. Sinan Bilikmen
Head of Department, **Physics** _____

Prof. Dr. Bayram Katırcıoğlu
Supervisor, **Physics, METU** _____

Examining Committee Members:

Assoc. Prof. Dr. İsmail Atılgan (*)
Physics, METU _____

Prof. Dr. Bayram Katırcıoğlu (**)
Physics, METU _____

Assist. Prof. Dr. Sadi Turgut
Physics, METU _____

Assist. Prof. Dr. Hüseyin Sarı
Physics Engineering, Ankara University _____

Assist. Prof. Dr. Barış Akaoğlu
Physics, Gazi University _____

Date: _____

(*) Head of Examining Committee
(**) Supervisor

I hereby declare that all information in this document has been obtained and presented in accordance with academic rules and ethical conduct. I also declare that, as required by these rules and conduct, I have fully cited and referenced all material and results that are not original to this work.

Name, Last name : Mustafa ANUTGAN

Signature :

ABSTRACT

INVESTIGATION OF PECVD DEPOSITED
HEXAGONAL BORON NITRIDE THIN FILMS

Anutgan, Mustafa
M.Sc., Department of Physics
Supervisor: Prof. Dr. Bayram Katırcıoğlu

July 2007, 123 pages

Hexagonal boron nitride (h-BN) thin films are deposited by plasma enhanced chemical vapor deposition (PECVD). Effects of heat treatment and source gases on the structure and physical properties are investigated. Chemical bonding is analyzed in comparison with the better understood isoelectronic carbon compound, graphite. It seems that the basic difference between h-BN and graphite arises from the different electronegativities of boron and nitrogen atoms. Optical absorptions in UV-visible range for crystalline and amorphous structures are outlined. The expressions used for the evaluation of mechanical stress induced in thin films are derived. The deposited films are considered to be turbostratic as they do not exhibit the characteristic optical absorption spectra of a crystal. A new system, stylus profilometer, is implemented and installed for thin film thickness and mechanical stress measurements. Hydrogen atom density within the films, estimated from FTIR spectroscopy, is found to be a major factor affecting the order and mechanical stress of the films. Heat treatment of the films reduces the hydrogen content, does not affect the optical gap and slightly increases the Urbach energy probably due to an increased disorder. Increasing the nitrogen gas flow rate in the source gas results in more ordered films. The virtual crystal of these films is detected to be unique. Relative bond concentrations of the

constituent elements indicate a ternary boron-oxygen-nitrogen structure. The physical properties of h-BN such as high resistivity and wide band gap seem suitable for optoelectronic applications such as gate dielectrics in thin film transistors and light emitting devices in the blue region.

Keywords: turbostratic boron nitride, electronegativity, Urbach energy, virtual crystal, thin film stress.

ÖZ

PLAZMA İLE BİRİKTİRİLMİŞ HEGZAGONAL BOR NİTRÜR İNCE FİLMLERİN İNCELENMESİ

Anutgan, Mustafa
Master, Fizik Bölümü
Tez Yöneticisi: Prof. Dr. Bayram Katırcıoğlu

Temmuz 2007, 123 sayfa

Hegzagonal bor nitrür (h-BN) ince filmler plazma destekli kimyasal buhar biriktirme yöntemiyle (PECVD) büyütülmüştür. Isıl işlem ve azot kaynağının yapı ve fiziksel özellikler üzerindeki etkileri incelenmiştir. Kimyasal bağ çözümlemesi hem h-BN hem de daha iyi anlaşılmış izoelektroniği grafit üzerindeki çalışmalar ışığında yapılmıştır. h-BN ve grafit arasındaki temel farklılıkların bor ve azotun değişik elektron çekerliklerinden kaynaklandığı belirtilmiştir. Değişik yapılardaki ışığın soğurulma katsayısı ve ince filmlerdeki mekanik stres formülleri türetilmiştir. Üretilmiş filmler, kristal yapının kendine has optik soğurma tayfını sergilemediğinden, turbostratik olarak düşünülmüştür. Yeni bir ölçüm aleti, iğne ile yanay ölçer, kurulmuş ve ince filmlerin kalınlık ve mekanik streslerinin belirlenmesinde kullanılmıştır. FTIR tayf-izler ile hesaplanmış olan filmlerdeki hidrojen atom yoğunluğunun filmlerdeki düzenliliği ve mekanik stresi etkileyen temel bir faktör olduğu bulunmuştur. Üretilmiş filmlerdeki ısıl işlem hidrojen miktarını azaltmış ve bir düzensizlik parametresi olan Urbach enerjisini hafifçe yükseltmiştir; ancak yasak enerji aralığını değiştirmemiştir. Kaynak gazındaki azot gaz akım oranının arttırılması daha düzenli film oluşumunu sağlamıştır. Bu filmlerin tek bir sanal kristale sahip oldukları saptanmıştır. Mevcut elementlerin göreli bağ

yoğunlukları üçlü bor-oksijen-azot yapısının varlığına işaret etmektedir. h-BN'nin yüksek elektrik direnci ve geniş yasak enerji aralığı gibi fiziksel özellikleri ince film transistörlerde yalıtkan tabaka ve mavi ışık bölgesinde ışık yayan bileşenler gibi optoelektronik uygulamalara uygun gözükmektedir.

Anahtar kelimeler: turbostratik bor nitrür, elektron çekerlik, Urbach enerjisi, sanal kristal, ince film stresi.

To My Family

ACKNOWLEDGMENTS

First of all, I would like to thank my supervisor Prof. Dr. Bayram Katırcıoğlu for his scientific and technical guidance throughout this work.

I express my gratitude to Assoc. Prof. Dr. İsmail Atılgan as he is the technical backbone of this laboratory being able to execute all the present measurement and production units. He also directs the route of the research by his advices.

I would like to thank Scientific and Technical Research Council of Turkey (TÜBİTAK) for financial support during my academic studies.

I acknowledge Engin Özkol for his cheerful colleagueship. He also supported me with XPS data and helped me at the processing step.

I am grateful to Assist. Prof. Dr. Orhan Özdemir for his advices and critics.

I would also like to thank my sister and parents for their lifelong guidance.

Finally, I want to express thanks to my wife, Tamila Aliyeva Anutgan. This work would not be possible without her solid help and understanding both in laboratory and daily lives. She also conducted the FTIR analysis of this work.

TABLE OF CONTENTS

LIST OF TABLES

TABLES

LIST OF FIGURES

FIGURES

CHAPTER 1

INTRODUCTION

1.1 Boron Nitride Structures

The existence of stable polyatomic species (whether elemental or compound) implies that atoms can act upon each other to form aggregates which have lower potential energy than separate atoms. In other words, chemical bonds exist between atoms. Consequently, the nature of chemical bonding determines the chemical and physical properties of elements and compounds. Qualitatively an electron is shared more or less equally by a group of atoms in a bond (equal sharing for covalent bonds and unequal sharing for ionic bonds). One of the approaches for studying bonds is to consider the bonds as "molecular" orbitals which are "built" of overlapping atomic orbitals.

Although the boron atom in its normal electronic configuration has only one half filled orbital $(1s^2 2s^2 \boldsymbol{2p^1})$, the maximum possible number of partially filled orbitals is 3 $(1s^2 2s^1 2p_x^1 2p_y^1)$. Consequently, it can form three covalent bonds (e.g. BF_3) rather than one as suggested by its normal configuration. As for the nitrogen, it has 3 half filled orbitals $(1s^2 2s^2 2p^3)$, normally it is able to form three covalent bonds. Bonding electrons in atomic orbitals being not equivalently located in space, the equivalence of bonds in compounds (such as BN) is built by the hybridization of atomic orbitals. Both for boron and nitrogen, 3 equivalent (hybrid) orbitals may be obtained by combining one 2s-orbital with two 2p-orbitals (planar $2p_x$ and $2p_y$) as three sp^2 hybrid orbitals (Fig. 1.1).

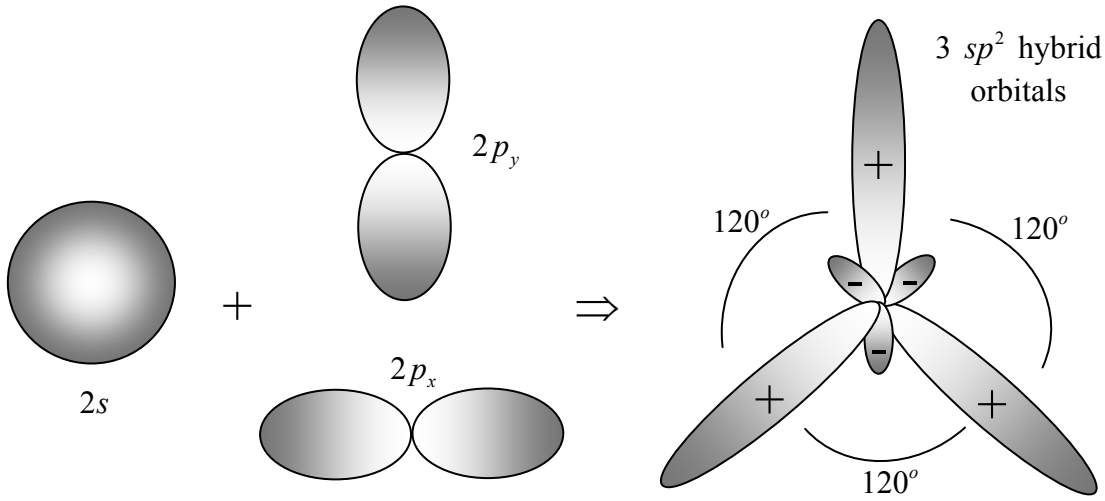

Figure 1.1: Combination of one s and two p orbitals to form three sp^2 hybrid orbitals.

Three planar sp^2-like σ bonds (with cylindrical symmetry around BN axis) are formed around each of the components (Fig. 1.2). Each of these σ bonds could not be considered as purely covalent that is, bonding electrons are not equally shared by the two components. On the contrary, in these hetero-nuclear diatomic bonds, electrons are expected to be concentrated rather towards the nitrogen atom side since atomic orbitals on the nitrogen are located relatively lower in potential energy (due to the greater nuclear charge of nitrogen) than do the atomic orbitals on the boron. In other words, the B-N bond is slightly polar $(B^{+\delta} \xleftrightarrow[d]{} N^{-\delta})$, leading to a finite dipole moment $\mu = d\delta$.

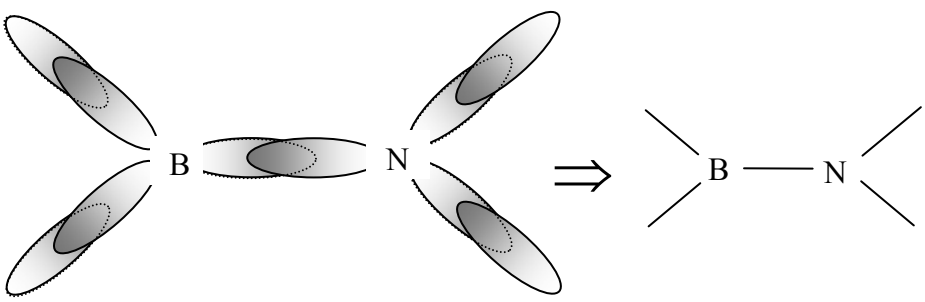

Figure 1.2: Three planar $sp^2 - \sigma$ like bonds of boron nitride and their representation.

During the formation of above described three planar sp^2-like σ bonds around each atom, an unhybridized free p_z atomic orbital remains on each component, which are perpendicular to the plane of the three sp^2 orbitals (Fig. 1.3). As stated previously, the nitrogen orbital $(p_z)_N$ is lying lower in potential energy than that of the boron $(p_z)_B$. Consequently, $(p_z)_N$ is expected to be occupied by two electrons (of opposite spin) and $(p_z)_B$ remains empty (it is assumed here that one of the $2s^2$ electrons of nitrogen atom participates in sp^2 bonding, the other is excited to $(p_z)_N$ orbital). Moreover, the lobes of $(p_z)_B$ and $(p_z)_N$ above and below the sp^2 bonds should be symmetrically cut by the plane of sp^2 bonds.

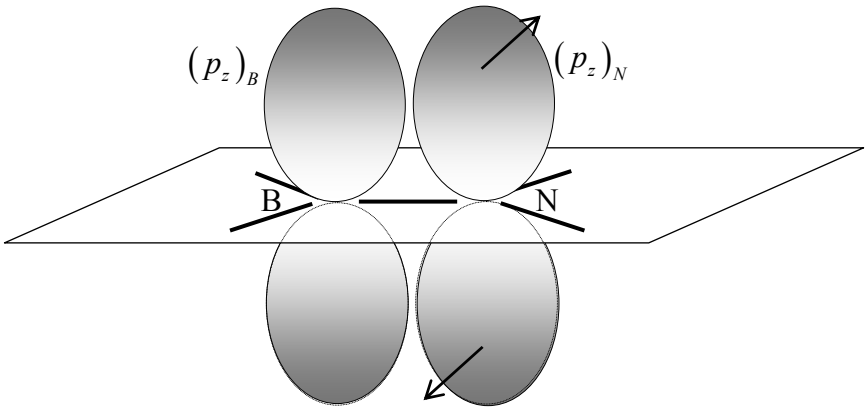

Figure 1.3: p_z orbitals are perpendicular to the plane of $sp^2-\sigma$ bonds. The interaction between neighboring p_z orbitals contributes to the planar structure.

At this stage of boron-nitrogen (B-N) bonding, it may be useful to compare this bonding with that of the carbon-carbon (C-C) bonding. The combination of B-N is isoelectronic to C-C pair (boron and nitrogen atoms are of similar atomic number, they are located on either side of the carbon in the periodic table of elements). Furthermore, the covalent radius and the electronegativity comparison locate carbon between boron and nitrogen elements (Table 1.1). (Pauling's electronegativity value, *x*, for an element is related to the average of its ionization potential energy *I* and its electron affinity χ, in eV, by the following relation: $x = 0.18(I+\chi)$).

Table 1.1: The average radii and electronegativities for boron and nitrogen are nearly the same with those for carbon thus, isoelectronic structure of carbon and boron-nitrogen compound is expected.

Element	**Electronegativity [1]**	**Covalent Radius**	**# of valence electrons**
Carbon	2.5	0.77	4
Boron	2	0.88	3
Nitrogen	3	0.7	5

The overlapping of p_z orbitals for carbon-carbon combination, shown in Fig. 1.3, forms the second bond (π bond together with the $sp^2 - \sigma$ bond, leading to the famous double bonded $(> C = C <)$ structure. The existence of double bonding in BN has been extensively discussed [2]. One might speculate as follows about double bonding of BN combination. The two $(p_z)_N$ electrons around the nitrogen as shown in Fig. 1.3 might be partially available for π-bonding, by the partial transfer of $(p_z)_N$ electrons to $(p_z)_B$ at the boron site, without totally compensating the transfer along the $sp^2 - \sigma$ bond from boron to nitrogen due to the differences in electronegativity between boron and nitrogen. However, the low magnitude of this double bond character could not seem to be comparable to that of a carbon-carbon double bond. Therefore, for a rough analysis, the sharing of nitrogen $(p_z)_N$ electron pair in the bond building remains limited and then negligible. The following figure depicts this configuration (Fig. 1.4).

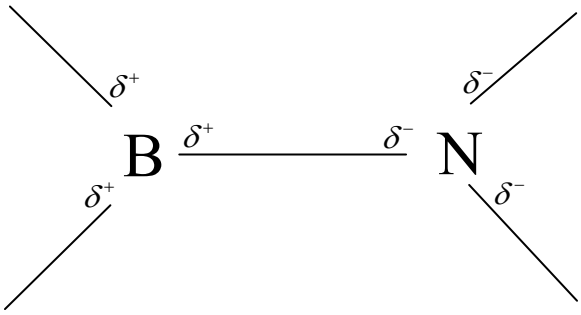

Figure 1.4: Net charge distribution around boron and nitrogen atoms as they are bonded. Nitrogen attracts electrons more due to its relatively high electronegativity and becomes negatively charged while the opposite case holds for boron atom.

Within the previously described boron-nitrogen combination where each component atom of one sort has three planar trigonal $sp^2 - \sigma$ bonds 120° apart to three atoms of second sort. The configuration may easily lead to six sided planar ring structure, reasonable due to the following two phenomena:

a. Optimization of the interactions between the lobes above and below hexagonal plane of the unhybridized $(p_z)_B$ and $(p_z)_N$ orbitals (Fig. 1.3).

b. Tendency to cancel the total dipole moment although B-N bond is polar (Fig. 1.5)

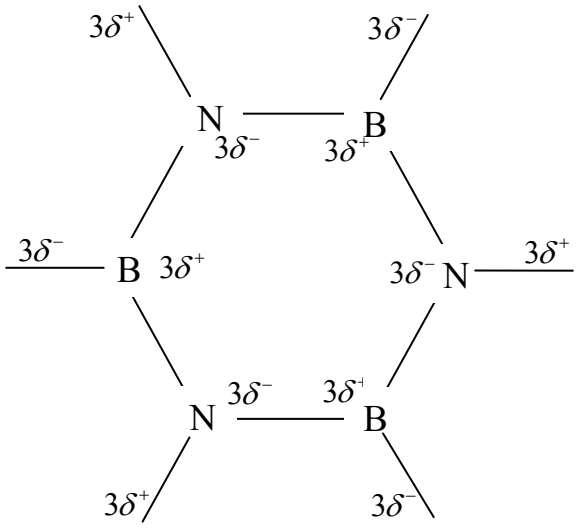

Figure 1.5: Total dipole moment in the sp^2 bonding configuration is expected to be zero at each site if the σ bonds are planar and 120° apart from the neighboring ones.

The above described hexagonal structure has the obvious ability to be arranged into a three $sp^2 - \sigma$ like coordinated hexagonal 2-dimensional infinite layers. These six-fold B_3N_3 rings of a giant planar molecule are held together by weak van der Waals or dipolar interaction. In other words, this interaction might be interpreted as a secondary weak bond between the hexagonal planes. As depicted in Fig. 1.6a, these hexagons are packed directly on top of each other where a boron atom in one layer remains closest to each corresponding nitrogen atom in the neighboring layers with ABAB… sequence of planes. However, omitting the diatomic structure, sequence of hexagonal lattice is as AAAA…, exhibiting the second difference apart from the polarity of bonds from the packing of graphite where the hexagons are shifted by one bond length along the neighboring planes and leading to ABAB… sequence.

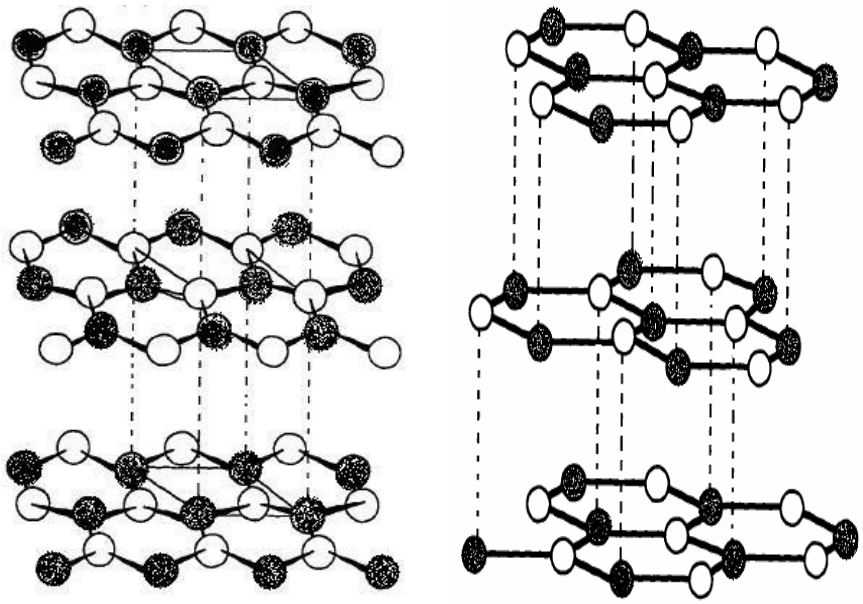

(a) (b)

Figure 1.6: sp^2 bonded layer structure of (a) hexagonal BN of ABAB… sequence along c-axis and (b) rhombohedral BN of ABCABC… sequence.

The analysis so far establishes the theoretical basis of hexagonal boron nitride (h-BN) crystals. Experiments have carried out indicate that h-BN is the only stable

phase found in nature. On the other hand, the above described hexagonal structure is not the only symmetry of boron nitride. This crystalline BN solid can have (more or less stable) different microscopic arrangement (it is polymorphous or allotrope). For example, rhombohedral (r-BN) symmetry is obtained from ABCABC… sequence of hexagonal planes with $sp^2 - \sigma$ like trigonal bonding (Fig. 1.6b). Rhombohedral structure is thermodynamically unstable and can be considered as an extended stacking fault of hexagonal structure. It is not found in pure form but rather in combination with hexagonal structure.

Another stable form of BN crystal is the cubic structure which may be converted from the h-BN crystals by heat treatments. In this arrangement, the components boron and nitrogen supply 8 valence electrons which are hybridized from the linear combination of $2s^1 2p_x^1 2p_y^1 2p_z^1$ atomic orbitals of both B and N atoms into 4 sp^3 identical orbitals equivalently located in space around each component; these hybrid orbitals from one component form σ-like tetrahedral bonds with the four neighboring second component (Fig. 1.7a). This cubic arrangement requires exceptional laboratory conditions to be produced as one might realize from the above description of $sp^3 - \sigma$ like bond formation. In spite of fabrication difficulty, this cubic form renders BN one of the most interesting candidates for hard and protective coating applications since its hardness approaches that of diamond [3].

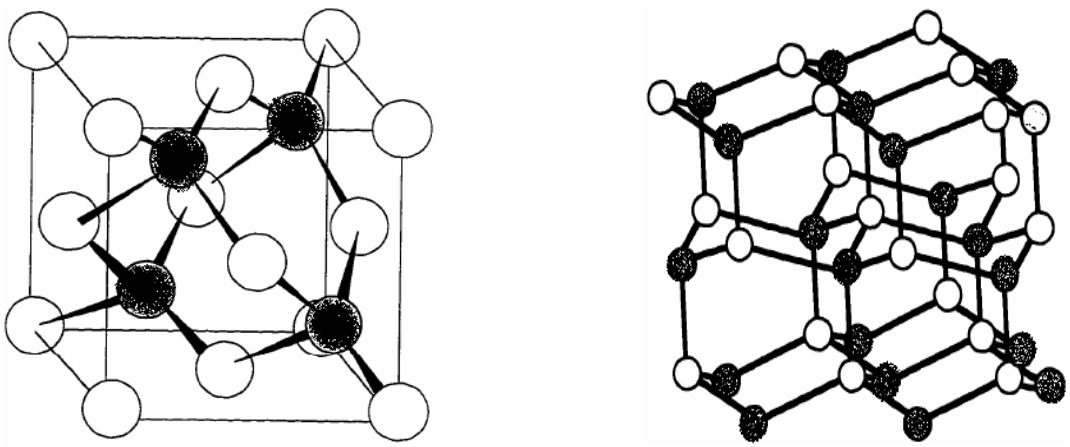

(a) (b)

Figure 1.7: sp^3 bonded symmetries of (a) cubic and (b) wurtzite BN.

Next form of BN symmetry is the wurtzite structure (w-BN) which is a metastable version of cubic phase. It may be considered as two interpenetrating hexagonal structures leading to tetrahedral ($sp^3-\sigma$ like) coordination such that each component is surrounded by 4 equivalently located neighbors of second sort (Fig. 1.7b). In this respect, one should keep in mind that the zinc blende type c-BN is obtained by two interpenetrating face centered cubic structures of each component supplying the tetrahedral $sp^3-\sigma$ like bonding.

Apart from the above presented single crystalline forms of BN compound, various polycrystalline (or microcrystalline or nanocrystalline) forms might exist. In this respect, the qualification turbostratic is commonly used. Aggregates of hexagonal crystallites of distributed sizes constitute the material. Each crystallite may be more or less perfect; most of them may contain a varying number of defects such as vacancies or dangling bonds, cavities and other imperfections. This porous structure is ready to receive impurities such as hydrogen, oxygen, etc.

When BN material is produced in thin film form, a disordered turbostratic structure is produced [4]. Relatively far from the substrate, these $sp^2-\sigma$ bonded hexagonal BN planar crystallites, which are relatively defect free, can have random orientations (i.e. rotated more or less around c-axis which is perpendicular to the hexagonal plane). These layers of planar hexagonal grains may not be perfectly parallel to each other and the ABAB… sequence of layers might be no longer maintained. However, the "grain" boundary regions might be extremely defective (a typical diagram depicting the turbostratic structure is given in Fig. 1.8).

The degree of porosity and contamination by impurities may, of course, depend on the production conditions and surrounding and then the resulting physical properties are affected. At the extreme limit, this turbostratic structure may be qualified as "amorphous" where almost only short range order might exist. During the film growth, at the initial stage, due to mainly the effects of substrate surface, the first layer on the substrate of thickness 2-4 nm may be amorphous. This layer might

contain defects of all sorts leading to a huge density of electronic states which are expected to be distributed from valence band to the conduction band.

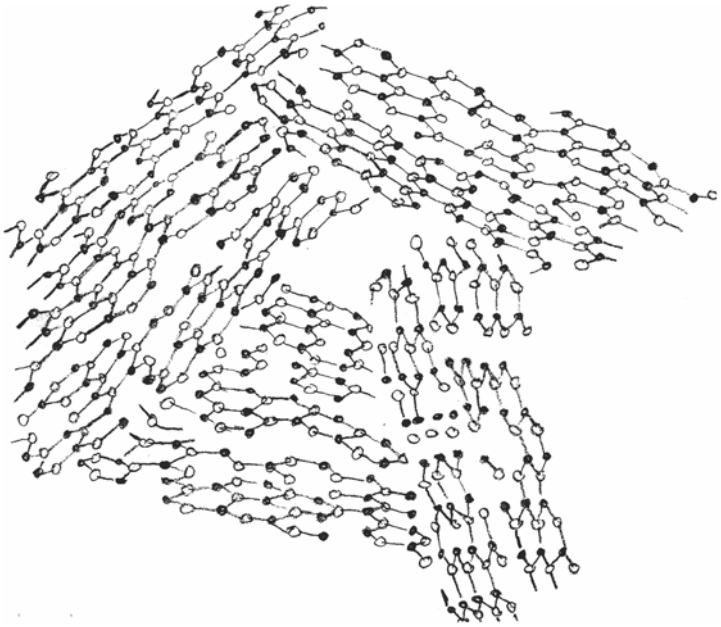

Figure 1.8: Turbostratic (disordered) hexagonal (sp^2) structure.

The three dimensional tight-binding (TB) band structure for h-BN has been calculated [5] by transferring the TB interactions from the analogous and better understood graphite. The results are partially reported in Fig. 1.9a and Fig. 1.9b from ref. 2. These figures are in reasonable agreement with the experimental electronic structure extracted from X-ray and photoemission measurements [5]. Contrary to the graphite without forbidden gap, h-BN exhibits a net direct gap at the Brillouin Zone (BZ) boundary along the quasimomentum line KPH (Fig. 1.9c). Moreover, the valence band region around the maximum is eventually constituted by $(p_z)_N$ orbital dominant bonding π states, while the region of the conduction band around minimum is rather constituted by $(p_z)_B$ orbital dominant anti-bonding π^* states (Fig. 1.9a). This behavior might be depicted in Fig. 1.9d with the following interpretation: the relatively lower potential (due to larger nuclear charge) of $(p_z)_N$ is the origin of the relatively larger electronegativity of nitrogen atom and therefore the bonding π orbital seems to be located rather near the nitrogen atom (it is $(p_z)_N$

dominant) and it is occupied by both electrons. On the contrary, the anti-bonding π^* orbital might be located rather near boron atom (it is $(p_z)_B$ dominant) since boron atom has relatively lower nuclear charge and then it remains non-occupied. One more remark about π and π^* bands that must be mentioned here is that they are relatively wide (especially π^* band). This may be interpreted as follows: the $(p_z)_B$ and $(p_z)_N$ orbitals of the h-BN layer structure have relatively greater spatial extension throughout the larger interlayer space (interlayer distance$= c/2 \approx 3.33\ \mathring{A}$) than the $sp^2 - \sigma$ like in plane bonds (B-N bond distance in the plane is almost the half, $1.45\ \mathring{A}$). The relative higher width of π^* band might be due to the fact that the $(p_z)_B$ atomic orbitals are less bound, more interacting and then more affected (Fig. 1.9d).

However, the above discussion is relevant to an ideal layered h-BN structure where all states are extended throughout the whole crystal. In real cases (Fig. 1.8), there are unavoidable deviations from the ideal configurations leading to localized states, existing within limited regions of the material. These localized states may be roughly divided into two classes:

a. **Tail states**
b. **Deep states**

The energy levels of these states are expected to be distributed in energy due to the possible differences in the surrounding of each state.

a. Tail states: They should derive from the relevant band states due to bond angle and bond length distortions. A distortion around a site, at the average position *R*, leads to a local trapping potential V(*R*-*r*), which, in its turn, localizes one of the band energy levels E. The total number of states remaining conserved, the width of the density of states (DOS) of a band may be broadened more or less on either side depending on the strength of the local perturbations.

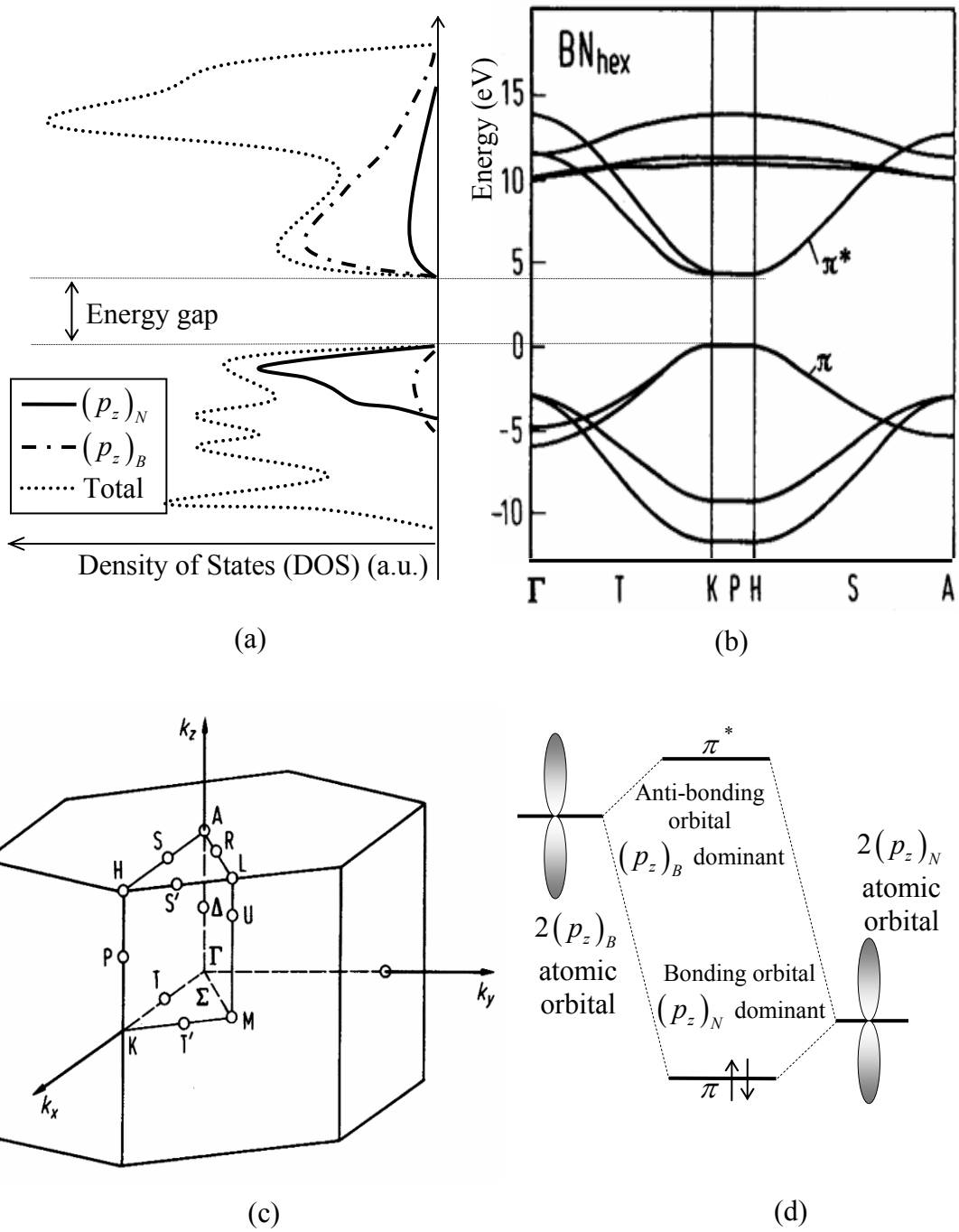

Figure 1.9: (a) Density of states around the energy gap. (b) Energy versus quasimomentum along the indicated direction in the Brillouin Zone [6]. (c) First BZ of h-BN structure energy gap occurs at the BZ boundary KPH [6]. (d) Schematic representation of atomic p_z orbital interaction for producing both valence and conduction bands.

The overall amount of V, reflecting the strength of local distortion, is related to the defect formation energy such that larger defect formation energy decreases the thermodynamical existence probability of this defect. Taking into account the independence and randomness of each local potential, the probability of occurrence of a local potential V is reasonably expected to be a "one sided" Gaussian relation:

$$P(V) = \frac{1}{\sqrt{2\pi\sigma_s^2}} \exp(-\frac{V^2}{2\sigma_s^2}) \tag{1.1}$$

where σ_s is the standard deviation from the reference value; which is the extended state band edge, (this is taken as reference level zero). In this respect, σ_s may be taken as a degree of average distortion or disorder parameter.

The effective extension of each local potential should remain within about the interatomic distance; at least the core effect distortion might be very narrow. Consequently, these local potentials might be replaced by more or less deep square well type potentials (schematically shown in Fig. 1.10).

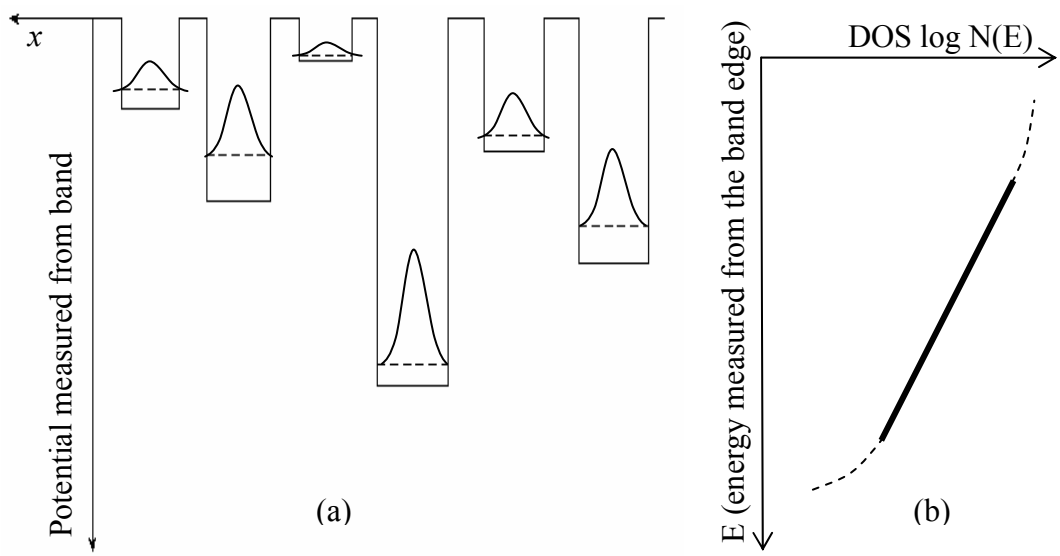

Figure 1.10: (a) Potential distribution where the fundamental wave function and resulted localized energy level are shown. (b) The distribution of density of states (DOS) from band edge into the gap as a function of energy.

Considering only the fundamental states as binding trap energies, the calculation supplies a density of states $N(E)$ (the number of energy level per unit energy interval per unit volume) which is taken simply as exponentially decreasing function of energy towards the gap (Fig. 1.11):

$$N(E) = N_{edge} exp\left(-\frac{|E|}{E_0}\right) \tag{1.2}$$

with $E_0 = \frac{\pi^2 \sigma_s^2}{2V_0}$ and $V_0 = \frac{\pi^2 \hbar^2}{8ma^2}$ (1.3)

where $2a$ is the potential well width and m is the mass of electron.

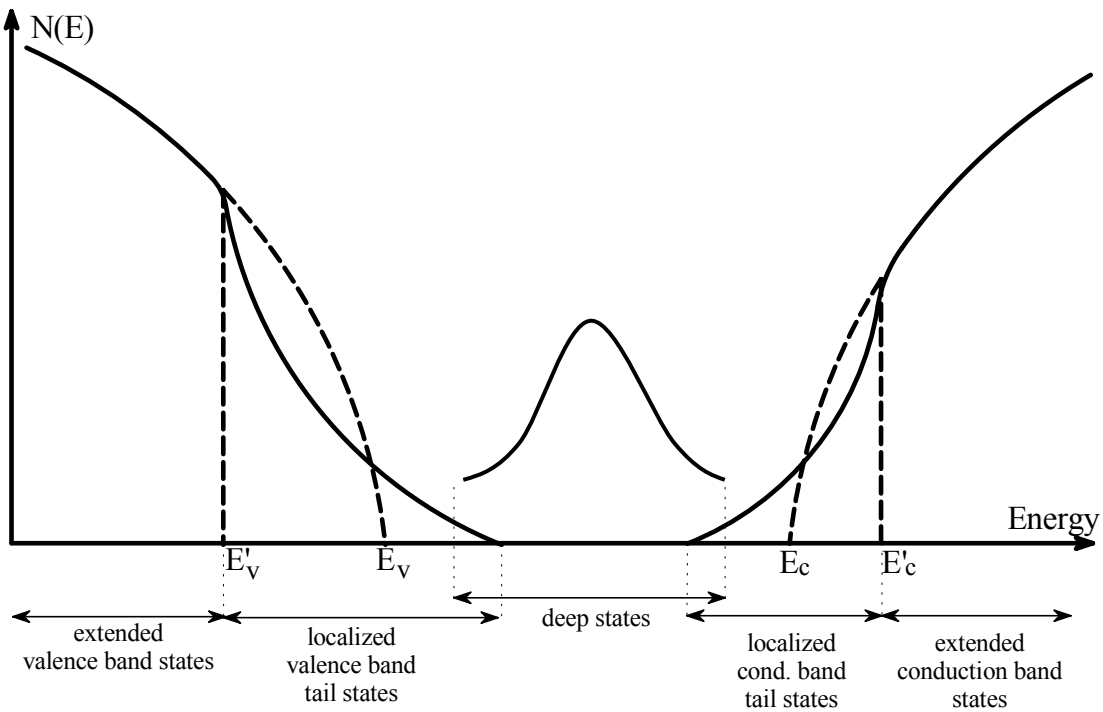

Figure 1.11: Various sorts of DOS expected in distorted semiconductor.

b. Deep states resulting from coordination defects (dangling bonds): The coordination defect states are mainly related to the broken or dangling bonds (DB). Defects of much more larger sizes together with foreign atoms would contribute to these deep states very different from constituent atoms B and N. As the surrounding

of each atomic site might be different in this randomly distributed hexagonal BN clusters (Fig. 1.8), the density of energy levels associated with these DBs, exhibits Gauss-like distribution,

$$N = N_m exp\left(-\frac{\left(E - E_m\right)^2}{2\sigma_o^2}\right) \tag{1.4}$$

around the middle of the gap. Taking into account the amphoteric nature of DBs (i.e. simultaneous presence of positive, neutral and negative charge states), the doubly occupied sites lead to a shifted Gauss-like DOS distribution due to the correlation energy. Thus, these DB distributions together with the localized DOS of weakened bonding (valence band tail) and anti-bonding states (conduction band tails) should cover the whole forbidden gap at least within defective "amorphous" layer neighboring the substrate.

1.2 Interaction of Electrons with Electromagnetic Radiation

A photon of vector potential $\vec{A}$, modifies the momentum of an electron by a term $-e\vec{A}/c$, which governed by Maxwell's Equations. An electron at the top of the valence band of a semiconductor, thus interacts with a photon to have the Hamiltonian

$$H = \frac{\left(\hat{p} - \frac{e\vec{A}}{c}\right)^2}{2m} + V\left(r\right) \tag{1.5}$$

This expression may be expressed in terms of the Hamiltonian in darkness and an additional perturbation term caused by the illumination. To obtain the Hamiltonian for illumination, we need to use the Lorenz Gauge $(\vec{\nabla} \cdot \vec{A} = 0)$ and keep only the first order term of the vector potential as the contribution of the quadratic term is negligible:

$$H = H_0 + W\,, \tag{1.6}$$

$$W = i\frac{\hbar e}{mc}\vec{A}\cdot\vec{\nabla}\,, \tag{1.7}$$

where, W is the perturbing term responsible for the transitions. To obtain the transition probability from an initial state to a final state, time-dependent perturbation theory should be considered (Appendix A). This theory gives out approximate results as it is derived from a series expansion of a time-dependent function, however, the physicist is free to take as many terms as necessary from the series according to the conditions of the problem. In the case of electromagnetic radiation, the perturbation is usually very small, such that only first few terms in the series expansion of transition probability will be enough. Up to first order approximation, the transition probability from an initial state *i* to a final state *n* is given by (Appendix A):

$$\left|c_n^{(1)}\right|^2 = \frac{1}{\hbar^2}\left|\int_0^t \langle n|W|i\rangle e^{\frac{i}{\hbar}(E_n - E_i)t} dt'\right|^2 \tag{1.8}$$

where $c_n^{(1)}(t)$ is the first order term in the series expansion of the weight function of the final state *n*. The transition is defined by the rate of change of transition probability per unit time:

$$M_{in} = \frac{d}{dt}\left|c_n^{(1)}(t)\right|^2 \tag{1.9}$$

The transition rate of an electron is strongly related to the absorption of light in semiconductors. In general, principles of conservation of energy and that of momentum lead to the absorption probability per unit time (Appendix A):

$$M_{in} = \frac{2\pi}{\hbar}\left|\upsilon_{in}\right|^2 \delta\left(E_n - E_i - \hbar\omega\right)\delta_{k_i k_n} \tag{1.10}$$

with $\upsilon_{in} = -\langle n | \frac{eA_0}{mc} e^{i\frac{\omega}{c}\hat{n}.\vec{x}} (\hat{\varepsilon}.\vec{p}) | i \rangle$ (1.11)

Absorption process is usually described by the absorption coefficient which is a measure of amount of energy absorbed per unit length by the system. It is naturally related to the absorption cross section (effective area of electrons for absorption) and density of initial and final states. The effective cross section of electrons can be defined as the transition rate per energy flux and density of states can be determined by considering that the smallest volume cell may contain two electrons with spins up and down. Then, the absorption coefficient is given as (Appendix A):

$$\alpha = \frac{e^2}{\pi^4 cm^2 n\omega} \int_{\tau_k} \left| \upsilon_{if} \right|^2 \delta\left(E_f(k_i) - E_i(k_i) - \hbar\omega \right) d\tau_{k_i} \tag{1.12}$$

where $d\tau_{k_i}$ is the volume element of momentum space. In a semiconductor, majority of the electrons are located in the valence band, slightly bound to its nucleus. If the semiconductor is illuminated with a light of enough energy, an electron can break its bond and jump to the conduction band and becomes ready to contribute to the conduction mechanism. Electronic band structure of semiconductors is divided into two groups: direct band and indirect band. This categorization is done according to whether the valence band maximum and conduction band minimum occur at the same momentum.

In direct band semiconductors, valence band maximum is below the conduction band minimum on energy axis (Fig. 1.12). A photon with at least the band gap energy can be absorbed and the electron can make a transition to the conduction band without a necessity of phonon absorption for momentum conservation. Eliminating the momentum conservation factors in Eq. 1.12, absorption coefficient for direct band gap semiconductors is (Appendix A):

$$\alpha = \frac{2e^2 \left| \upsilon_{if}(0) \right|^2 \left(2m^*_{red} \right)^{3/2}}{\pi^3 cm^2 n\hbar^2} \frac{\left(\hbar\omega - E_G \right)^{1/2}}{\hbar\omega} \tag{1.13}$$

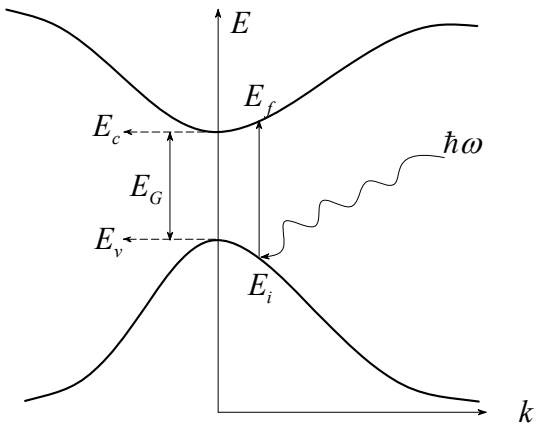

Figure 1.12: Direct band gap semiconductor in which the extrema of valence and conduction bands are in the same momentum.

The calculation of absorption coefficient for indirect band semiconductors requires momentum conservation principle. In indirect band semiconductors, the extrema of valence and conduction bands do not have the same momentum (Fig. 1.13). In this respect, a photon itself is not enough to carry an electron to the conduction band minimum; phonon absorption is required for the transition along the momentum axis.

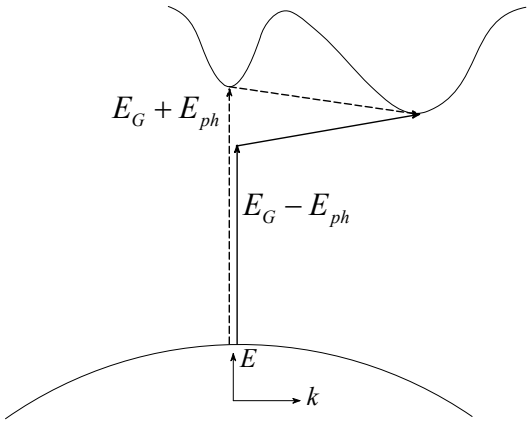

Figure 1.13: Indirect band structure and the compensation of insufficiency of photon energy by phonons.

As the electron has to catch a phonon with the required momentum, indirect transitions seems to happen slower relative to the direct ones, in which only photon absorption is enough. The required momentum of the phonon can be converted into its energy counterpart and the calculations can be followed in Appendix A, giving out the result:

$$\alpha\left(\hbar\omega\right)=\frac{A'\left(\hbar\omega-E_G\mp E_{ph}\right)^2}{\hbar\omega} \tag{1.14}$$

As for the amorphous semiconductors the uncertainty in momentum becomes very large and the momentum conservation seems to be irrelevant since a transition from any momentum to any other momentum is possible without a requirement of specific phonon absorption. Then, double integration over the initial and final momenta gives out absorption coefficient for amorphous semiconductors [7]:

$$\alpha(\hbar\omega)=B\frac{(\hbar\omega-E_G)^2}{\hbar\omega} \tag{1.15}$$

where B is a disorder parameter. Another disorder parameter for amorphous semiconductors is the Urbach energy. It was mentioned that the bond angle and length distortion, due to local imperfections of amorphous materials, results in tail states extending throughout the forbidden gap with an expression given in Eq. 1.2. This extension of density of states is exponentially decreasing with energy. Since absorption coefficient is proportional to the density of states, it is naturally expected to be an exponentially decreasing function of energy:

$$\alpha=C\exp\left(-\frac{E}{E_0}\right) \tag{1.16}$$

where E_0 is the Urbach energy which is a measure of extension of tail states throughout the band gap and C is a constant related to the properties of the material.

1.3 Mechanical Stress in Thin Films

The existence of stress in thin films was first recognized in the early nineteenth century. For instance, Gore in 1858 observed that an antimony film was prone to cracking as a result of external vibrating force or local heat application. He attributed the bending of the deposited layers to the development of "unequal states of cohesive tension" through the thickness of the deposit. The Earl of Rosse, in 1865, tried to form flat mirrors by evaporating silver on glass substrates prior to the copper deposition. He intended to do so since copper has more strength against external physical effects. However, copper on glass, without a prior silver evaporation, contracted so as to be detached from the glass substrate. Thus, a silver deposition before copper relaxed the system and reduced contraction. In addition, Stoney, in 1909, observed that the copper film electrodeposited as a protective layer on silver for searchlight applications were easily peeled off when the thickness of copper exceeded $10\mu m$.

Stoney's observation was that a metal film on a thick substrate had tension or compression in the absence of any external force, which would consequently strain the substrate so as to bend it. He made a series of experiments to relate the film stress to the amount of strain in the substrate. To do so, he deposited thin nickel films of thicknesses varying from $5.6\mu m$ to $46.2\mu m$ on steel substrates of dimension $(0.31\times102\times12)mm^3$. From the measurements of film thickness, amount of substrate bending and the elastic constants of steel, Stoney estimated tensile stresses of nickel films varying from $152\ MPa$ to $296\ MPa$ for film thicknesses from $46.2\mu m$ to $5.6\mu m$, respectively. Moreover, when the samples were heated to a "red heat so as to anneal them", their amounts of bending were considerably reduced.

Although very improved experimental tools have been produced since Stoney, the basis of determination of thin film stress is still very similar to his way. Therefore, the commonly used formula for film stresses is called Stoney's Formula in spite of

some modifications to the original form. There are several ways of obtaining Stoney's formula. A simple derivation is in what follows.

Virtually all experimental determinations of thin film stress use the variants of the equation first given by Stoney in 1909 [8]. That equation will now be derived with reference to Fig. 1.14. Let us imagine that the film is initially separated from the substrate, both of them are free of any stress and strain (Fig. 1.14a). Then, the film should be adapted to the substrate with some temporary external forces to keep the interfacial dimensions of the film identical to those of the substrate assuming film surface is larger than that of the substrate. Now, the film tends to have its initial surface area. In other words, at the instant of contact, let us assume the inwards forces are removed and then the film is forced to extend. This extension tendency can be represented by the interfacial forces, $\vec{F}_f$, on the film which can be assumed to be uniformly distributed over the cross sectional area of the film, $(d_f w)$ as shown in Fig. 1.14b. On the other hand, an opposite force, $\vec{F}_S$, should be applied from the substrate interface to limit film extension and keep it in contact. These forces which might be caused from lattice misfit, differential thermal expansion, film growth effects, etc. should be the source of stress at the film-substrate interface. The deformation will stop when these forces cancel each other. Hence, in equilibrium,

$$\vec{F}_f = \vec{F}_S \tag{1.17}$$

The moment resulting from mechanical stress is given by (Appendix B):

$$M_{ik} = \oint \left(\sigma_{il} x_k - \sigma_{kl} x_i \right) df_l \tag{1.18}$$

The total moment around the contact layer is responsible for the bowing of the film-substrate composite and equals

$$\frac{\left(d_f + d_S \right)}{2} F_f = M_f + M_S \tag{1.19}$$

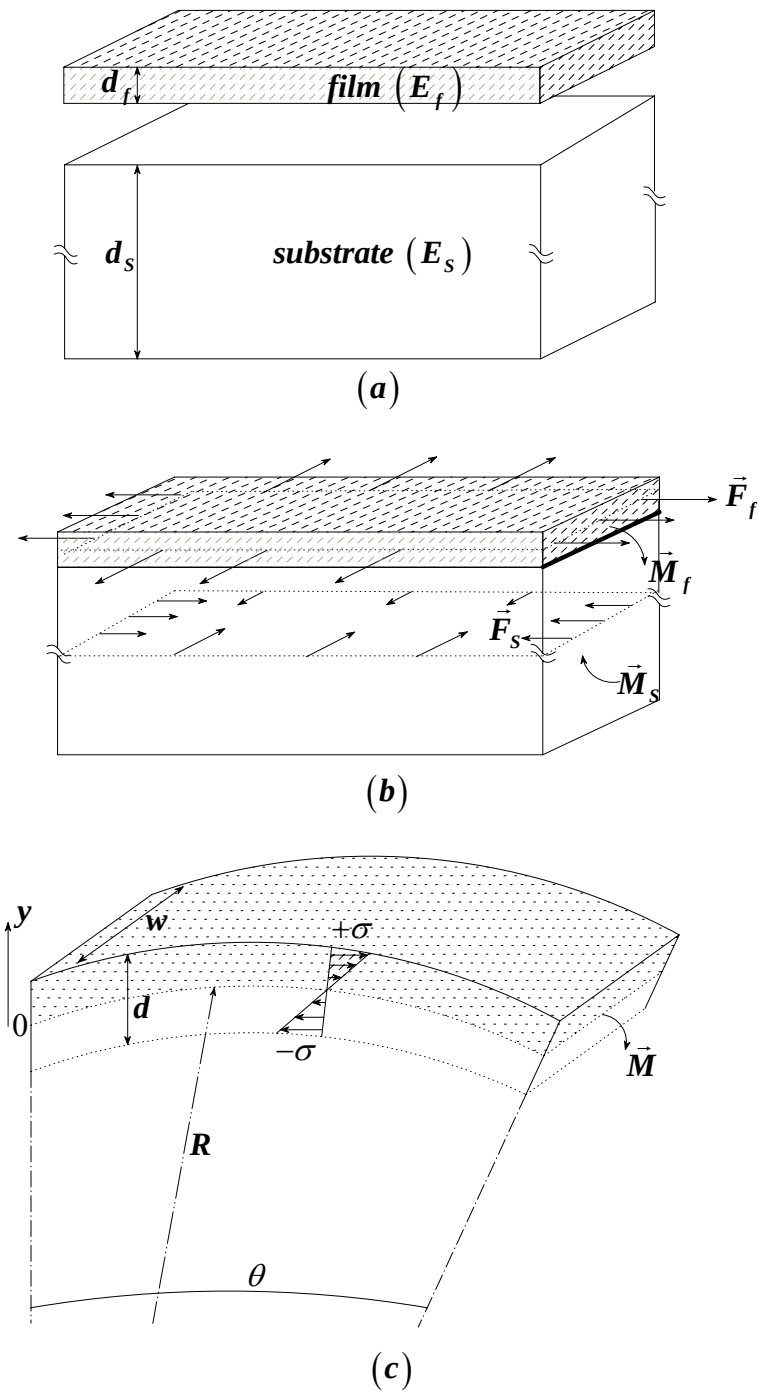

Figure 1.14: Stress analysis in a film-substrate composite. (a) Film above substrate with corresponding thicknesses and elastic constants. (b) Equibiaxial forces resulting in a moment at the interface. (c) An isolated moment $\vec{M}$ leads to a bending of the composite with curvature $1/R$.

Consider an isolated moment $\vec{M}$ shown in Figure 1.14c. In this case, the deformation is the distance between the upper end corner of the body and the mid-plane of the composite. Above this mid-layer the body is extended $(+\sigma)$ and below this layer the body is compressed $(-\sigma)$. That is why it is taken as strain-free and reference. In terms of radius of curvature, R, and angle, θ, Hooke's Law (Appendix B) yields

$$\sigma = E\left[\frac{\left(R+\frac{d}{2}\right)\theta - R\theta}{R\theta}\right] = \frac{Ed}{2R} \tag{1.20}$$

which corresponds to the bending moment M as

$$M = 2\int_0^{d/2} \sigma\left(\frac{y^2}{d/2}\right) wdy = \frac{\sigma w d^2}{6} = \frac{Ewd^3}{12R} \tag{1.21}$$

This result can now be applied to the film and substrate moments as

$$M_f = \frac{E_f w d_f^{\,3}}{12R} \text{ and } M_S = \frac{E_S w d_S^{\,3}}{12R} \tag{1.22}$$

E_f and E_S are the Young's moduli of film and substrate, respectively. Young's modulus is the proportionality constant between longitudinal strain and longitudinal stress. However, the stress leading to the longitudinal deformation here is the transverse stresses. Thus, Young's moduli need to be modified so as to give the transverse stresses for a unilateral compression (Appendix B):

$$E_f \to \frac{E_f}{1-\nu_S} \text{ and } E_S \to \frac{E_S}{1-\nu_S} \tag{1.23}$$

Hence;

$$\left(\frac{d_f + d_S}{2}\right) F_f = \frac{w}{12R}\left[\left(\frac{E_f}{1-\nu_S}\right) d_f^{\,3} + \left(\frac{E_S}{1-\nu_S}\right) d_S^{\,3}\right] \tag{1.24}$$

and considering $d_f \ll d_S$ and stress is the force per unit area, $\sigma = F_f \big/ \left(w d_f\right)$,

$$\sigma_f = \frac{1}{6R} \frac{E_S d_S^{\,2}}{\left(1-\nu_S\right) d_f} \tag{1.25}$$

This equation is called Stoney's Formula, relating the film stress, σ_f with the curvature, $1/R$.

1.4 Negative Electron Affinity (NEA)

1.4.1 Electron Affinity

Ionization energy is a commonly known concept that describes the energy required for an atom to release one electron so as to become a positively charged ion. Electron affinity can be regarded as the opposite of ionization energy. It is the energy released when a neutral atom gains an electron to become negatively charged. For instance chlorine atom gets an electron and releases 3.6 eV/atom via the following reaction:

$$Cl + e^- \rightarrow Cl^- \qquad Energy = -3.6 \text{ eV}$$

The negative sign in front of the reaction energy conventionally means energy is given by the system. Therefore, chlorine atom becomes a stable negative ion.

From semiconductors point of view, the electron affinity is the energy difference between conduction band minimum and the vacuum level (Fig. 1.15). An electron at the valence band maximum requires the band gap energy E_G to transit from bound states to the mobile (unbound) states. If the material has positive electron affinity (PEA), the energy required for that electron to reach the vacuum level is $E_G + \chi$, where χ is the electron affinity (Fig. 1.15a).

1.4.2 Negative Electron Affinity

The phenomenon of negative electron affinity (NEA) is observed when the conduction band minimum lies above the vacuum level. Any electron excited to an unbounded state in the conduction band then eligible to escape into vacuum (Fig. 1.15b). Hence for the materials having NEA, the energy required to reach the vacuum level is only E_G. This property has unique applications for electron emission devices, such as UV and X-ray photodetectors, cold-cathode emitters. Many photodetector designs already consist of NEA photocathodes. On the contrary, the photocathodes are easily contaminated which impedes the development of NEA electronic device technology.

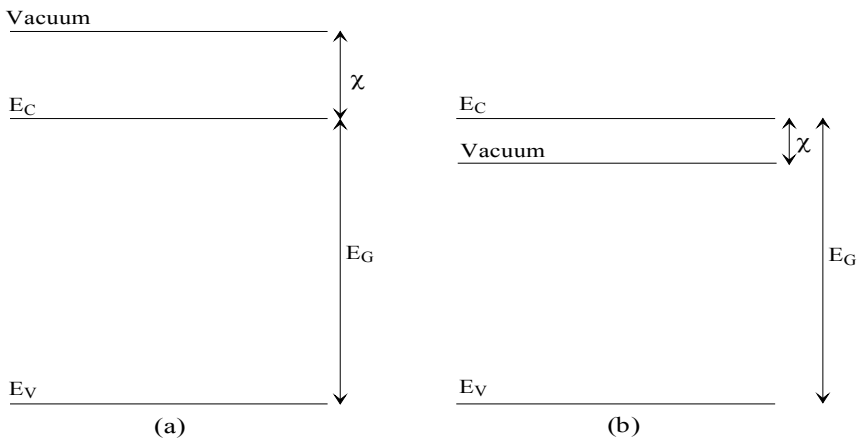

Figure 1.15: Energy band diagrams of (a) positive electron affinity, (b) negative electron affinity semiconductor. E_C, E_F, E_V are the energies at conduction band minimum, Fermi level and valence band maximum, respectively.

In intrinsic materials, vacuum level is always above the conduction band minimum, which is thermodynamically inevitable. However, there are cases where the vacuum level is pulled to lower energies. To do so, a layer of alkaline metal or its oxide should be deposited on the surface of the semiconductor film [9]. Thin solid films should satisfy some conditions to be a good candidate for NEA applications such that a negative electron affinity device (NEAD) is expected to give out sufficient performance. It should have small response times and the images should be sharp enough if a NEAD is to be used as the photocathode of photodetectors or the cold cathode of an electron emitter. Therefore, direct band gap thin film semiconductor materials and high optical absorption coefficients would result in high performance NEADs.

After the possibility of negative electron affinity was proven in 1960s, the subject attracted a great interest owing to its promising unique applications [10]. In the following years, a deceleration in the research followed because NEA surface can be easily poisoned from atmospheric contaminations. On the other hand, the proposals of new NEA materials in recent years, such as AlN and BN, have retaken the attention on the subject [11],[12]. Development of high efficiency NEADs might be possible; however, urgent understanding is required on the activation of NEA on the surfaces of semiconductors.

1.4.3 Activation of NEA

NEA phenomenon was first observed on GaAs samples coated with a thin cesium (Cs) layer [13]. The effective electron affinity could be lowered more by the additional surface treatment with oxygen to form Cs_2O layers [14]. Activation of NEA of semiconductor surfaces by Cs layers was widely accepted to obey the dipole layer (ionic) model until late 1980s [15]. This model was subjected to objections by 1989 [16], [17]; however, it consistently explains the main idea of the phenomenon.

As more than one atom come closer to form a molecule, the atomic orbitals overlap, which is a natural consequence of the electrons being attracted by the neighboring

atoms. However, no such overlaps can occur at the surface of a solid. A linear array of atoms binding to form a solid state with the surfaces at each end can be seen in Fig. 1.16. At each end of the solid the absence of atomic orbital overlaps arranges the potential distribution so as to prevent electrons from escaping to the vacuum where the potential of the nucleus is negligible. The height of this potential is called the vacuum level. The energy necessary to carry one electron from the surface of the Fermi electron sea to the vacuum level is the work function. The electrons need to reach the vacuum level for emission. Hence, emission of electrons from a relatively low vacuum level is easier.

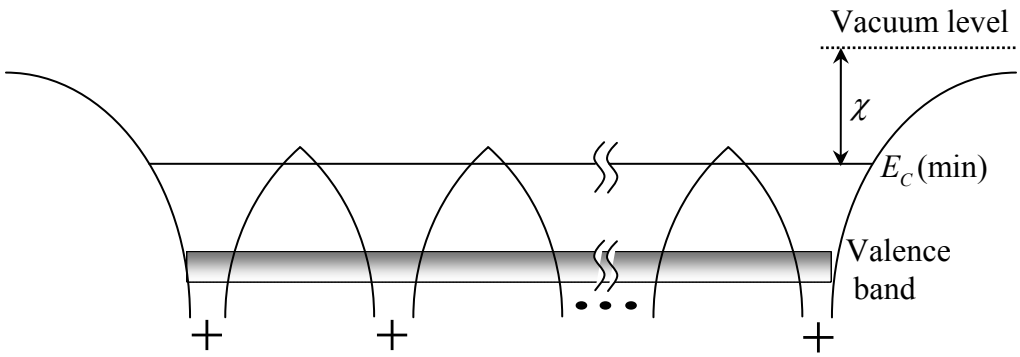

Figure 1.16: Linear array of atoms with schematic energy bands where the electron affinity is indicated.

To reach the NEA surface, the use of low vacuum level materials is essential at the first step. Vacuum level of semiconductors can be lowered by various surface treatments. Common surface treatments are done by the deposition of Cs and hydrogenated atomic layers for GaAs and diamond, respectively [18]. Lowering the vacuum level itself is not enough for the activation of NEA surfaces. The vacuum level is kept above the conduction band minimum as far as the band structure is flat (Fig. 1.17a). Pulling the vacuum level below the conduction band is possible by the creation of a depletion region of negative ions at a semiconductor/layer interface (Fig. 1.17b). Positive charges located at the surface states may be present due to dislocations, stacking faults, impurities, etc. Accumulation of positive charges at the

surface layer repels positive charges of the bulk material away from the surface. As a result, a depletion region is created consisting of only negative ions and the bands are bent downwards, pulling the vacuum level to lower values. The energy of the vacuum level might be pulled below the conduction band minimum depending on the electron affinity of the intrinsic material and the amount of band bending (Fig. 1.17b).

There are some factors contributing to the lowering of vacuum level, such as the dipole strength, thickness of the activating layer and the band gap energy of the bulk material. First, increasing the dipole density and dipole moment of the surface is one way of pulling down the vacuum level more. Dipoles are the sources of band bending at the surface of the material and thus, their density determines the bending amount. The thickness of the activating layer is another factor affecting the electron affinity. The band bending at the surface of a very thin layered surface might not be enough for the activation of NEA. Similarly, a very thick layer would act like an independent layer of a heterojunction and activating layer concept, which was discussed above, would be meaningless. On the contrary, an optimal thickness is efficient in the activation of NEA. For the same band bending behavior, an optimal thickness of activating layer results in NEA surface; however, a very thin layer makes the material remain at PEA. Finally, the effect of band gap energy width on NEA should be mentioned here. For a very low band gap semiconductor, the effective barrier height (E_B) between the bulk and the activating layer would be very high such that the escape of electrons over the barrier is greatly reduced. On the contrary, the barrier height for wide band gap semiconductors is relatively smaller such that the height of the effective potential barrier might lie below the conduction band minimum as the surface is being activated by the layer. Therefore, once an electron is excited to the conduction band, it is free to transmit above the barrier and escape into the vacuum.

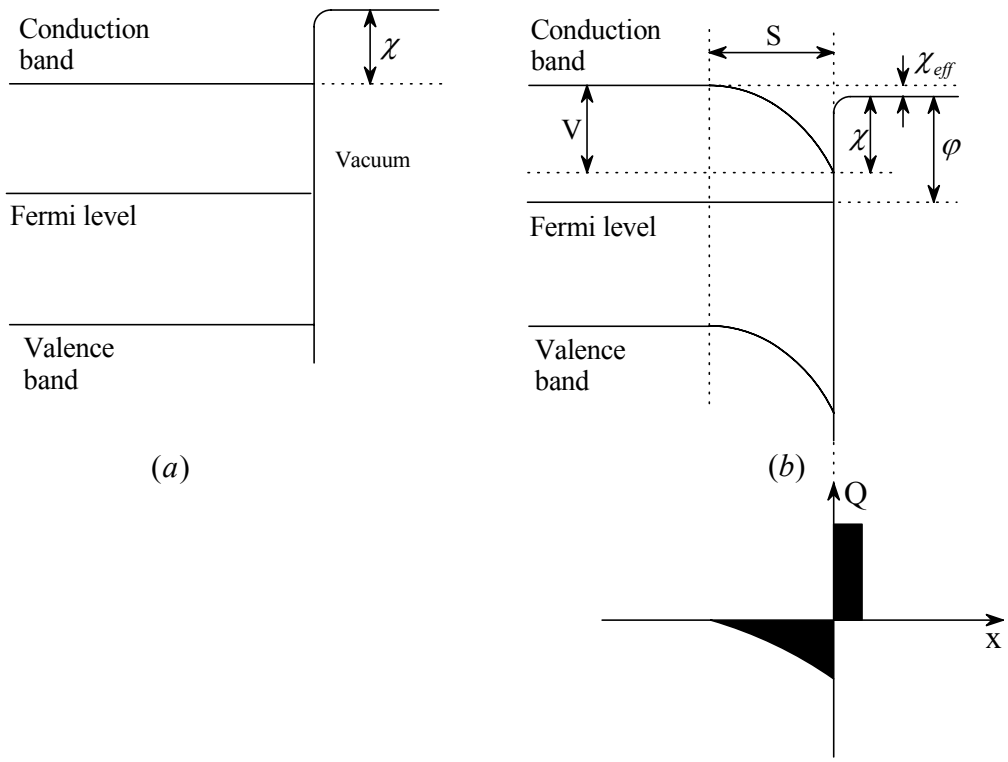

Figure 1.17: (a) In the flat band condition the vacuum level is above the conduction band minimum. (b) As the bands are bent by the creation of a depletion region due to the positively charged surface states, the vacuum level can be pulled below the conduction band minimum (above) and charges accumulated at the interface (below).

1.4.4 Negative Electron Affinity of Boron Nitride

Hexagonal boron nitride (h-BN) is a direct gap semiconductor with a wide forbidden gap of 5-6 eV. In addition, it has high absorption coefficients about $5\times10^{4}cm^{-1}$ at band gap energy. These optical properties of h-BN bring up the possibility of its usage in NEADs. Indeed, h-BN thin film was observed to exhibit NEA in 1995 [11]. A brief introduction of the NEA properties of h-BN and basic issues will be discussed below.

Diamond, which is isoelectronic to BN, is known to be NEA [18]. As a consequence of the previously discussed effect of forbidden gap on NEA, c-BN having larger

band gap than diamond may be expected to exhibit a NEA [19], whereas h-BN having more or less a similar band gap with diamond, would not. However, experiments on h-BN of various thicknesses have contradicted that judgment on h-BN; these experiments had shown that h-BN has a characteristic strong emission of a NEA [11].

It is discussed above that surface termination is the basic source of dipole creation along the interface of a semiconductor and the surface layer. In this respect, an example of surface investigation of h-BN may be done in the following manner: wide band gap and dipolar bonding configuration between B and N atoms of h-BN should be effective on the creation of a depletion region (or weak accumulation so as to result in a suitable band bending) at the interface of the bulk film and a surface layer. Although the properties of the surface layer built NEA of h-BN is still being debated, surface treatments of h-BN with hydrogen and oxygen or heat treatment of the h-BN thin films showed the following results [12], [20]: as deposited h-BN films may exhibit NEA. Heat treatment of the film at 1100 ^{0}C eliminates the NEA of h-BN surface; h-BN becomes PEA. Subsequently, exposure of PEA surface to atomic hydrogen at room temperature regenerates the NEA condition. Possible consequence of this process cycle is that hydrogen on the h-BN surface plays a fundamental role. That is, it might be at the origin of the required suitable surface dipolar layer (in this respect, the effect of H on the diamond NEA should be remembered). Moreover, the difference of electronegativities for B and N or that of their reactivities to H should contribute for that purpose [12]. Oxygen plasma treatment effect on the emission characteristics of h-BN seems rather obscure.

1.5 Possible Current Transport Mechanisms in Insulating Materials

As mentioned above, BN film has large energy gap value of about 5 eV which places it among the insulating materials. It is well known that the current transport mechanisms in insulating materials are complex. Let us give an outline on this subject in order to assess the film resistivity as correctly as possible.

The current flow (I) under a d.c. voltage (V) is either limited by metal-insulator interface or by the bulk properties of the BN films.

a. Interface limited current

In the first case, the injection or supply of charge carriers from metal electrode Fermi level (E_F) to the relevant band of the insulator will limit the current since the energy barrier $q\phi_B$ at the interface impedes the transport of carriers (emission or contact limited current). Two mechanisms may be considered to overcome this barrier: carriers can pass over the barrier by thermionic (Schottky) emission (mechanism "1" in Fig. 1.18) [21], or carriers can tunnel the barrier (Fowler-Nordheim) towards the insulator band (mechanism "2") or towards insulator trap level E_t (mechanism "3"). The thermionic current is the strongly temperature dependent mechanism (mechanism "1" in Fig. 1.18) [21]:

$$I \sim T^2 \exp\left(\frac{a\sqrt{V}}{T} - \frac{q\phi_B}{kT}\right) \tag{1.26}$$

where V is the applied d.c. voltage, T is the temperature, $a = \sqrt{q/(4\pi\varepsilon_i d)}$, ε_i is the insulator permittivity and d is the insulator thickness. The slight voltage dependence in this mechanism is due to the image force induced lowering of the barrier ϕ_B under applied electric field [21].

The Fowler Nordheim tunneling current is obtained by considering the transmission probability of the carrier through triangular shaped energy barrier. This current is strongly applied voltage (electric field) dependent (almost temperature independent) [22]:

$$I \sim V^2 \exp\left(-\frac{b}{V}\right) \tag{1.27}$$

where b is a constant.

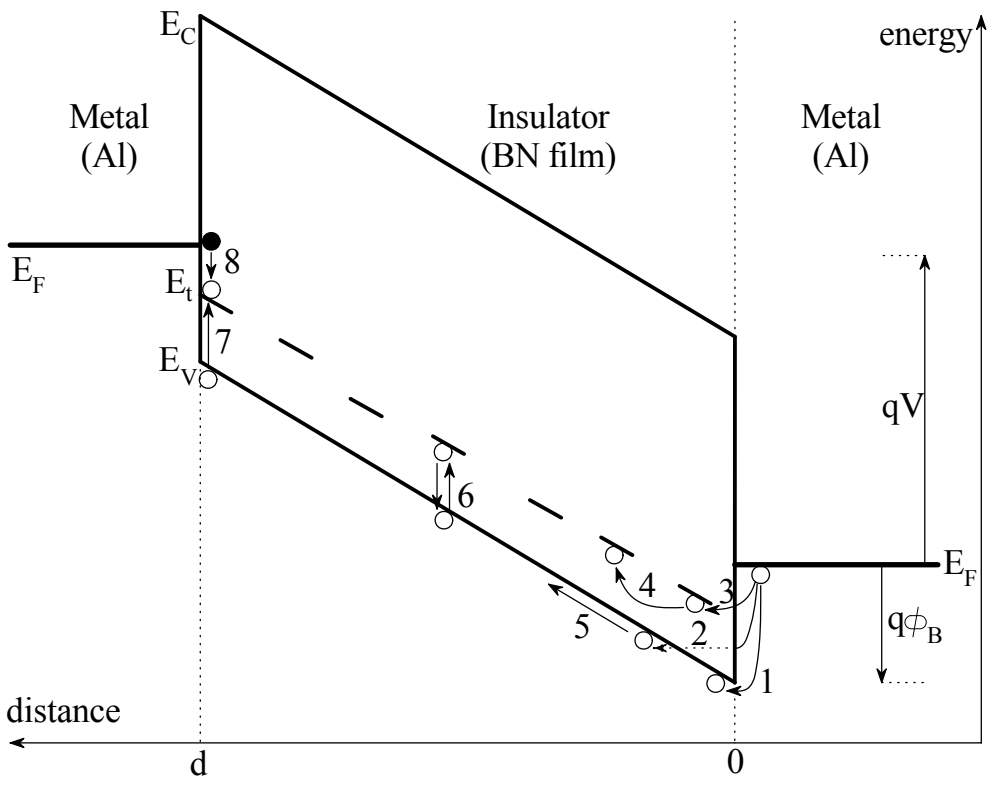

Figure 1.18: Possible charge carrier transport mechanisms across a MIM (metal-insulator-metal) structure (• electrons, o holes, E_F metal Fermi levels; E_C, E_V conduction band and valence band edges respectively of the BN film, E_t a single trap level chosen symbolically for illustrating the mechanisms). The Fermi level of aluminum (Al) (having work function of about 4 eV) is placed closer to the valence band of BN film, whose vacuum level can be roughly considered to be slightly above or below the conduction band minimum. Therefore, the charge seems to be carried mainly by holes.

The current may be limited also by the emission of trapped carriers from traps towards the relevant band (Fig. 1.19). This mechanism is similar to the above mentioned Schottky emission (Eq. 1.26) [21]:

$$I \sim V \exp\left(\frac{2a\sqrt{V}}{T} - \frac{\Delta E_t}{kT}\right) \tag{1.28}$$

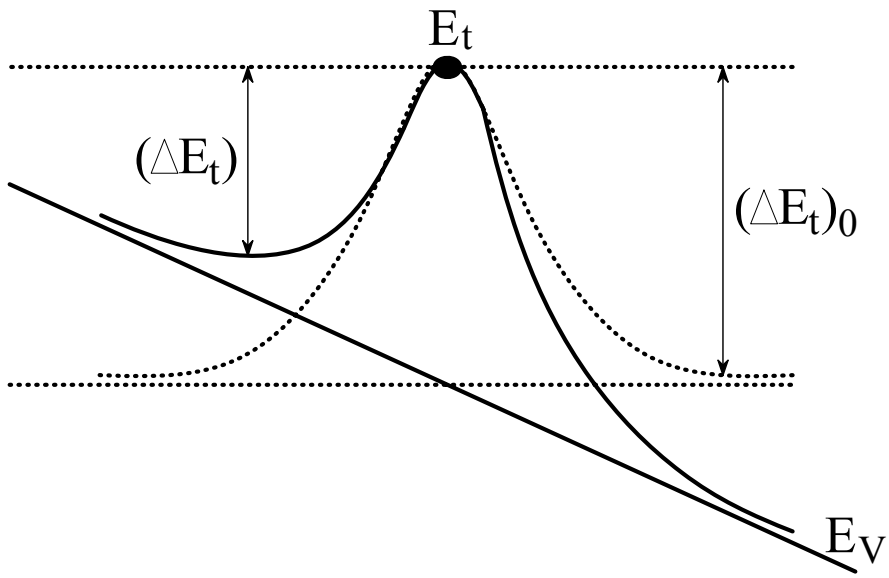

Figure 1.19: Frenkel-Poole emission of carrier from a trap where the potential around the trap is lowered from $(\Delta E_t)_0$ to ΔE_t by the applied voltage (or electric field).

b. Bulk limited current

Beyond a certain value of electric field or the temperature, the current is not limited by the contact "resistance"; but it is rather limited by space charge formed in the bulk of the insulator due to the injected carriers. Let us outline the space charge limited current.

b.1. Insulator without trap

Consider first an ideal insulator without trapping localized states (free carrier density $p_0 = 0$ and trapped carrier density $p_t = 0$). Assume that the carriers are injected from the metal electrode at $x = 0$ (Fig. 1.18). Current density (J) at the position x in the insulator may be expressed as a sum of drift and diffusion current densities:

$$J = qp\mu\xi - qD\frac{dp}{dx} \tag{1.29}$$

where p is the injected carrier concentration, μ is the carrier mobility, ξ is the electric field and D is the diffusion coefficient of free carriers. At the same x position, the Poisson's equation may be written as:

$$\frac{d\xi}{dx} = \frac{qp}{\varepsilon_i} \tag{1.30}$$

reporting Eq. 1.30 into Eq. 1.29, J becomes:

$$J = \mu\varepsilon\xi\frac{d\xi}{dx} - D\varepsilon\frac{d^2\xi}{dx^2} \tag{1.31}$$

Using the Einstein relation $D = \frac{kT}{q}\mu$, the Eq. 1.31 can be integrated:

$$J \cdot x = \mu\varepsilon\frac{\xi^2}{2} - \frac{kT}{q}\mu\varepsilon\frac{d\xi}{dx} \tag{1.32}$$

The diffusion term may be neglected when $V \gg kT/q$ since $\frac{d\xi}{dx} \approx 0$. Considering $V = \int_0^d \xi dx$, the Mott-Gurney square law may be obtained:

$$J = \frac{9}{8}\frac{\varepsilon\mu}{d^3}V^2 \tag{1.33}$$

This relation (Eq. 1.33) does not reflect the ohmicity where $J \propto V$.

b.2. Insulator with traps

As discussed towards the end of Section 1.1, there are plenty of localized states (traps) within the forbidden gap. Let us assume, first, a single trap level E_t for

simplicity. These traps, via capturing part of the free carriers from the relevant band, influence the conductivity by immobilizing a fraction of the injected carriers [22]:

$$p = p_0 + p_i = N_V \exp\left(\frac{E_V - E_{Fp}}{kT}\right) \tag{1.34}$$

$$p_t = \frac{N_t}{1 + \frac{1}{g}\exp\left(\frac{E_t - E_{Fp}}{kT}\right)} \tag{1.35}$$

where p, p_0, p_i and p_t are the free, thermal free, injected and trapped carrier concentrations, respectively. N_V is the effective density of states, E_{Fp} is the carrier quasi Fermi level, g is the degeneracy factor and N_t is the trap concentration.

Let us assume $p_t >> p$ (note that for opposite condition, the effect of traps might be negligible). Using Eq. 1.34, the expression of p_t may be written as:

$$p_t = \frac{N_t}{1 + \frac{N}{gp}} \tag{1.36}$$

where $N = N_V \exp\left(\frac{E_V - E_t}{kT}\right)$.

The equilibrium trap occupancy results from a balance between capture of carriers into the traps and their thermal re-emission into the relevant band (process 6 in Fig. 1.18)

In the presence of the applied electric field, if it is not too strong, the balance between free and trapped carriers is altered only through the change in free-carrier concentration accompanying injection. If the trap energy level E_t is a relatively shallow energy level, that is, if E_{Fp} lies above E_t (i.e. $(E_{Fp} - E_t)/kT > 1$), the Eq. 1.36 becomes:

$$p_t = g\frac{N_t}{N}p \tag{1.37}$$

Among the injected carriers, the fraction of free carriers is as follows (with $p_t >> p$):

$$\theta = \frac{p}{p+p_t} \approx \frac{p}{p_t} = \frac{N}{gN_t} = \frac{N_V}{gN}\exp\left(\frac{E_V - E_t}{kT}\right) \tag{1.38}$$

This fraction is independent of the applied voltage.

As a result, the relatively shallow traps of concentration N_t at energy level E_t will substantially affect the space charge limited injection current if $\theta << 1$ and in this case the current voltage relation becomes:

$$J = \frac{9}{8}\frac{\mu\varepsilon\theta}{d^3}V^2 \tag{1.39}$$

If there are traps distributed in energy instead of a single trap at energy E_t, the space charge limited current versus voltage relation will be changed. If this distribution is an exponential function of trap energy, the following relation can be obtained [22]:

$$J = \text{constant}\frac{V^{a+1}}{d^{2a+1}} \text{ with } a > 1 \tag{1.40}$$

c. Ohm's law regime

In an insulator of large band gap E_G, the free carrier density p_0 is expected to be very low $[p_0 \approx \exp(-E_G/2kT)]$. The free carrier density may be exceptionally large if there is a shallow dopant level of sufficient concentration. These dopants can supply free carriers to the relevant band, leading to the Ohm's law:

$$J = qp_0\mu\frac{V}{d} \tag{1.41}$$

This ohmic behavior will last until the average injected excess free carrier density p_i becomes comparable (or dominant) to the thermally generated carrier density p_0. In other words, the Ohm's law regime is valid below a certain applied voltage.

CHAPTER 2

EXPERIMENTS

2.1 Production of Boron Nitride Films

2.1.1 Substrate Cleanliness

For each production cycle, crystalline silicon (100) wafers polished on both sides, glass microscope slides and quartz plates are used as substrates which are cleaned using the following standard procedure: First, glass and quartz substrates are boiled both in trichloroethylene solution and then in H_2O_2:H_2O (1:1) mixture for 2 min each. Si substrates are boiled in the trichloroethylene solution for 3 min, followed by boiling both in H_2O:NH_4OH: H_2O_2 (6:1:1) mixture for 5 min and then in H_2O:H_2O_2:HCl (6:1:1) mixture for 10 min. After each step, all substrates are rinsed in deionized water (DW) and washed in ultrasonically agitated DW for 10 min. Additionally, Si substrates are dipped in H_2O:HF (50:1) solution for 30 s to remove the eventual SiO_x layer and rinsed in DW just before all substrates are dried with the nitrogen gun. When cleaning process is over, the substrates are immediately loaded on the grounded bottom electrode of the parallel plate capacitive type plasma reactor (Fig. 2.1). Small glass pieces $(\approx 1 \times 5 \times 75\ mm^3)$ are placed as mask on some of the substrates for thickness measurements. These shadow masks avoid the plasma deposition on the selected substrate surfaces and a groovy surface is formed; see Section 2.2.2. Next, the reactor is pumped down to below 1 mTorr and before starting the growth process in situ nitrogen cleaning is performed for 5 min.

2.1.2 Plasma Reactor

As previously mentioned, BN thin films are deposited using parallel plate plasma enhanced chemical vapor deposition (PECVD) system at 13.56 MHz (Plasma Lab µP 80) with ammonia (Chapter 3) or nitrogen (Chapter 4) and hydrogen-diluted diborane (15%) as source gases. Temperature and RF power of the ground electrode together with the pressure of the chamber are controlled by the interface unit of the deposition system. As the chamber is adjusted at a constant pressure of 0.5 Torr for NH_3 source gas (Chapter 3) or 0.1 Torr for N_2 source gas (Chapter 4), the reactant gases are sent to the chamber through a shower head which is placed at the center of the upper electrode and pumped out of the system with a rotary pump from under the bottom electrode (Fig. 2.1). Outgases are first burnt in high temperature oven and then released to open air as decomposed molecules in order to eliminate any explosive risks. During gas transition over the substrates, RF power of 250 W is applied between the electrodes and then plasma is created. As the deposition is performed, RF power is switched off, and the pressure is decreased down to high vacuum. Next, the chamber may be opened to collect the samples when the temperature of the ground electrode is decreased to about 40 ^{0}C.

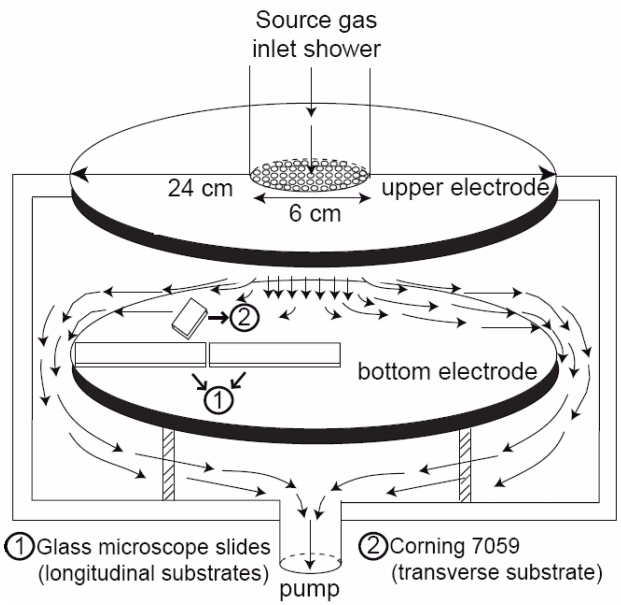

Figure 2.1: Schematic diagram of RF PECVD reactor for thin film deposition with commonly used substrate positions indicated.

2.2 Main Measuring Systems for Film Characterization

2.2.1 Mechanical Measurements

A mechanical stylus profilometer (AMBIOS XP-2) with tip radius of 2.0 microns, approximate lateral resolution of 100 nm and vertical resolution in between 1.5-62Å is used to obtain the surface profile of the samples (Fig. 2.2). Data processing within the profilometer may be briefly explained as follows: Let a sample be placed on the sample stage (the implementation of this system has been achieved within the frame of this thesis by using the documents and software supplied by the producer company [23]). The tip is engaged onto the sample with a user-defined stylus force (between 0.05 and 10 mg). Surveying on a rugged surface, as the tip moves up or down stylus force can be kept constant with the force coil creating a suitable moment on the frictionless pivot. In order to determine the tip height, a red laser light is reflected from the mirror-like back of the tip holder and aimed to the split photo detector (SPD). When the tip holder is horizontal (zero altitude) the laser light is equally shared by both sub-detectors of the SPD. Then, the signal intensities of both sub-detectors are subtracted from each other and zero altitude is verified (signals are identical and subtraction gives zero). On the other hand, when the tip holder is not horizontal (i.e. tip climbs up a valley or goes down a cavity) the laser light would be rather projected more on the lower or upper sub-detector. In this case, the subtraction of the signal intensities does not give zero and the resultant signal is amplified for a precise height determination. This process is done for every data point (maximum data points for a measurement is 60,000) and the result is loaded to the computer screen as the two dimensional surface profile of the sample.

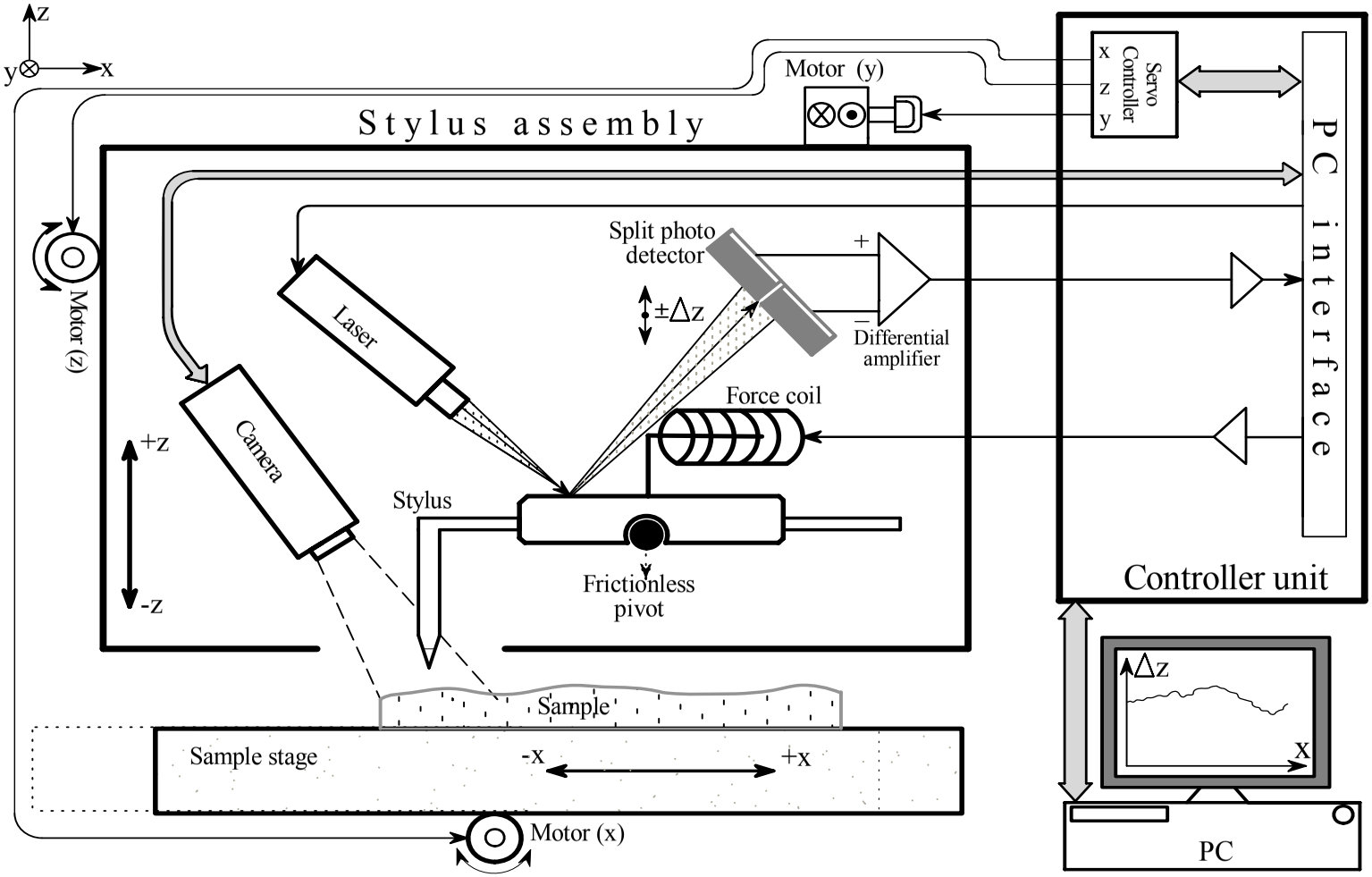

Figure 2.2: Schematic diagram, depicting the main parts and measurement principle of mechanical stylus profilometer.

2.2.2 Thickness Measurements

Prior to the deposition, small glass shadow masks are placed on the substrates resulting in the formation of a groovy surface (Fig. 2.3). The base of the grooves is the substrate surface and deposited film structure begins at the end of the grooves. Naked eye hardly ever recognizes the color difference between the groove and the film; however, the profilometer relieves the surface morphology precisely where the thickness of the film can be seen clearly (Fig. 2.3). It should be noted here that the film thickness at the vicinity of the groove edges may not be uniform since these places are possibly shadowed from gas flow during the growth in the reactor. An eventual nonuniformity (if exists) has to be taken into account for a correct thickness determination.

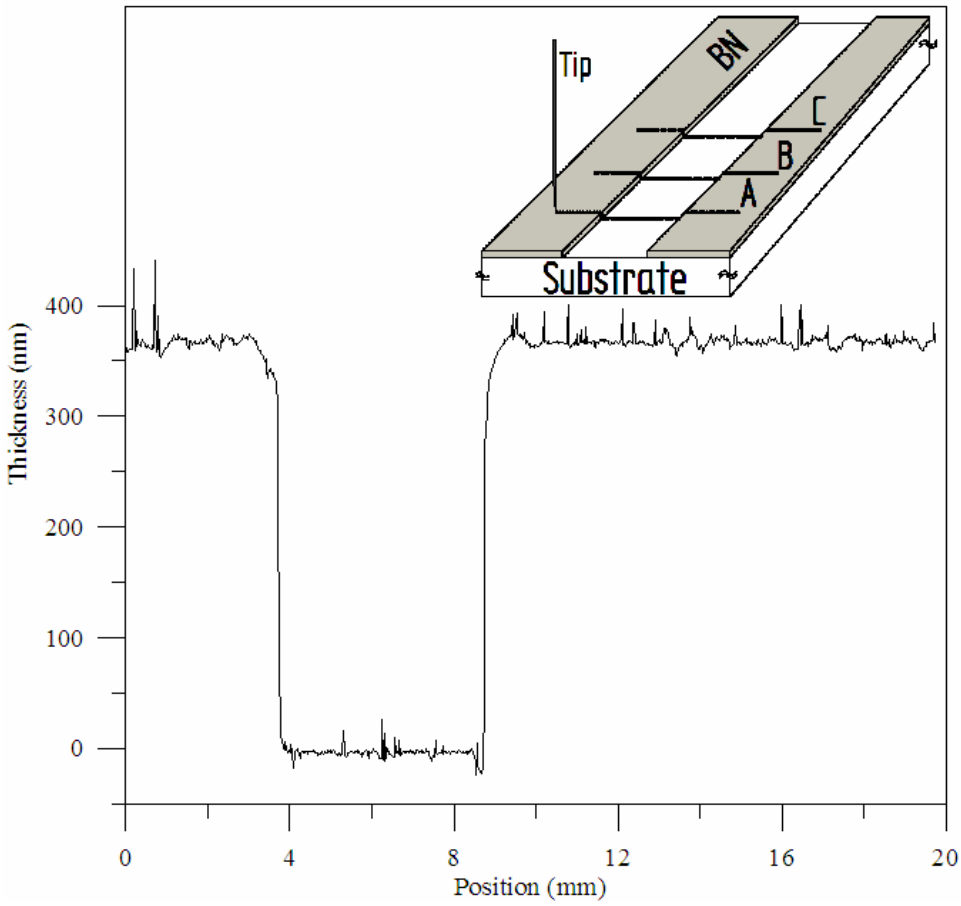

Figure 2.3: An example of profile supplying the thickness determination where the thickness is the difference between the lower and upper horizontal signal levels. Inset shows the various tip paths for determining eventual thickness distribution.

2.2.3 Thin Film Stress Measurements

Thin film stress is related to the substrate deformation by Stoney's Equation (1.25), in which the curvature of deformation should be predetermined. To determine the final shape of the substrate after film deposition, various sophisticated experimental methods can be used. For instance, the mechanical stylus profilometer would be helpful as it gives out the two dimensional profile of the film surface. Then, the data may be fitted to a least square curve as shown in Fig. 2.4. The equation of the curve is

$$y = \sqrt{R^2 - (b - x)^2} - c\,, \tag{2.1}$$

which can be fitted to the original data by curve fitting tool of MATLAB© finding the most suitable values for the parameters R, b and c.

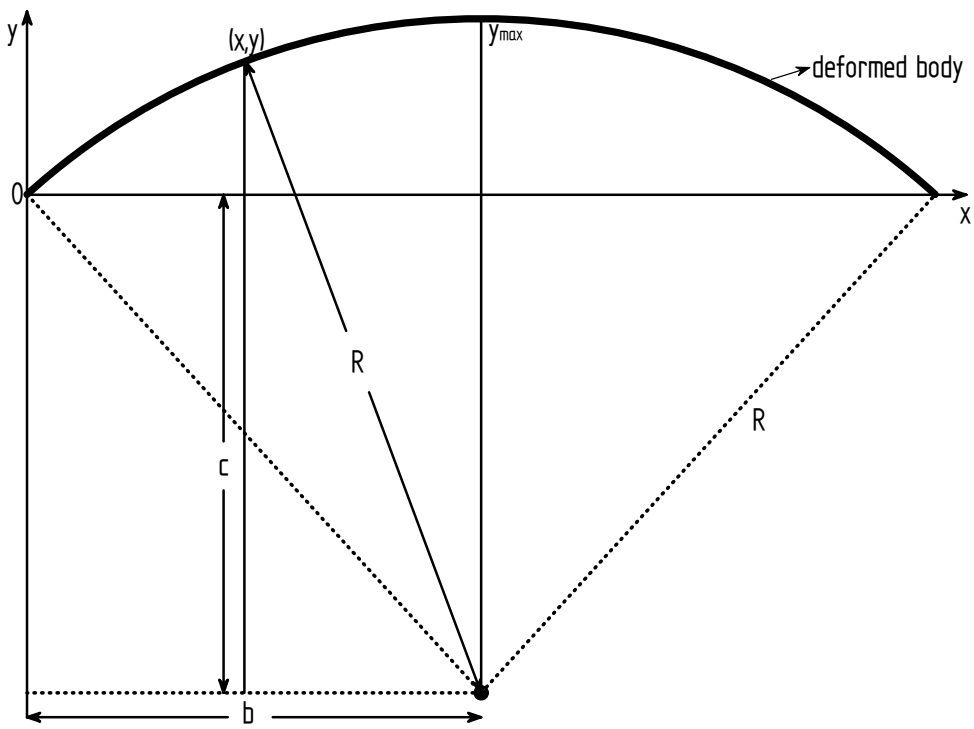

Figure 2.4: Strained film-substrate composite due to the compressive film stress leading to a curved shape of curvature $1/R$.

An example for measurement of surface profile of h-BN film on Si (100) substrate and its stress analysis are illustrated in Fig. 2.5. In this figure, least square fit of a circular arc to the absolute profile yields R, b and c values of $5.585\ m$, $1.22\ cm$ and $5.543\ m$, respectively. Using this radius of curvature and elastic constant of Si (100) as $180.5\ GPa$, the film stress can now be calculated.

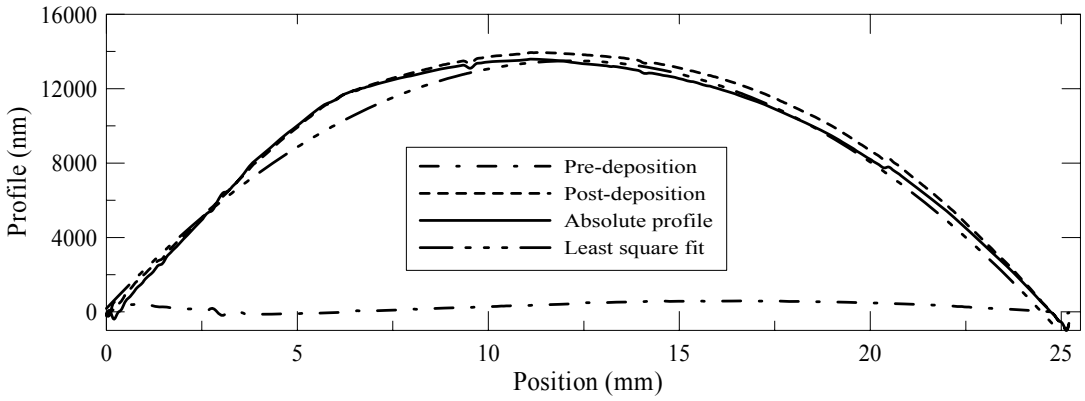

Figure 2.5: Stress analysis of h-BN film on Si (100) substrate whose thicknesses are 370 *nm* and 200 μm, respectively. Absolute profile is obtained by subtracting pre-deposition data from post-deposition one.

The result of the stress calculation from Stoney's formula application to the least square fit revealed a stress value of 585.4 *MPa*. On the other hand, a comparison of this finding has been done with the software result of the thickness profilometer for thin film stress. The software gave out a stress value of 596.7 *MPa* corresponding to a radius of bending of 5.45 *m*. The difference between the two results is almost negligible. That is, the experimenter is free to choose any one of the two methods according to surrounding of the conditions.

2.2.4 Optical Measurements: UV-VIS, XPS, IR Spectroscopies

UV-visible transmission spectra of the samples are measured to obtain the band gap energy, Urbach energy, refractive index and thickness of the samples (by Perkin

Elmer Lambda 2S Spectrometer). Measurements were taken in the wavelength region of 200-1100 nm. The transparent region of the transmission data could be well fitted by the minimization program, OPTICHAR©. Refractive indices and thicknesses were found from this region. These values were used to obtain the absorption coefficients as a function of energy by Swanepoel's method [24].

Chemical compositions of the films were determined by the XPS analyzer Specs EA 200, using an anode of Al Kα (1486.3 eV) as X-ray source (Mg Kα (1253.6 eV) is also available). The films deposited on glass substrates were used for this purpose. The surfaces of the films were cleaned from carbon contamination by sputtering with argon ions of energy 5000 eV for about 20 minutes till the carbon peak is vanished. The photoemission process leads to positively charged ion formation at the surface. Those ions attract the ejected electrons back to the surface and thus reduce their kinetic energies. This attraction leads to the shift of the binding energies to higher energies in the XPS spectrum. The calibration of peaks is done according to B 1s peak, which is located at 190.5 eV [25]. Calibration with respect to O 1s peak at 532.0 eV is also possible [26]. Atomic sensitivity factors (ASF) of boron, oxygen, and nitrogen are taken as $\sigma_B = 0.13$, $\sigma_O = 0.66$, and $\sigma_N = 0.42$, respectively. For the deconvolution of the peaks, the computer program PeakFit © is used.

Bonding structure analysis was based on Fourier transform infrared (FTIR) spectroscopy. Subsequent to the deposition (within first 30 min.), infrared absorption spectra of the films under normal incidence were measured by Nicolet 520 spectrometer (4 cm^{-1} resolution) purged with dry air. The background was corrected by measurements of substrate transmittance ($50\,\Omega \cdot cm$ Si) just before taking the spectra of the samples. In order to investigate the evolution of the films within the humid atmosphere, measurements were repeated 80 days after the deposition.

The transmission data was transferred to absorption using the formula (disregarding reflectance):

$$T = exp(-\alpha d) \tag{2.2}$$

where α is absorption coefficient and d is the thickness of the film. Background correction, deconvolution of the peaks and fitting were done using the computer program PeakFit ©.

2.2.5 Electrical Measurements

Both the vertical and lateral resistivities of the films are measured for testing the degree of insulating behavior and for carrying out eventual resistivity anisotropy (Fig. 2.6). Current-voltage characteristics of the films were measured by Keithley 6517 electrometer for high resistive systems. The device is controlled by computer via the software LabView ©. The films for electrical measurements were deposited on glass and crystalline silicon substrates. Then, aluminum planar and dot contacts were evaporated onto the films in a vacuum system. The dimensions of the contacts and distances between them were determined by the mechanical profilometer.

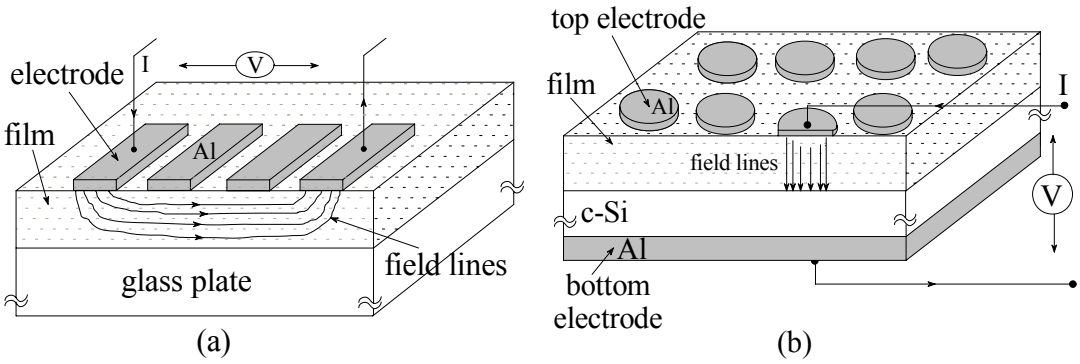

Figure 2.6: Electrical resistivity measurements through (a) lateral and (b) vertical contacts.

CHAPTER 3

RESULTS AND DISCUSSIONS ON BN FILMS USING AMMONIA

3.1 Introduction

As outlined in Chapter 1, boron nitride consists of a III-A element boron and a V-A element nitrogen which are both nearest neighbors to carbon in the periodic table. Thus, BN has the same electronic configuration as carbon molecules. Consequently, the physical structures of BN and carbon are very similar. BN, like carbon, is formed in two main phases. Hexagonal BN (h-BN) is similar to graphite as both are very soft and have a layered structure; however, unlike graphite, it has a very high electrical resistivity (along both a and c axes) and it is transparent to visible light. Other phase is cubic BN (c-BN) which is similar in bonding structure to diamond. In fact, c-BN is second, after diamond, in the list of hard materials [27]. However, h-BN is relatively easier to deposit in thin film form by PECVD system, which is an essential system for the production of large area low cost electronic materials.

A sub-phase of h-BN is the so-called turbostratic boron nitride (t-BN). This structure constitutes clusters of parallel hexagonal planes which are rotated randomly around the c-axis (Fig. 1.8). Indeed, t-BN is fairly defective as the tissue between the clusters is considered to be highly disordered. This tissue may contain (together with amorphous boron nitride (a-BN)) hydrogen and oxygen atoms which should naturally affect the film characteristics [28], [29]. Except for the turbostratic phase being a disordered structure, h-BN and t-BN exhibits the same B-N bond frequencies in infrared.

Although it has not gained a commercial importance yet, h-BN is a potential material for thin film optoelectronic applications. Having optical gap in the range 5.0-6.0 eV, it may be used as a UV-source or UV-detector [30]. Negative electron affinity of h-BN also promises unique applications like photo detectors and cold cathode emitters [31]. High breakdown field $\{(3-7)\times 10^6\ \mathrm{V/cm}\}$ and high resistivity bring up the idea of using h-BN as an insulating layer of thin film transistors [32], [33], [34], [35]. On the other hand, despite its low cost and easy production, h-BN thin films containing turbostratic form in majority comes up with defects and stoichiometry problems. High density of states (both tail and deep states) can damp its dielectric properties [26]. In addition, relative compositions of boron and nitrogen are reported to affect the film properties enormously so that boron rich films results in a very low band gap of 3.7 eV [32]. Optimization of deposition parameters should help in both increasing the structural order and reaching stoichiometry.

Ammonia and nitrogen are commonly used as source gases for nitrogen containing thin film depositions. In this Chapter, ammonia is used as the nitrogen source for BN deposition. It has several advantages, but the essential one is that ammonia dissociates easily and leads to rich chemical reactions within the plasma. It also carries the hydrogen into the plasma, which may affect the growth and hydrogenation of the films. As hydrogen is expected to play a major role in the film structure, the investigation of its effects on physical properties of h-BN films is the main goal of this Chapter.

3.2 Experiments

The c-Si wafers $(5\times 20\ mm^2)$, glass microscope slides and transparent quartz plates are cleaned by a standard process as described in Chapter 2. IR, UV-visible, thickness and mechanical stress measurements are conducted within the first half of an hour after the deposition. After the characterization of the as-deposited films is completed, four identical pieces $(5\times 5\ mm^2)$ are obtained by cutting the film/c-Si composite $(5\times 20\ mm^2)$. One is kept for reference at room temperature (RT) and the

other three are annealed in a furnace for 1.5 hours under nitrogen atmosphere at 475, 650 and 800 ºC, respectively. Three film/quartz composites are also annealed at 400, 600 and 800 ºC, respectively. The optical constants of the films are obtained from UV-visible spectroscopy measured on annealed film/quartz composites. The IR and mechanical stress measurements are taken from annealed film/c-Si composites.

3.2.1 Mechanical Stress Measurements

Stress in the films is determined by measuring the substrate curvature and the calculation via thin film stress software of the profilometer as described in Chapter 2. Manual calculation by the external MATLAB© fit program is not necessary since the obtained curve is smooth enough; whereas, some disturbing parts are taken out from the original data. The photographs of the sample surfaces are taken by a stereo optic microscope using 400X zoom. The relation between stress and microphotos of the corresponding sample surfaces is shown in Fig. 3.1. The scales of x and y axes in different graphs (in Fig. 3.1) are kept same for easy mutual comparison between the measurements. The stress of as-deposited film is tensile ~ 100 MPa. As the samples are annealed at 475 °C, stress is converted from tensile to compressive with a value 585 MPa, and further increased to 1910 MPa when annealed at 650 °C. Stress of 800 °C annealed film could not be measured; however, it may be concluded that the film possesses high compressive stress which was released by the cracking observed in the microphoto. The drastic increase in compressive stress indicates a change of atomic bond configuration at the interface. The relaxation of these bonds seems to be reduced with annealing. When the relaxation of these bonds becomes deficient (at 800 ^{0}C) the system should relax itself by cracking.

3.2.2 UV-visible Measurements

Optical transmittance spectra are taken in the UV and visible region (Fig. 3.2). The Urbach energies and optical gaps are calculated from the medium and strong absorption regions of the spectra as shown in Fig. 3.3. Optical gap of the films seems

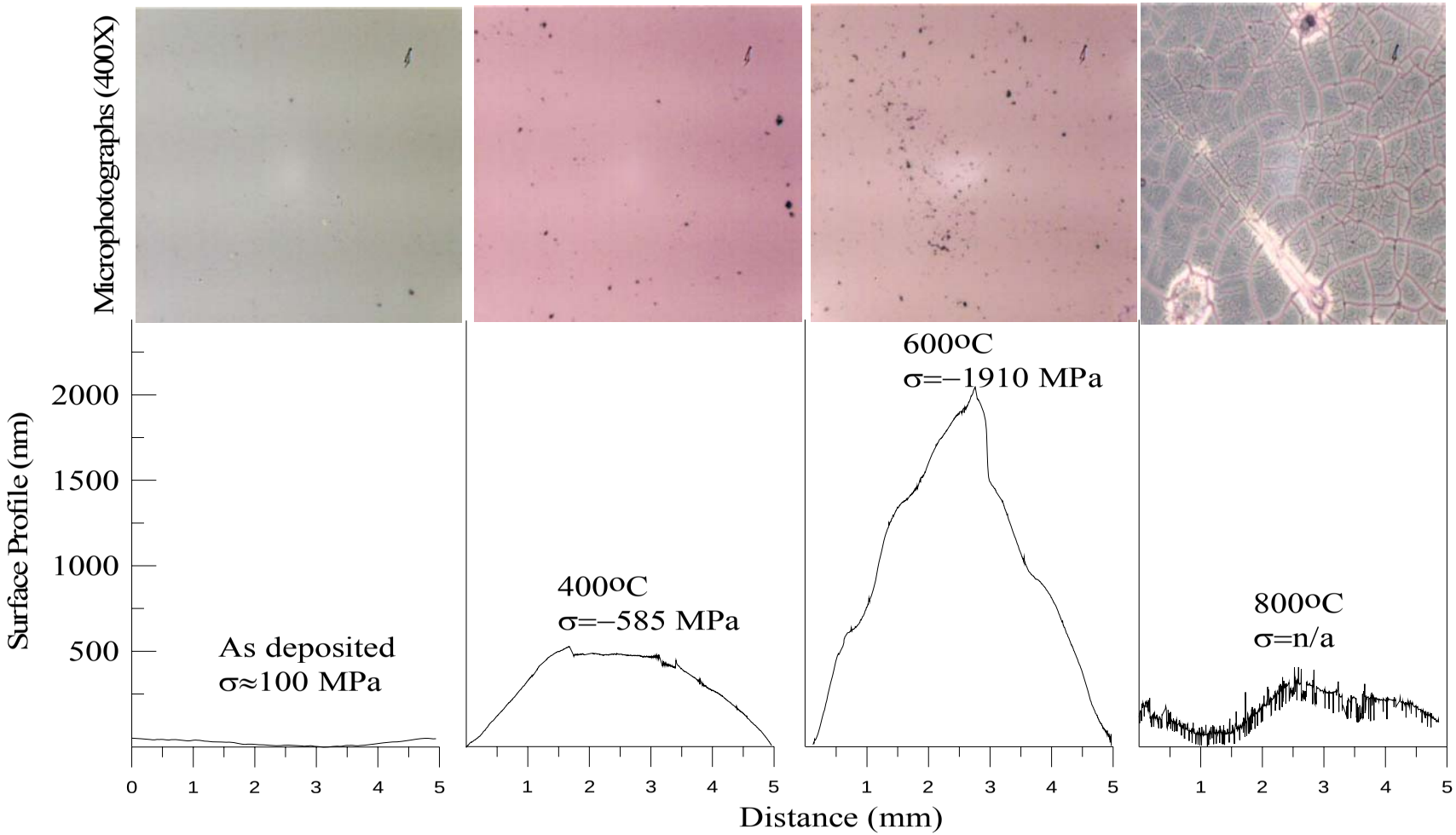

Figure 3.1: Surface profiles of the as-deposited and annealed films with the corresponding microphotos for the mutual comparison of film stresses.

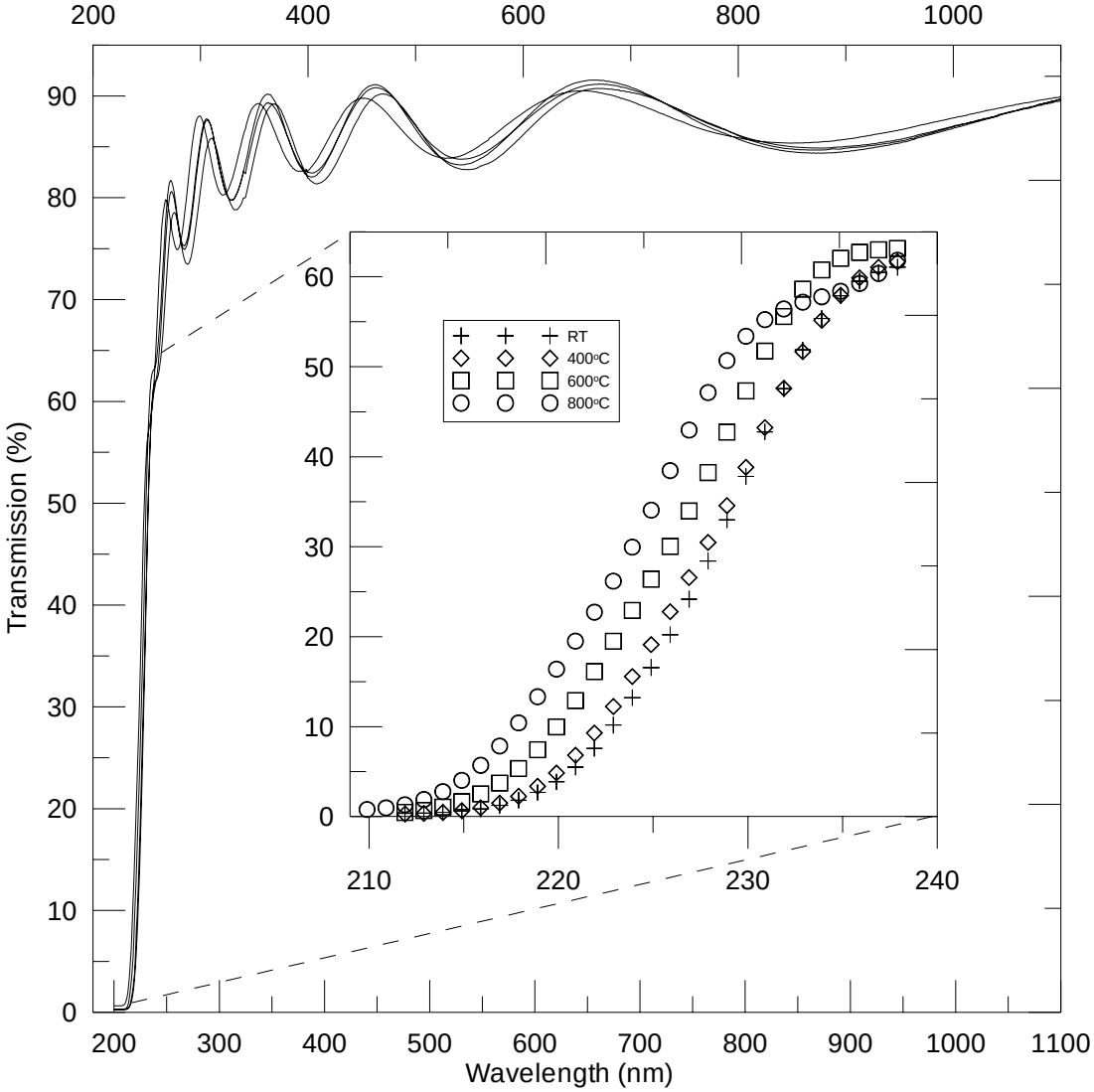

Figure 3.2: UV- visible transmission spectra of the film/quartz composites annealed at different temperatures. Inset shows the medium and strong absorption regions.

to increase slightly by heat treatments. As the error in the gap determination is considered to be around 10% arising mainly from the error of thickness measurements, the increase might be speculated within this limit. The measured gaps are about 5.3 eV which is close to the gap values of h-BN reported in literature [36]. Additionally, Urbach energy, which is a disorder parameter for an amorphous material, is obtained by linear fit of logarithm of absorption coefficient versus energy in the medium absorption region. In this region, tail-to-band transitions are taken into

account. The observation of Urbach energy for as-deposited and annealed samples exhibits a slight increase with increasing annealing temperature, which implies a rise in bond distortions. The descending relaxation of coordination defects will be attributed to the decrease in hydrogen content with annealing (discussed in the following section) and then, internal stress increases as expected.

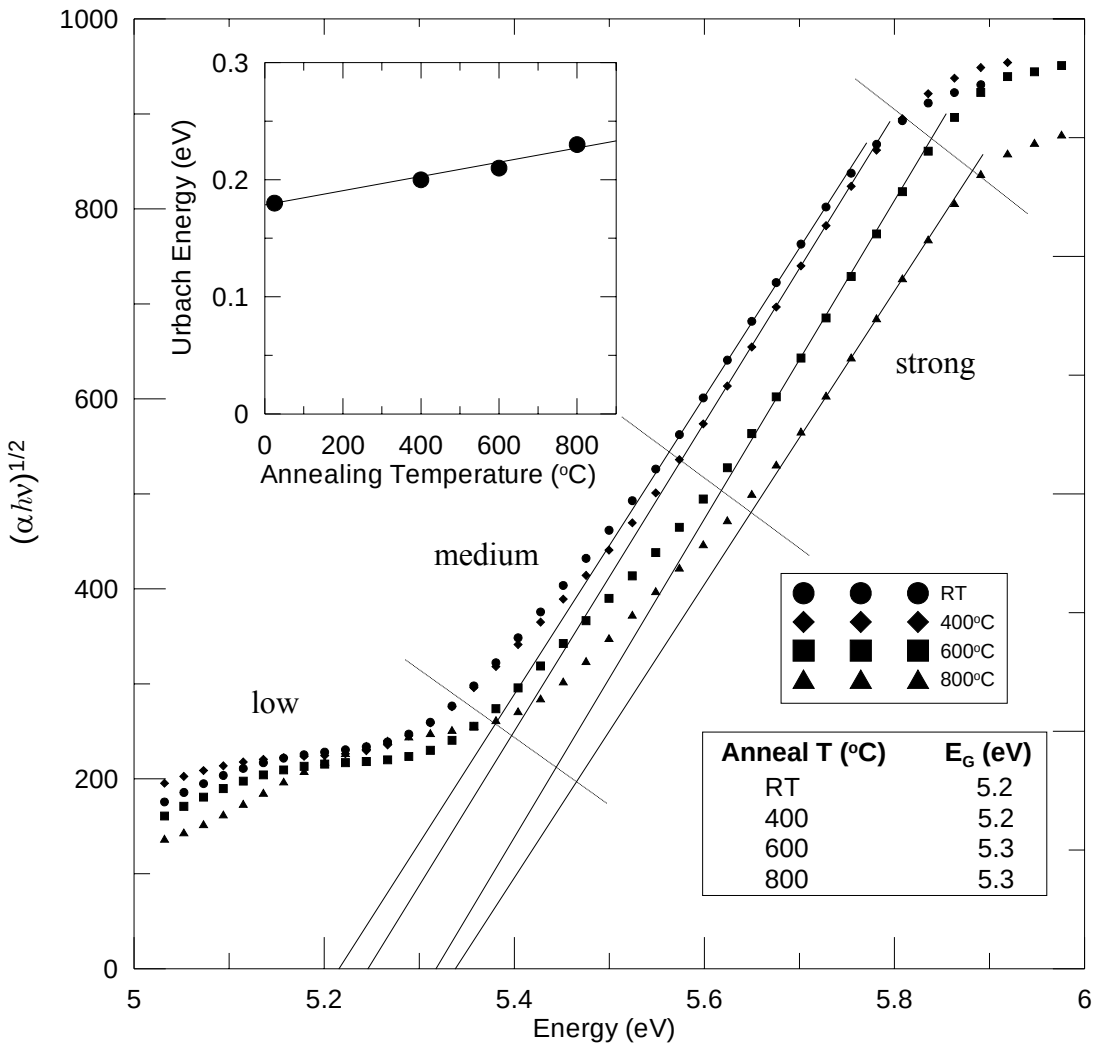

Figure 3.3: Optical gap determination from energy-axis intercept of the fit of the linear region (strong absorption). Medium absorption starts at lower energies where linear fit is separated from the data points.

3.3 Discussions

3.3.1 FTIR Measurements

In this work, bonding structure analysis of BN films was based on Fourier transform infrared (FTIR) spectroscopy technique, which allows determining phase structure (hexagonal or cubic) very fast and non-destructively. For infrared light absorption process to occur the atoms in the solid must possess time-varying dipole moment; quasimomentum and energy conservation laws should be valid simultaneously. The values of resonance frequencies are determined by transverse optical (TO) and longitudinal optical (LO) vibrational modes branches within the center of the first Brillouin zone (wavevector ≈ 0). In amorphous material quasimomentum selection rule is relaxed and phonons of any wavevector value can contribute to the absorption, resulting in broadened and low energy shifted peaks. For near-normal incidence, infrared spectroscopy gives a peak near the frequency of the TO phonon mode, since LO phonons could not absorb light because their dipole moment vector is perpendicular to the incident electric field vector.

For h-BN, the two IR-active phonons have TO frequencies at about 783 cm^{-1} and 1367 cm^{-1}, while LO frequencies are at 828 cm^{-1} and 1610 cm^{-1}. These correspond to a bending of the B-N-B bond between the basal planes and stretching of the B-N bond within the basal plane, respectively (Fig. 3.4). Very similar frequencies are observed for t-BN as well, only with broadened peaks. c-BN has a phonon with TO component at 1065 cm^{-1} and a LO component at 1340 cm^{-1} [37]. Since frequencies of c-BN and h-BN are different, FTIR is suitable to distinguish between sp^2- and sp^3-bonded phases. Although w-BN is not very well investigated, phonon frequencies at 1085, 1125 and 1250 cm^{-1} have been reported [38]. Usually, to distinguish w-BN from c-BN the peak at approximately 1130 cm^{-1} is used [39].

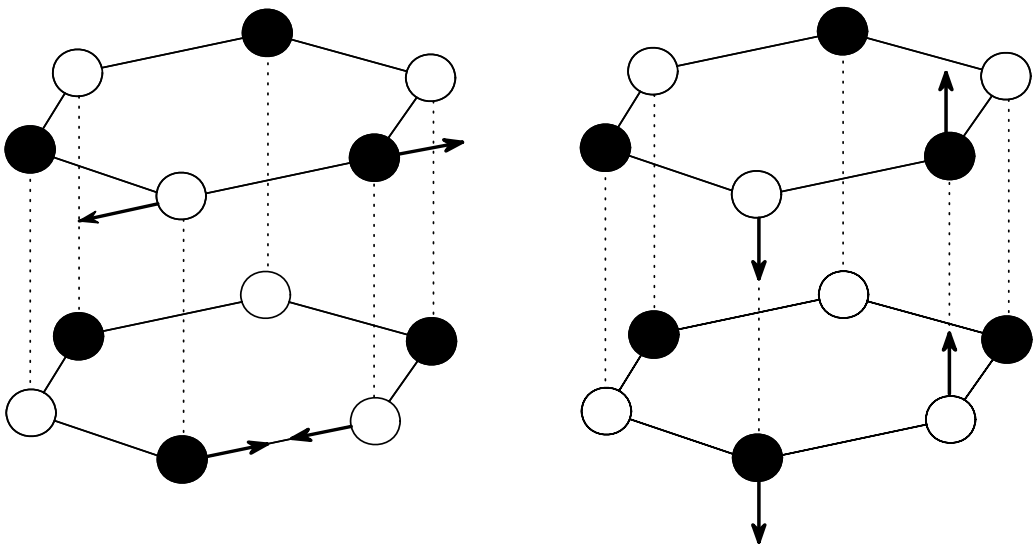

B-N in-plane bond stretching

B-N-B out-of-plane bond bending

Figure 3.4: Displacements of boron and nitrogen atoms for two infrared active vibrational modes in h-BN.

BN film FTIR spectra were fitted taking into account the fact that the surface of Si substrate with film on it is cleaner than the surface of original Si wafer substrate alone (used for background subtraction). That is, in the spectra of background Si wafer, peaks at the 550-1200 cm^{-1} region, especially around 607 and 1107 cm^{-1} associated with Si-C and Si-O bonds respectively, might have larger intensity than the intensities in the actual Si substrate. Thus, overestimation of the background may lead to artificial decrease of the absorption intensity of BN film spectrum around these peak positions. The fitting for this region is clarified in the Fig. 3.5.

FTIR spectra for as-deposited, 475 ^{o}C and 650 ^{o}C annealed BN films were fitted in similar way. Asymmetric peak around 1380 cm^{-1} was deconvoluted into three peaks with Lorentzian peaks around 1380, 1540 cm^{-1} and Gaussian peak at 1430 cm^{-1}; for 650 ^{o}C spectrum a Gaussian peak at 1250 cm^{-1} was added. Peak around 3434 cm^{-1} was fitted with Lorentzian, while Gaussian peak fitting was used (Fig. 3.6) for remaining peaks in the spectra. For the film annealed at 800 ^{o}C Gaussian peaks are

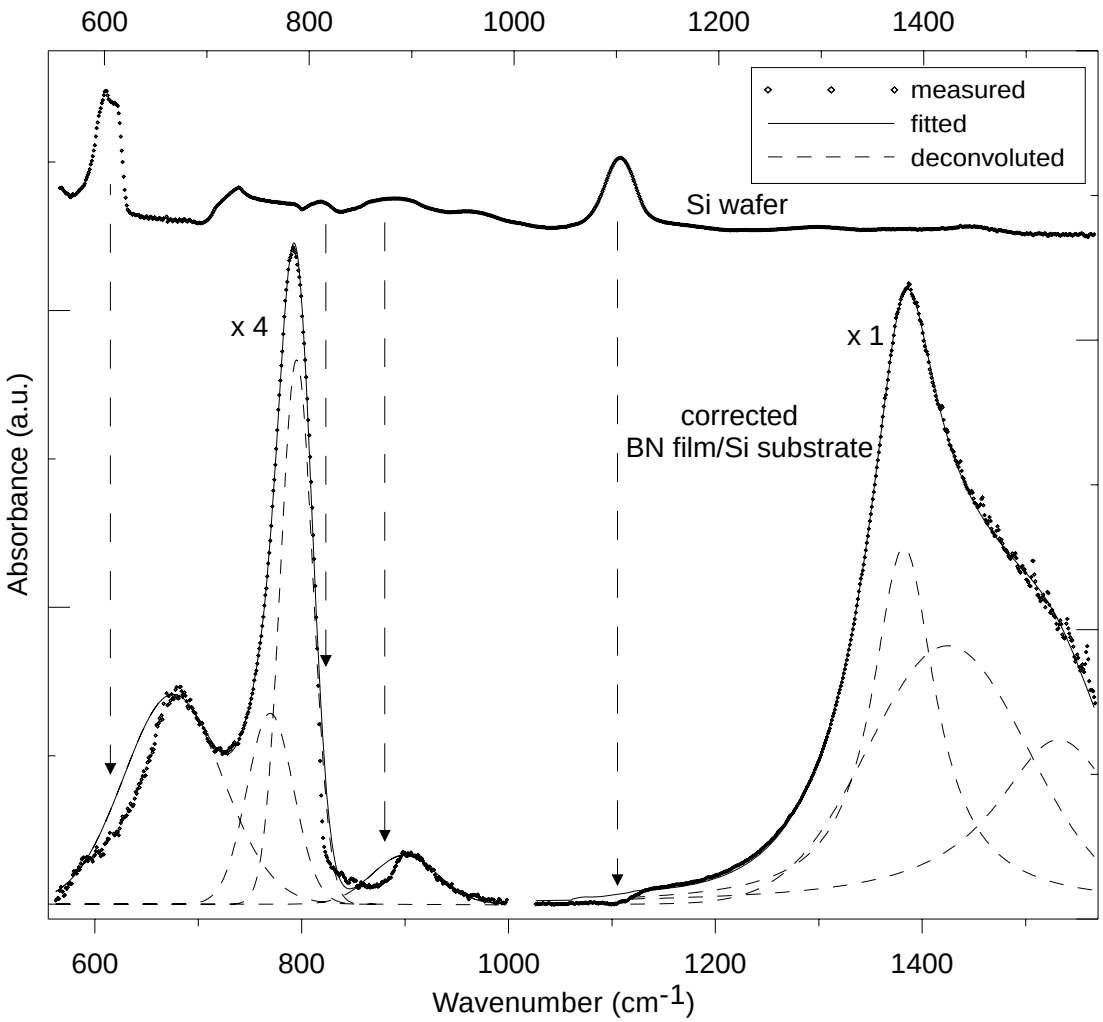

Figure 3.5: Removal of the Si substrate contribution in the spectra of BN/Si substrate sample (overcorrection is not impossible).

used except peaks at 1380 and 1598 cm^{-1}, for which Lorentzian distribution is used. The deconvoluted peak positions and their FWHM are given in Table 3.1 together with possible peak assignments found by scanning the relevant literature.

Broad peak around 1380 cm^{-1} and the one near 790 cm^{-1} are the characteristic peaks of sp^2 bonded t-BN films. For both of these peaks the LO and TO components are

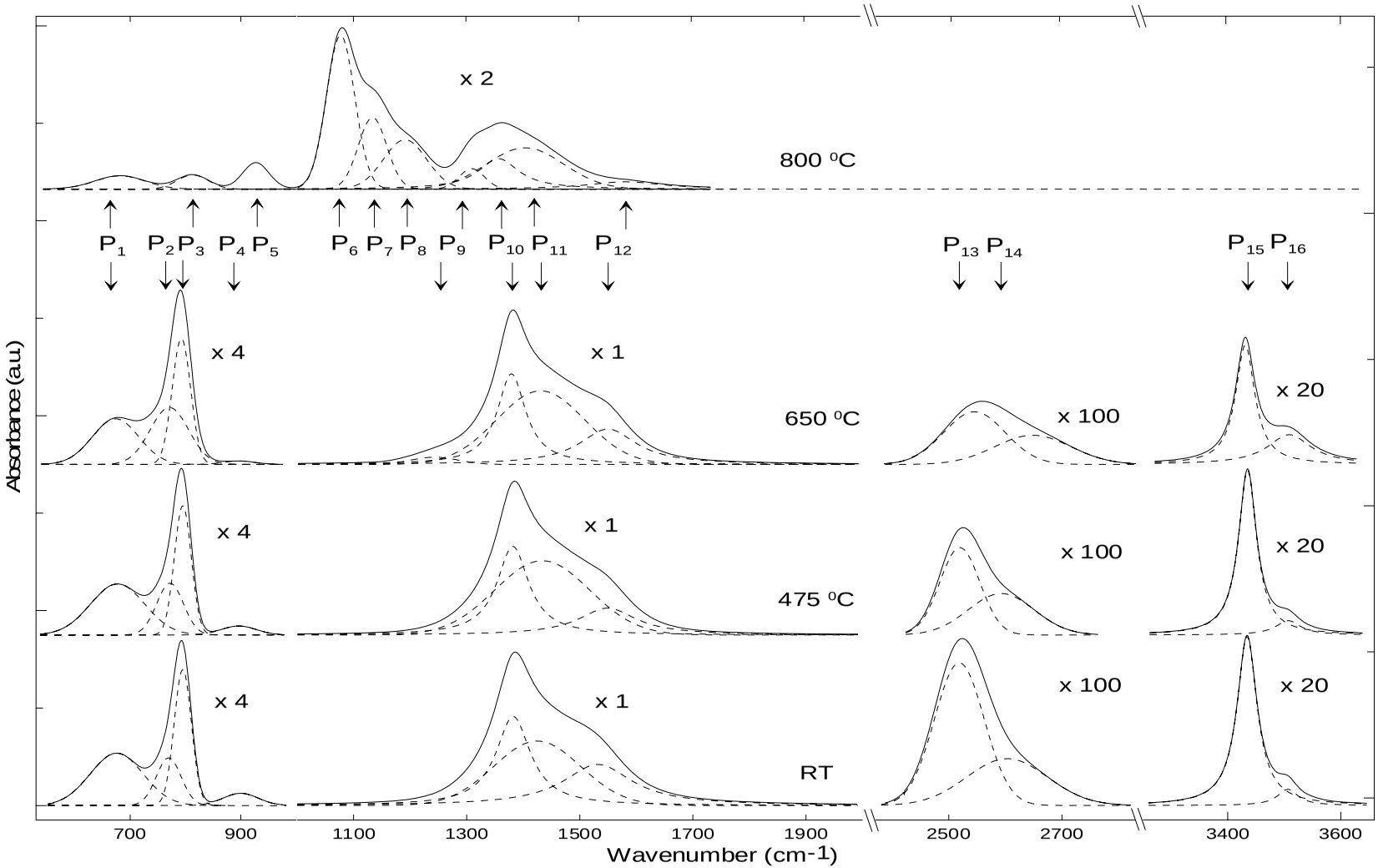

Figure 3.6: Deconvoluted FTIR spectra of as-deposited and annealed (475, 650, 800 ^{0}C) BN films.

Table 3.1. Peaks with their FWHM obtained from the deconvolution of FTIR spectra of BN films and possible assignments of vibrational modes.

	Peak range (cm^{-1})	**FWHM (cm^{-1})**	**Peak assignment**
P1	680	110	B-O-H out of plane bending [40]
P2	770	57	B-N-B out-of-plane bending (TO) [41]
P3	795-813	37-67	B-N-B out-of-plane bending (LO) [41]
P4	900	75	B-H out-of-plane bending [42]
P5	927	55	B-O stretching (BO_4) [43]
P6	1080	60	c-BN stretching (TO) [37] & w-BN [38]
P7	1140	60	w-BN [38]
P8	1200	92	w-BN [38]
P9	1250-1320	98-54	B-O stretching (BO_3) [43]
P10	1365-1380	89-74	B-N in-plane stretching (TO) [41]
P11	1430	150 ($\pm$ 30)	B-O-N [44]
P12	1532-1595	149-166	B-N in-plane stretching (LO) [41]
P13	2520	104	B-H stretching (h-BN) [42]
P14	2600	168	B-H stretching (a-B:H) [45]
P15	3434	40	N-H stretching [42]
P16	3506	50	O-H stretching [46]

assumed to be present because of random orientation of basal hexagonal planar crystallites throughout the t-BN structure. The peak at 795 cm^{-1} is interpreted as the shifted longitudinal optical (LO) vibration mode of h-BN ($B\text{-}N_{(LO)}$) at 828 cm^{-1}. Similarly, the peak at 1532 cm^{-1} might be the shifted $B\text{-}N_{(LO)}$ at 1610 cm^{-1} [47]. As discussed earlier, this LO peak may result from the vibrations of the edges of h-BN clusters present throughout the film [48]. For LO modes to be active at normal incidence of light, the c-axis of h-BN basal planes should not be perpendicular to the plane of the sample. Considering this presence of the LO modes, t-BN films of this study can be assumed to be composed of h-BN clusters (parallel to the substrate

surface), some planes at the edges of which may be oriented at different angles with respect to normal of the sample.

Deconvoluted peaks around 2520 cm^{-1} and 2600 cm^{-1} are related to B-H stretching modes. The lower frequency is the value mostly found for B-H stretching in h-BN films [42], while the higher frequency can be attributed to usually reported 2560 cm^{-1} value for the B-H modes in hydrogenated amorphous boron thin films [45]. Peak at 3434 cm^{-1} is addressed to N-H stretching mode [42]. The small broad peak around 3506 cm^{-1} can be assigned to the O-H stretching of the water molecules which might be present at the surface of the film [46]. Broad peak around 680 cm^{-1} is the out-of-plane bending mode of B-O-H [40], which is also assumed to be mostly on the surface. Peak around 900 cm^{-1} is generally referred to B-H bending mode [42]. Peak around 1430 cm^{-1} obtained after deconvolution can be associated with vibration of B-O-N system [44]. Only for 650 and 800 ^{o}C annealed films, the peaks at 1250 and 1320 cm^{-1} respectively, are detected showing the presence of B-O stretching vibration for trigonal BO_3 units [43].

The spectra of the film annealed 800 ^{o}C contain new peaks. The one at 927 cm^{-1} is assigned to the B-O stretching vibration of tetragonal boron coordination [43]. Also, the wurtzite phase was detected through peaks at 1080, 1140 and 1200 cm^{-1}, close to the ones found earlier [49]. The peak of c-BN was reported to be at 1080 cm^{-1} for the films with high compressive stress [37]. The sample annealed at 800 ^{o}C, which was cracked into consecutive pieces under excessive compressive stress, might be constituted by the coexistence of the c-BN and w-BN phases.

In the literature there exists misinterpretation of the peaks around 1080 cm^{-1}, since the absorbance peak around 1100 and 1050 cm^{-1} together with the shoulder about 1150 cm^{-1} is also a fingerprint of SiO_x structure [37]. However, in this work for two BN films of different thicknesses (380 and 250 nm) annealed similarly at 800 ^{o}C, the intensity of the peak around 1080 cm^{-1} increases proportionally to the thickness. Besides, the BN film is not too thin (380 nm) to be affected by the absorbance intensity of possibly present thin (few nanometers) SiO_x layer at the film substrate

interface. Therefore, it was concluded that peaks around 1080, 1140 and 1200 cm^{-1} are the signature of c-BN and w-BN phases.

The integrated absorption areas ($I = \int \alpha(\omega) d\omega$) of the deconvoluted peaks were used to follow the change in the bond concentrations with the increasing annealing temperature. B-O-H and B-H bending, B-H and N-H stretching bond concentrations decreased with annealing temperature, pointing out the escape of hydrogen atoms from the film. The only hydrogen containing bond, which remains in the film annealed at 800 ^{o}C, is the surface B-O-H bending bond. Surface O-H stretching increases with temperature but disappears at 800 ^{o}C. For B-H stretching bond the decrease is almost due to the peak around 2520 cm^{-1}. Besides this, for 650 ^{o}C annealed film the shift of the peaks at 2520 cm^{-1} and 2600 cm^{-1} to higher frequency values at 2545 and 2650 cm^{-1} respectively occurs. This shift may be due to the increase of the compressive stress (-1.91 GPa). If a solid body is subjected to compressive stress, it will react with a decrease of the bond length and thus with a decrease of its volume. Within the harmonic oscillator model commonly used to describe the bonding (i.e. a linear chain of mass points connected by Hookian springs), in case of no compressive stress, the stretching of the bonds by an amount x_0 results in a restoring force of F_0. Under the compressive stress if the stretching is again at point x_0 the restoring force is now greater than F_0. Consequently, force constant, k, defined as the force per unit length, increases in the presence of a compressive stress. The increase of k value results in a steeper increase of the inharmonic potential around the equilibrium state of the oscillators. Thus, the resonance frequency shifts to higher wavenumbers. However, it should be mentioned that a frequency shift is not exclusively related to compressive stress. Other factors may shift the IR peaks, including film thickness, the degree of crystallinity, the optical properties of the substrate, and deviations in film stoichiometry [50].

The peak around 1380 cm^{-1} is easier to follow if the RT spectrum is subtracted from 475 and 650 ^{o}C spectra (Fig. 3.7). The division of the spectra gives the similar result (Fig. 3.8). Peaks around 1060, 1250, 1380 and 1600 cm^{-1} are increased and become more narrowed with increasing annealing temperature. From the deconvolution it

was also found that the full widths at half peak maximum (FWHM) are decreased for peaks at 1380 cm^{-1} and 1540 cm^{-1} from 74 to 61 cm^{-1} and from 149 to 122 cm^{-1}, respectively, indicating more ordered hexagonal planes. In the film annealed at 800°C B-$N_{(TO)}$ bond concentration decreases drastically while its FWHM increases from 61 to 89 cm^{-1}, with position shifted from 1380 to 1365 cm^{-1}. This accounts for a decrease in the order within h-BN planes, which may be the result of deformation in the network caused by huge compressive stress at 800 ^{o}C. B-$N_{(LO)}$ mode shifts to the higher (from 1532 to 1595 cm^{-1}) and B-N-$B_{(LO)}$ to lower (from 795 to 793 cm^{-1}) wavenumbers as annealing temperature is increased, indicating that θ (angle between the c-axis of the h-BN basal planes and the normal of the sample surface) increases from 0 to 90°, according to Schubert's model [47]. B-N-$B_{(TO)}$ bond concentration increases, while B-N-$B_{(LO)}$ stays the same with annealing temperature. At 800 ^{o}C B-N-B bond concentration decreases drastically, forming a single peak at position shifted to higher wavenumber (813 cm^{-1}). This shift is probably connected with the increase of the stress as described above. It is also worthwhile to look at the increasing peak intensity ratio P_{770}/P_{1380} for RT, 475 and 650 ^{o}C: 0.13, 0.15, and 0.16 respectively. As shown in Fig.3.9 this means that there are more basal planes with c-axis parallel to the substrate surface [37], since only those modes with the vibration axis parallel to the electric field vector can be excited by unpolarized IR light in near normal incidence. This is also supported by the increase in LO mode around 1600 cm^{-1}, indicating more planes at the edges of the h-BN clusters oriented non-parallel to the plane of the sample [47]. The in-plane orientation of these clusters (c-axis parallel to the substrate plane) can be considered to support the increase of the compressive stress in the structure, which eventually trigger nucleation of c-BN and w-BN on the basal planes oriented perpendicularly to the substrate surface for film annealed at 800 ^{o}C [37]. As at 800 ^{o}C the peak around 1400 cm^{-1} is greater in intensity than the one at 813 cm^{-1}, it can indicate that h-BN clusters parallel to the substrate are still present in the network together with wurtzite phase. These last two consequences imply that the nucleation of w-BN is mainly on the thin amorphous tissue.

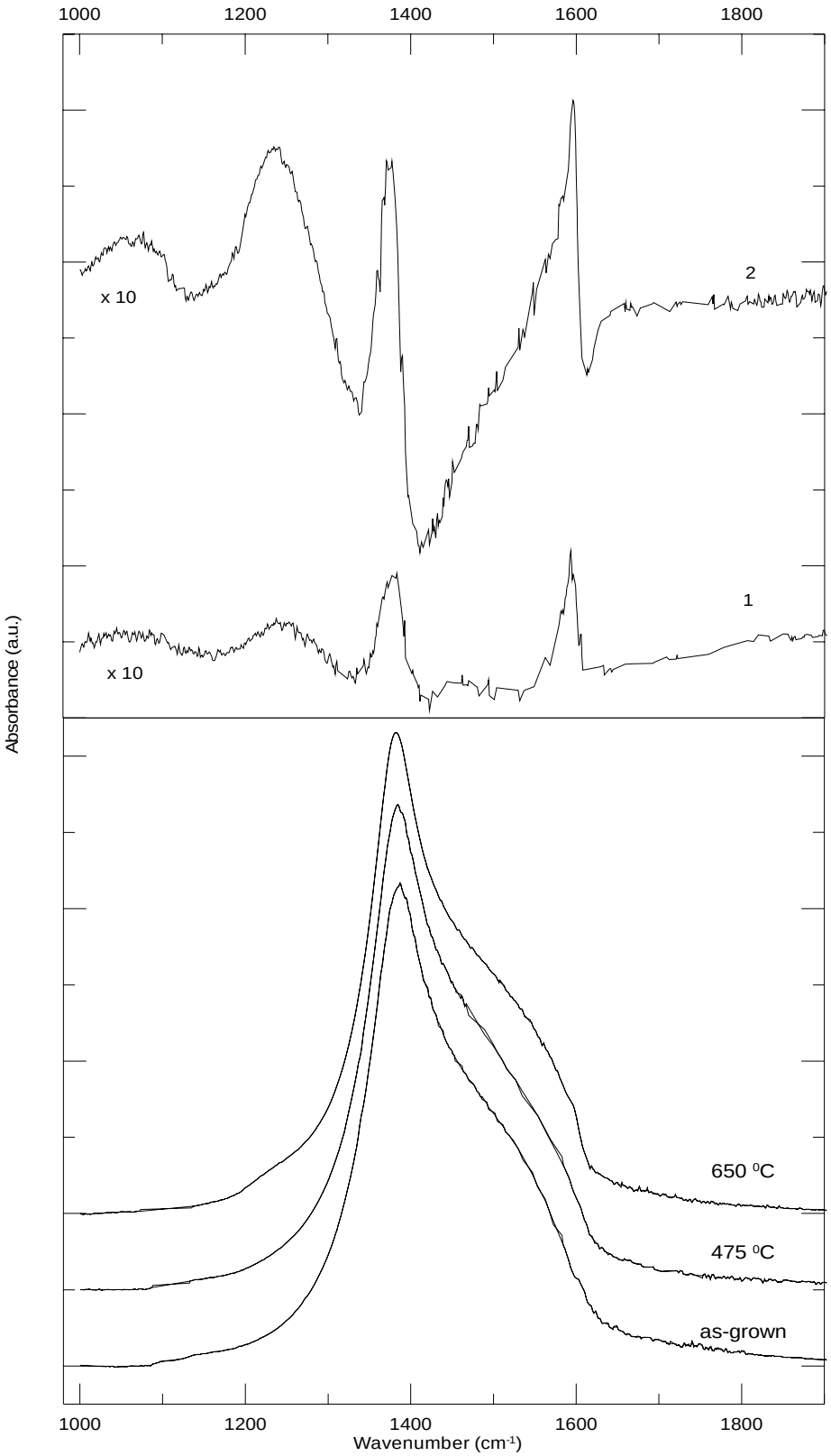

Figure 3.7: Comparison of the FTIR spectra of the films annealed at both 475 ^{0}C (1) and 650 ^{0}C (2) with that of the as-grown sample by subtraction of spectra.

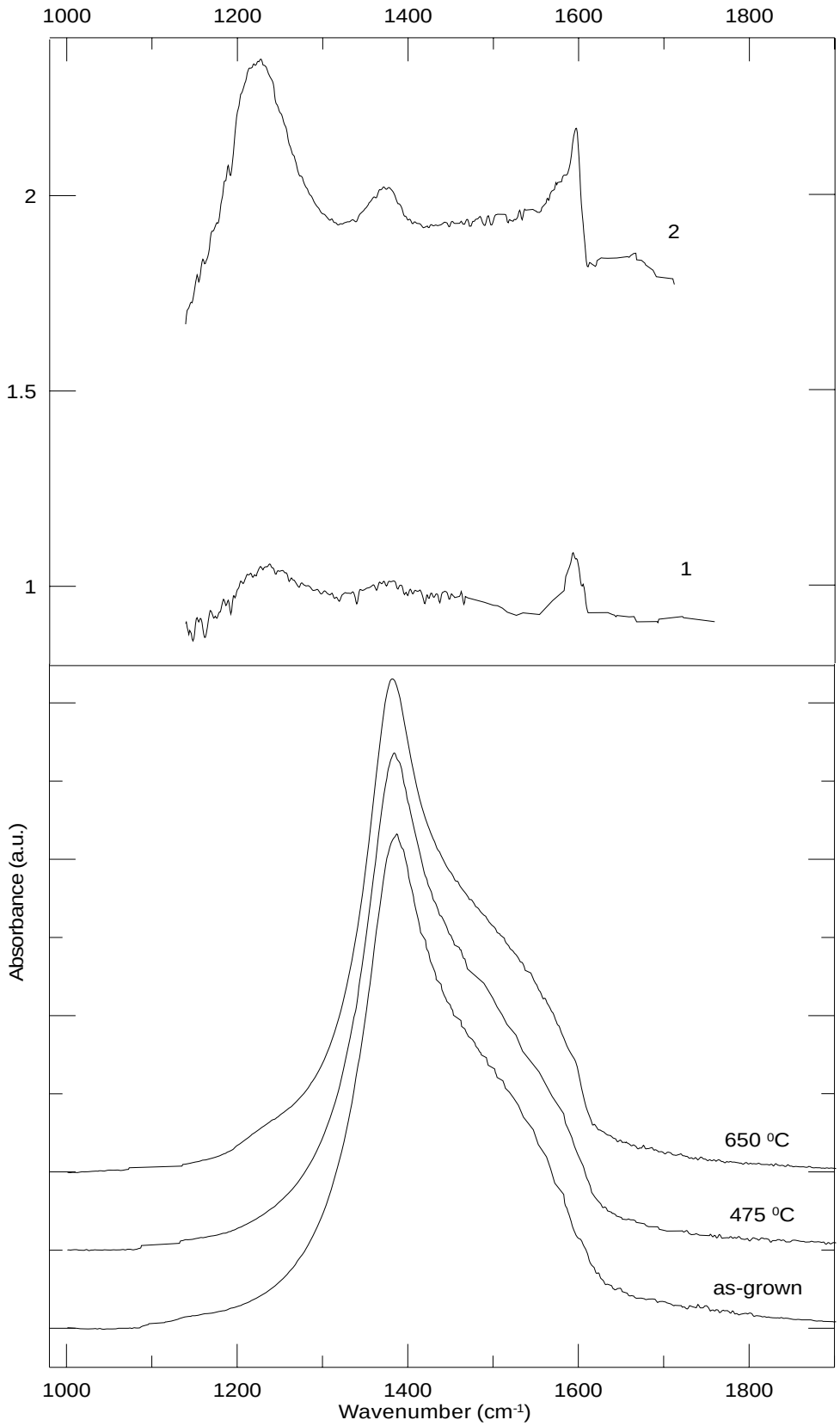

Figure 3.8: Similar comparison of spectra as in Fig. 3.7 by normalizing the spectra of the annealed samples 475 ^{0}C (1), 650 ^{0}C (2) to the one of as-grown sample.

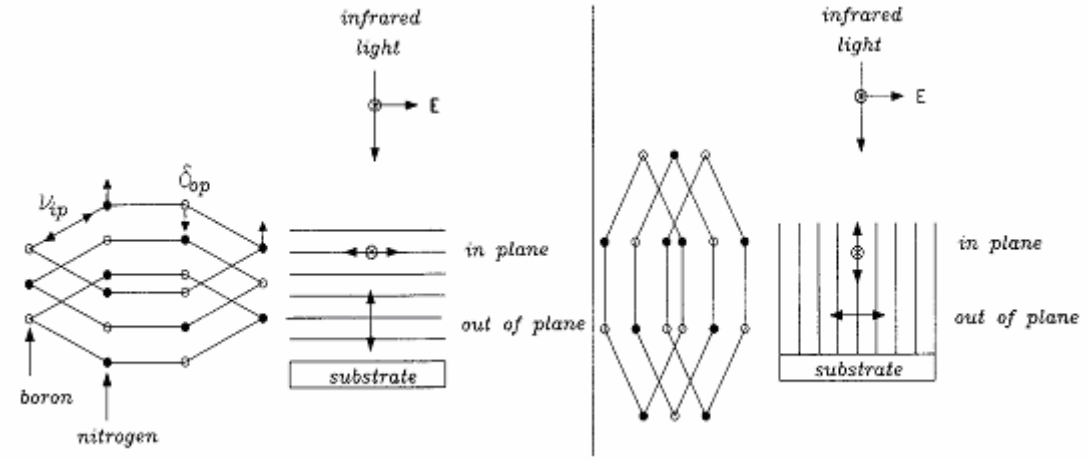

Figure 3.9: Schematic diagram of the infrared active modes in h-BN and the relationship of the vibration axis of these modes to the electric field vector of unpolarized light for horizontal and vertical arrangements of the h-BN layers [50].

The oxygen incorporation into the film in the form of trigonal boron units BO_3 starts at 475 ^{o}C (1250 cm^{-1} peak, Fig. 3.7). When wurtzite and cubic phases are formed at 800 ^{o}C, BO_4 units appear together with BO_3 ones, the former being greater in absorption intensity. Since w- and c-BN are the four coordinated structures, the formation of boron tetragonal coordination BO_4 can be the result of incorporation of oxygen atoms to saturate part of the dangling bonds of wurtzite structure. Similarly, three coordinated structure of t-BN, still present at 800 ^{o}C, may promote BO_3 formation.

Apart from identifying the phases present in BN films FTIR spectroscopy technique is also suitable to quantify the c-BN volume fraction, which is roughly given as:

$$c\text{-}BN\ volume\ fraction \approx \frac{P_{1080}}{P_{1080} + P_{1380}} \tag{3.1}$$

where P_{1080} and P_{1380} are the normalized reflected or transmitted IR absorbance peak intensities at approximately 1080 and 1380 cm^{-1}, respectively [37]. However, application of this formula gives only a very rough approximation due to the fact that

h-BN (sp^2-bonded BN in general) is not isotropic. As the t-BN interlayer present in almost all ion beam deposited c-BN films, has its basal planes perpendicular to the substrate surface, the out-of-plane 780 cm^{-1} mode is enhanced compared to the in-plane 1380 cm^{-1} mode. Thus, 1380 cm^{-1} mode is infrared inactive for the planes perpendicular to substrate surface (Fig. 3.9) and then, the c-BN content is most often overestimated. For mixed sp^3 phases (w-BN and c-BN) existing in the film annealed at 800 ^{0}C the extended formula [51] can be used:

$$sp^3 - bonded\ BN\ phase\ volume\ fraction \approx \frac{I_{1080,\ 1140,\ 1200}}{I_{1080,\ 1140,\ 1200} + I_{1320,1365,1430,1595}} \tag{3.2}$$

where $I_{1080,\ 1140,\ 1200}$ and $I_{1320,1365,1430,1595}$ are the integrated absorption areas of the corresponding peaks for sp^3- and sp^2-bonded phases, respectively. The sp^3-bonded volume fraction was estimated to be 56.9 % for film annealed at 800 ^{0}C.

To calculate hydrogen content in films, oscillator concentration N was calculated:

$$N = A\frac{I}{\omega} \tag{3.3}$$

where A is the proportionality factor and ω is the peak frequency. For N-H bonds $A = 2.8\times10^{20}\,cm^{-2}$, as it was determined from $a-SiN_x:H$ films [52]. For B-H stretching and bending bonds the determination of A was based on equation [45]:

$$N_{B-H} = \frac{cn_0\mu_{B-H}}{2\pi^2 e_s^{*2}} I \tag{3.4}$$

where c is the velocity of light, $n_0 = 1.78$ is the refractive index of the BN film, $\mu_{B-H} = 0.92$ reduced mass, e_s^* is the effective charge. The local field correction of the effective charge led to $e_s^* = e_g^*\varepsilon_m$ (where $e_g^* = 0.2$, $\varepsilon_m = n_0^2$) [45]. The

proportionality constant N_{B-H}/I was obtained to be $4.61\times10^{16} cm^{-1}$. Assuming the oscillator strength to be equal for both stretching and bending B-H bonds, the concentrations for B-H bending, B-H and N-H stretching bonds were determined as a function of annealing temperature (Fig. 3.10). The O-H bonds were not taken into account, because of their surface rather than bulk nature. From Fig. 3.10 it can be concluded that hydrogen bonded boron atom density decreases more rapidly than the nitrogen atom density, which was also observed by Z. L. Akkerman et al. for low temperatures (below 650 ^{o}C) [47]. The total concentration of hydrogen containing bonds results in hydrogen atom density, which decreases with the increasing annealing temperature. Since FTIR spectra for RT, 475 and 650 ^{o}C resulted in the noticeable change of only hydrogen oscillators, the changes in the mechanical stress of the film are expected to be related to the decrease of hydrogen amount. The relationship between stress and hydrogen atom density was established to be almost linear for the RT - 650 ^{o}C temperature region (Fig. 3.11). The decrease of hydrogen atom density in films can account for the increase in dangling bond amount in the films. Dangling bonds associated with boron atoms can be saturated with those of nitrogen atoms by forming B-N bond. This B-N formation may complete the hexagonal planes at the edges of the clusters (with c-axis not perpendicular to the substrate surface), therefore increasing bond distortion in the network leading to more stressful structure. Besides the formation of B-N bonds by the dangling bonds, left boron atoms may form B-N bonds with the nitrogen atoms of N_2 gas used during annealing process. In any case B-N bond formation is promoted with increasing annealing temperature, while hydrogen amount in films is decreased. For 800 ^{o}C annealed sample hydrogen is only present on the surface of the film. In this respect, the relaxation of coordination defects by hydrogen saturation is totally eliminated. Then, the film structure became expectedly cracked due to internal stress.

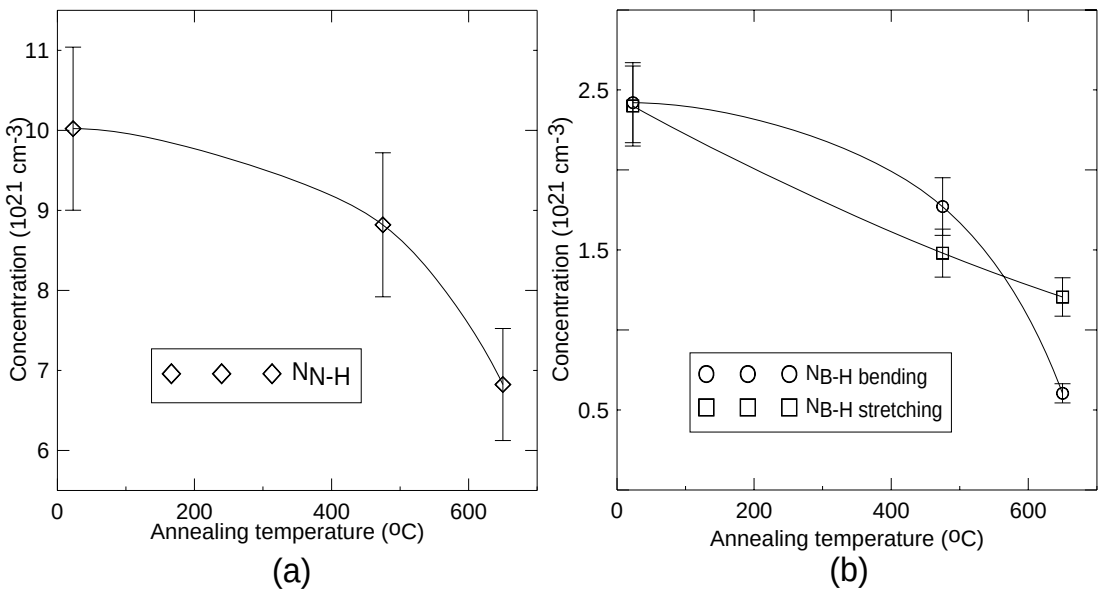

Figure 3.10: Evaluated concentrations for (a) nitrogen-hydrogen, (b) boron-hydrogen oscillators of BN film as a function of annealing temperature.

The reduced absorption intensity at 800 ^{o}C may stem from the fact that the infrared light is partially focused on the possible film-free regions created by the cracking of the film (Fig. 3.1). Besides, this reduction in absorbance might be due to the decrease in thickness of the film. One possible reason for decrease of thickness might be the peeling off of the films as a result of high stress.

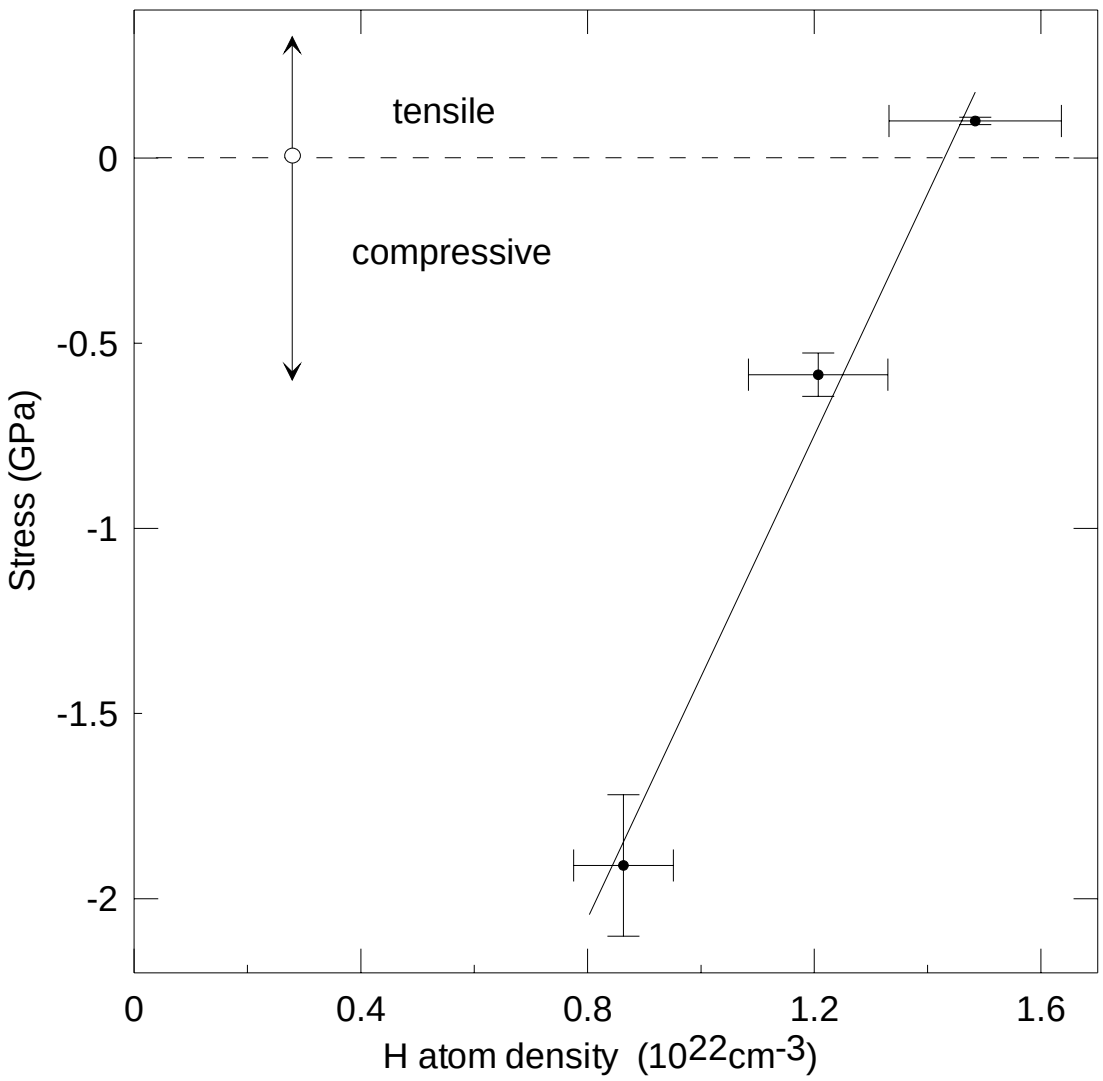

Figure 3.11: Variation of stress with calculated total hydrogen atom density for BN film at RT, 475 and 650 ^{0}C.

3.3.2 Plasma Chemistry

In plasma environment gas molecules lose some of their electrons or atoms as a result of the collisions with charged plasma species. Then, the created ions are accelerated through the ground electrode under the radio frequency (r.f.). These ions are responsible for the film deposition and therefore study of the plasma chemistry is unavoidable for understanding the film growth process.

Let us first focus on the reactions in the gaseous phase. Adding ammonia (NH_3) to diborane (B_2H_6) gives different compounds depending on the mixture ratio and temperature. At the room temperature (RT) a stable white solid borohydride, the diammoniate of diborane $\left[H_2B\left(NH_3\right)_2\right]^+\left[BH_4\right]^-$, is produced (Figure 3.11, Eq. 3.2). Another product at the RT is $H_3B \cdot NH_3$ (Eq. 3.1), which sublimates just above the RT eliminating hydrogen molecule to form aminoborane $H_2B = NH_2$ (Eq. 3.3). For temperatures above 200 ^{0}C borazine $B_3N_3H_6$ is produced together with some boranes of form $\left(BNH_2\right)_n$ (Eq. 3.4). While temperature is increased, hydrogen is eliminated, then, $\left(BNH\right)_n$ (Eq. 3.5) and finally BN (Eq. 3.6) is left [42].

$$\text{RT}\begin{cases} B_2H_6 + NH_3 \rightarrow H_3B \cdot NH_3 & (3.1) \\ B_2H_6 + NH_3 \rightarrow [H_2B(NH_3)_2]^+[BH_4]^- & (3.2) \end{cases}$$

$$\text{increasing T} \downarrow \quad \begin{array}{ll} B_2H_6 + NH_3 \rightarrow H_2B = NH_2 + H_2 & (3.3) \\ B_2H_6 + NH_3 \rightarrow B_3N_3H_6 + H_2 + \text{solid boranes} & (3.4) \\ B_2H_6 + NH_3 \rightarrow (BNH)_n + H_2 & (3.5) \\ B_2H_6 + NH_3 \rightarrow BN + H_2 & (3.6) \end{array}$$

Figure 3.12: Compounds created as a result of gas mixture of diborane and ammonia [42].

In the presence of capacitively coupled r.f. plasma NH_3 and B_2H_6 mixture shows strong modifications if compared to its gas phase. The dissociation of reactant gases occurs. White solid (diammoniate of diborane) disappears. Also, new BN-containing, BH_y $\left(y \leq 4\right)$ and NH_z $(z \leq 2)$ radicals are created, indicating the aminoborane ($H_2B = NH_2$) production [42]. It can be then deduced that the film growth in the case of NH_3 and B_2H_6 mixture may be due to the B- and N- containing species that already exist within the plasma.

3.4 Summary

Hexagonal boron nitride (h-BN) thin films are deposited by PECVD using ammonia (NH_3) and diborane (B_2H_6) as source gases. On one side B_2H_6 is diluted in hydrogen (15% B_2H_6, 85% H_2) on the other side both source gases contain hydrogen atoms, the deposited BN film may be considered "hydrogenated" and then hydrogen content within the film is expected to affect the physical properties. In this respect, hydrogen atom concentration has been estimated for the films annealed at 475, 650 and 800 ºC. The hydrogen concentration is observed to gradually decrease by heat treatment; parallelly, internal compressive stress of the films increases with increasing annealing temperature. In other words, the linear dependence of stress on hydrogen atom density implies that the hydrogen atoms should relax the network by first breaking the overstrained (and then weakened) bonds under stress and by then saturating them. Consequently, the release of hydrogen due to annealing process, both recreate partly the dangling bonds and partly reconstruct the strained bonds. These strained bonds lead to the increase of stress and Urbach energy. Increasing Urbach energy is known to decrease the band gap energy. However, BN bond promotion together with increased order within the hexagonal clusters (not the whole film structure) with increasing annealing temperature should tend to increase the energy gap. These two last consequences seem to compensate each other since the energy gap of the BN films at hand remains almost constant. At 800 ºC, hydrogen seems to be totally removed from the system and phase transition from hexagonal to wurtzite (mixed with hexagonal and possibly cubic phases) boron nitride (w-BN) is observed. In addition, high compressive stress, which is expected for wurtzite phase, leads to cracking of the film.

It was also observed that during the deposition processes (with ammonia and diborane as sources) the reaction described in Eq. 3.2 occurs and leads to the precipitation of white powder inside those gas tubes that are combined before reaching the chamber. Unfortunately, the PECVD system at hand can not afford to carry these gases in different tubes within the chamber. Therefore, in the following depositions of BN films ammonia source gas is replaced by nitrogen gas.

CHAPTER 4

RESULTS AND DISCUSSIONS ON BN FILMS USING NITROGEN

4.1 Introduction

Ammonia and diborane gases react at room temperature outside the reactor, in the tubing, to form solid state compounds [53]. This phenomenon, which was presented in Chapter 3, caused serious problems within the deposition system during the production and ammonia is replaced by nitrogen gas. Nitrogen gas does not react with diborane. It is also commercially cheaper and easily available. Besides, it was reported that the deposition rate in nitrogen case is greater than that in ammonia case [42]. Therefore, the subsequent depositions are performed by nitrogen and diborane as source gases.

4.2 Production

Three sets of boron nitride (BN) thin films are deposited with different N_2/B_2H_6 flow ratios by plasma enhanced chemical vapor deposition (PECVD), as described in Chapter 2. The deposition parameters for the sets are given in Table 4.1. In order to increase the ion bombardment rate on the surface negative d.c. bias voltage is applied on the bottom electrode of PECVD. The variations of physical properties in different deposition sets are analyzed by optical, mechanical and electrical measurements using FTIR, X-ray photoelectron (XPS) and UV-visible spectrometers, a mechanical stylus profilometer and a current-voltage (*I-V*) system.

Table 4.1: The parameters used for the depositions. All the depositions were performed with pressure 0.1 Torr, power 200 W, temperature 250 ºC and ground electrode dc bias voltage -300 V.

Sample	F (N_2) (sccm)	F (B_2H_6, 15% in H_2) (sccm)	Flow Ratio ($r = N_2/B_2H_6$)
BN1	18	30	4
BN2	30	20	10
BN3	40	10	25

It is seen from Table 4.1 that N_2/B_2H_6 flow ratio is increased from $r = 4$ to $r = 25$ as follows: N_2 flow rate is increased while B_2H_6 flow rate is decreased so as to keep the total flow rate in the reactor constant under the pressure of 0.1 Torr. Therefore, as N_2/B_2H_6 increases from $r = 4$ through $r = 25$, boron amount within the reactor becomes more deficient.

4.3 Deposition Rate and Mechanical Stress

Although high deposition rate is desirable for lower cost, it does not always result in good quality films [54]. On the other hand, possible deposition rate variations along the radial direction of a plasma electrode (Fig. 4.1) remain one of the drawbacks to be surmounted. Such nonuniformities may give insight into the physical dynamics inside the system [55], [56]. Moreover, a thickness distribution might lead to the microscopic structure and composition inhomogeneity of the film.

Thicknesses of the films were measured by mechanical stylus profilometer with error $\leq 10\%$. These values were used for mutual control of the thicknesses and refractive indices found via decomposition of the optical path, $n \cdot d$ measured by UV-visible spectrometer. A minimization program, OPTICHAR was used to decompose the optical path [57].

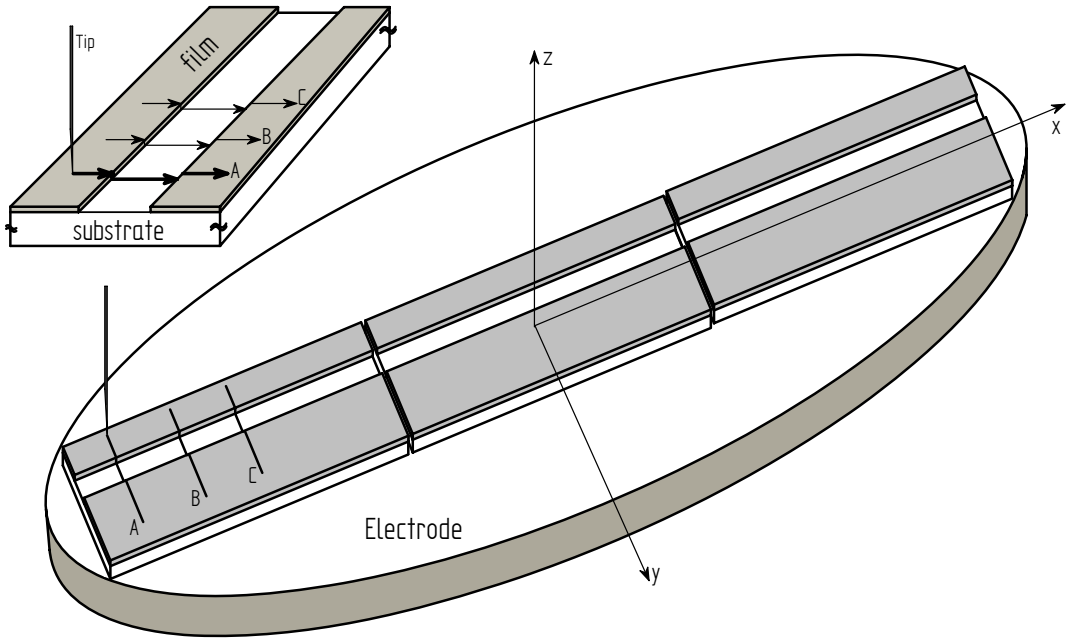

Figure 4.1: The glass substrates were placed along the radius of the lower electrode of PECVD system. Grooves were created placing relatively thin glass shadow masks on the substrates prior to the deposition. The tip path of the profilometer is such that the thickness can be easily seen from the profile data.

Deposition rates were found by dividing thicknesses to the deposition times. At the edge of the electrode, the deposition rate decreases with increasing *r* as: 9.7, 8.9 and 5.3 nm/min for *r* = 4, 10 and 25, respectively. The variations of deposition rates along the reactor radial direction seem to depend on the flow ratios *r* (Fig. 4.2). The sample with *r* = 25 shows the larger distribution magnitude (which is defined as the difference between the deposition rates at the center and at the edge of the electrode), where the deposition rate gradually decreases from the center towards the edge. Despite the presence of some waviness or roughness, the distribution magnitude is gradually reduced when *r* decreases to 4 (see Fig. 4.2).

Mechanical stress measurements exhibit compressive stress and no significant change with increasing *r*: 0.38, 0.34 and 0.39 GPa.

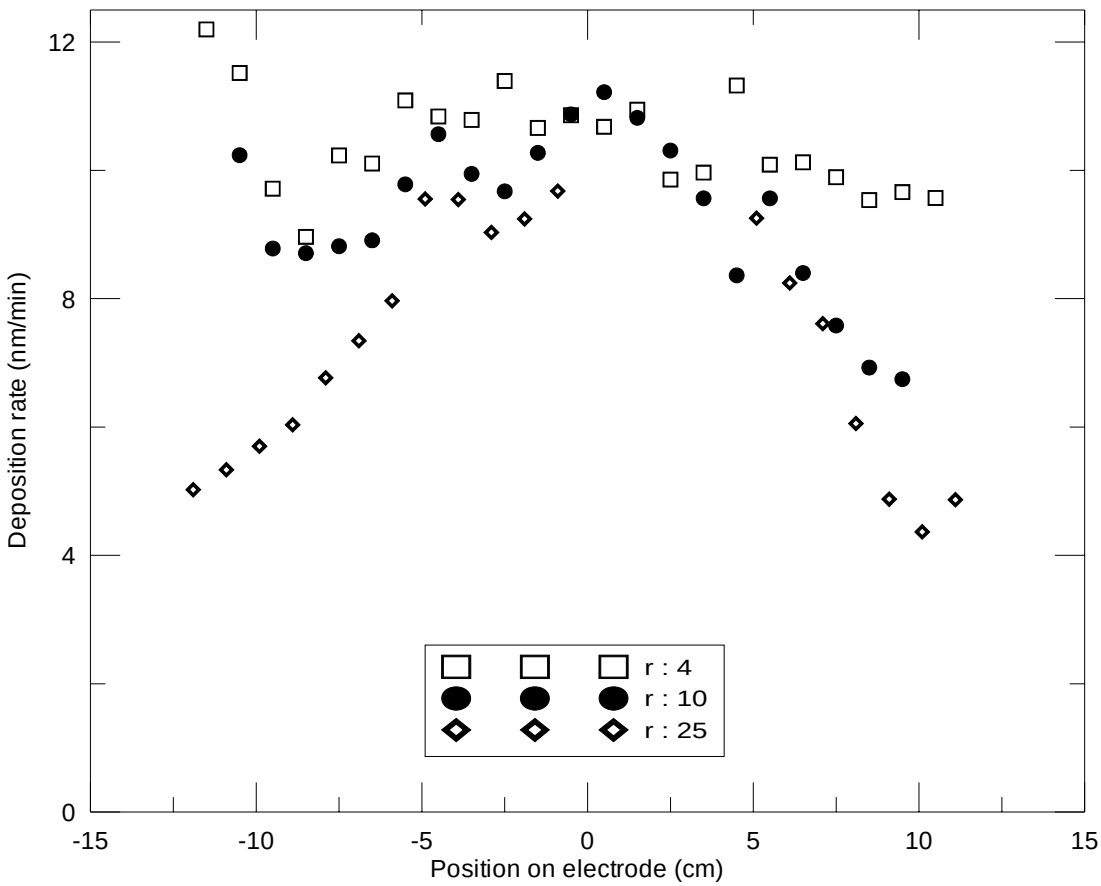

Figure 4.2: Deposition rate variations of three BN films prepared with $r = N_2/B_2H_6$ flow ratios 4, 10 and 25, along the radial direction of the ground electrode. Position ´zero` indicates the center of the electrode.

4.4 Discussions

4.4.1 Deposition Rate Measurements

It was mentioned earlier that there are several nonuniformity sources along the reactor radius such as perturbation of electric field lines at the electrode edges [55], standing wave effect [58], plasma potential nonuniformity [59], gas injection distribution [60], etc. In the literature, it was reported that boron is the limiting factor of BN film deposition rates and that the growth rate of pure boron was assumed to be

higher than that of BN [61]. Thus, greater number of boron atoms at the center of the reactor relative to the edges observed by IR spectra can be a confirmation of this hypothesis. Thus, for lower B_2H_6 flow rate, through edge of the reactor boron amount inside the system might be assumed to decrease. Reduction of deposition rate towards the edge of the electrode seems to be preferred instead of promoting nitrogen rich film structure. In this boron deficient environment, supposing B-H bonds to have smaller energy relative to B-N ones, B-H bonds might be broken by nitrogen and hydrogen etching [62]. B-H radicals return to the plasma from the film surface. Then, B-N bonds can be formed on the surface, whose energies are much higher, thus are relatively harder to be etched by bombardment (to be consistent with the plasma chemistry, discussed in Section 4.4.4). Deposition rate limited by B_2H_6 flow rate mostly explains the differences in the nonuniformity characteristics of the films along the reactor radial direction. As boron amount becomes more efficient (from r = 25 to r = 4) the distribution magnitude decreases and instead of the deposition rate limitation, a wavy and randomized growth rate is observed along the radius. This waviness may reflect that the bonds of the films prepared by higher B_2H_6 flow rate are more affected by the electrodynamics within the reactor (Fig. 4.2).

4.4.2 XPS Measurements

The XPS technique was used to estimate the main atomic compositions of the BN films at hand. In this Chapter, the relative ratio of N_2 flow rate to B_2H_6 one was increased systematically to carry out the effects of N_2 flow on the composition and properties of the films. Although the compositional variations of B and N atoms obtained from XPS analysis seems small when r increases, a weak tendency towards stoichiometry is observed (Table 4.2). Apart from B and N constituents, serious unintentional oxygen content was detected in the BN films. The deconvolution of the main peaks of B1s, N1s and O1s are shown in Fig. 4.3. Oxygen presence in the films is probably due to a leakage in the reactor during deposition or an atmospheric contamination by diffusion through the surface subsequent to the deposition. The later one seems probable due to a sudden diffusion through the interlayer spacing of the hexagonal structure either saturating the dangling bonds of boron or binding

boron atoms at the nitrogen sites [63]. Eventual oxygen diffusion should be relatively rapid since the IR transmittance of the samples showed no evolution between the first day and 80 days after the deposition.

Table 4.2: Elemental composition and bond concentration percentages obtained from XPS analysis.

	%			Ratio			B 1s			N 1s		O 1s	
r	B	N	O	O/B	O/N	B/N	B-B	B-N	$B\text{-}O_x(\text{-}N_y)$	N-B	$N_y\text{-}O_x(\text{-}B)$	N-O	$B\text{-}O_x\text{-}N_y$
4	55.21	35.38	9.41	0.17	0.27	1.56	23.6	66.9	9.6	40.8	59.1	45.4	54.6
10	55.44	35.62	8.94	0.16	0.25	1.56	16.2	69.7	14.1	42.9	57.1	37.6	62.4
25	51.73	36.39	11.88	0.23	0.33	1.42	6.5	74.1	19.3	46.9	53.1	21.5	78.5

B1s peak could be deconvoluted into three sub-peaks located at 188.0, 190.5 and 191.5 eV corresponding to B-B, B-N and $B\text{-}O_xN_y$ $\left(B\text{-}O_xN_{3\text{-}x}\right)$ bonds, respectively [54], [62], [64], [65], [66], [67], [68], [69]. B-B bond peak area is decreased while B-N and $B\text{-}O_xN_y$ areas are increased with increasing relative N_2 flow ratio. At 397.9 and 399.7 eV of N1s peak there are N-B and $N_y\text{-}O_xB$ $\left(N\text{-}O_xB_{3\text{-}x}\right)$ sub-peaks, respectively [54], [63], [64], [67], [70], [71]. From Table 4.2, N-B peak area increases and $N_y\text{-}O_xB$ peak area decreases as the N_2 flow rate is increased. Increasing $B\text{-}O_xN_y$ in B1s and decreasing $N_y\text{-}O_xB$ in N1s indicates that *'y`* is getting smaller. The decrease in the coalescence of N atoms in the ternary $B\text{-}O_xN_y$ or $N_y\text{-}O_xB$ structure and decrease in B-B bonds are probable to lead to an increase in B-N peak area leaving B/N ratio unchanged. It might be thought that B-B acts as boron source and both $B\text{-}O_xN_y$ and $N_y\text{-}O_xB$ ternary structures act as nitrogen sources for the B-N formation. This explanation is supported by the evolution of O1s sub-peaks located at 531.5 and 533.0 eV corresponding to N-O and B-O peaks, respectively [69], [72]. Increasing N_2 flow rate results in fewer N-O bonds and more B-O bonds. The full width at half maximum of B-O peak is 2.4 eV and that of N-O

peak is 4.3 eV. In this respect, N-O bonds within the structure should be relatively more distorted and B-O bonds should be promoted if a more ordered structure is reached by increasing N_2 flow rate.

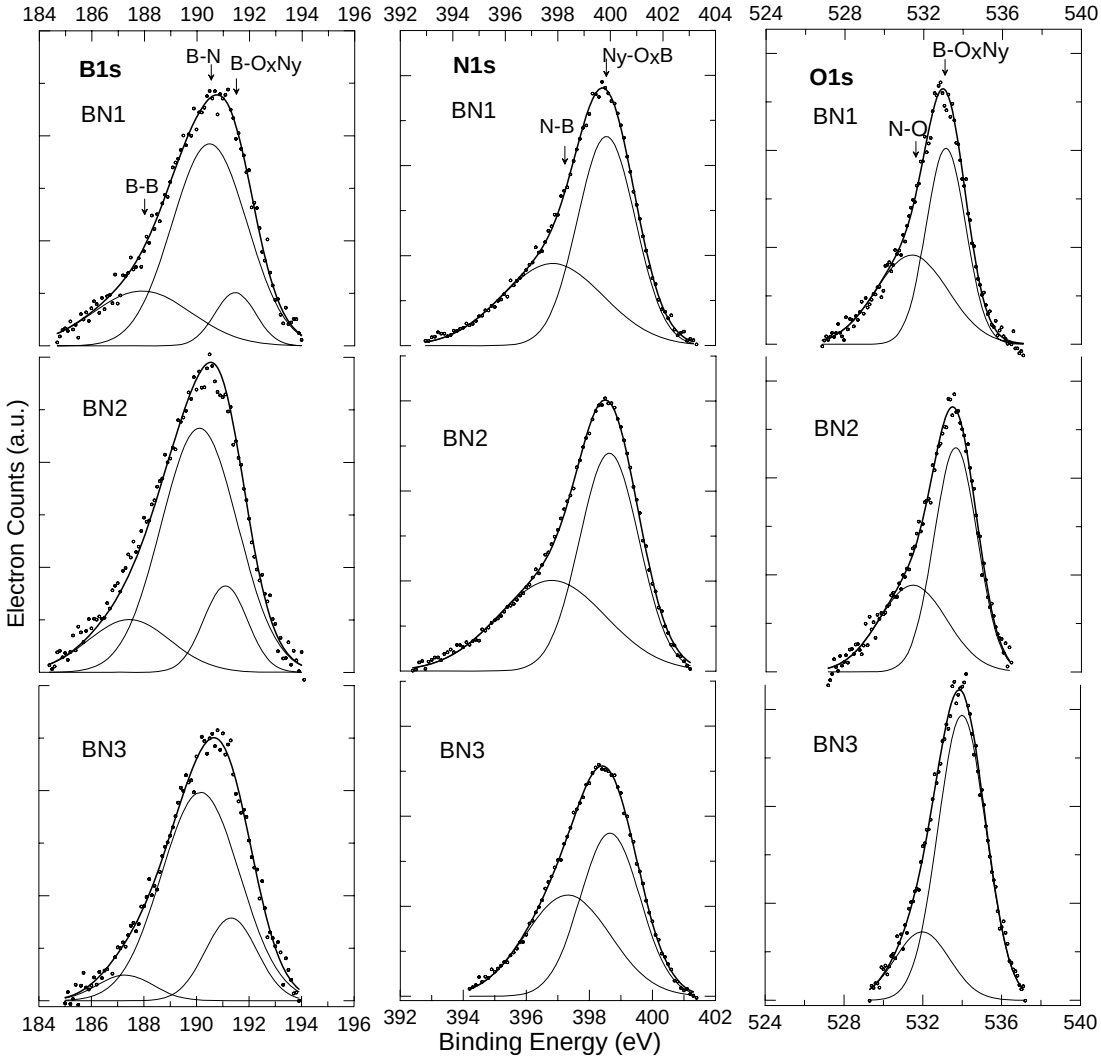

Figure 4.3: XPS analysis of (a) B1s, (b) N1s, and (c) O1s peaks. Circles show the original data and bold line is the fit obtained from deconvolution.

As a result of the XPS analysis, despite the B/N ratio does not significantly change, regardless of a slight decrease with increasing N_2 flow, B-N bond formation is preferred where B and N atoms are supplied as a result of internal conversion of

bonds from other configurations. Increasing relative N_2 flow seems to be acting as a catalyst for the formation B-N bonds. However, oxygen incorporation into the network creates very stable B-O bonds and prevents the composition form approaching the stoichiometry.

4.4.3 FTIR Measurements

The deconvoluted FTIR spectra are shown in Fig. 4.4. The deconvolution of the spectra was done similarly to the case of as-deposited BN films discussed in Chapter 3 (Fig 4.4). The results of FTIR spectra are consistent with the XPS analysis. In addition, it provides information about hydrogen evolution of the films with increase of the relative nitrogen flow rate. Peak around 1385 cm^{-1} is related to in-plane B-N stretching transverse optical mode of vibration ($B\text{-}N_{(TO)}$) and the one near 780 cm^{-1} to out-of plane B-N-B bending mode; both peaks being the characteristic peaks of sp^2 bonded h-BN films. No evidence of the sp^3 bonds (cubic BN), that result in peak around 1065 cm^{-1}, was detected. There are also absorption bands around 2520-2580 cm^{-1} and 3439 cm^{-1}, corresponding to B-H and N-H stretching modes respectively. Peak around 910 cm^{-1} is generally referred to B-H out-of plane bending mode. Peak around 1420 cm^{-1} obtained after deconvolution can be attributed to vibration of angular B-O-N system. The other absorbance peak near 1530 cm^{-1} can be considered is the shifted $B\text{-}N_{(LO)}$ at 1610 cm^{-1}. As it was discussed in Chapter 3, LO peak may result from the vibrations of the edges of h-BN clusters present throughout the film. So, again, BN films can be deduced to be composed of h-BN clusters with some planes at the edges of the clusters oriented at different angles with respect to normal of the sample. B-N bond concentration (near 780 cm^{-1} and 1385 cm^{-1}) increases with increasing nitrogen flow rate, keeping the ratio I_{780}/I_{1385} almost the same. This means that only the amount of h-BN basal planes inside the clusters increases holding the orientation of planes almost the same, i.e. increase in size of the clusters. According to the B-O-N peak area the oxygen amount can be deduced to slightly increase with the increase of N_2/B_2H_6 flow ratio. Also, N-H stretching bond concentration increases. On the other hand, B-H stretching and bending bond amount decreases, which can be the consequence of the effective nitrogen etching.

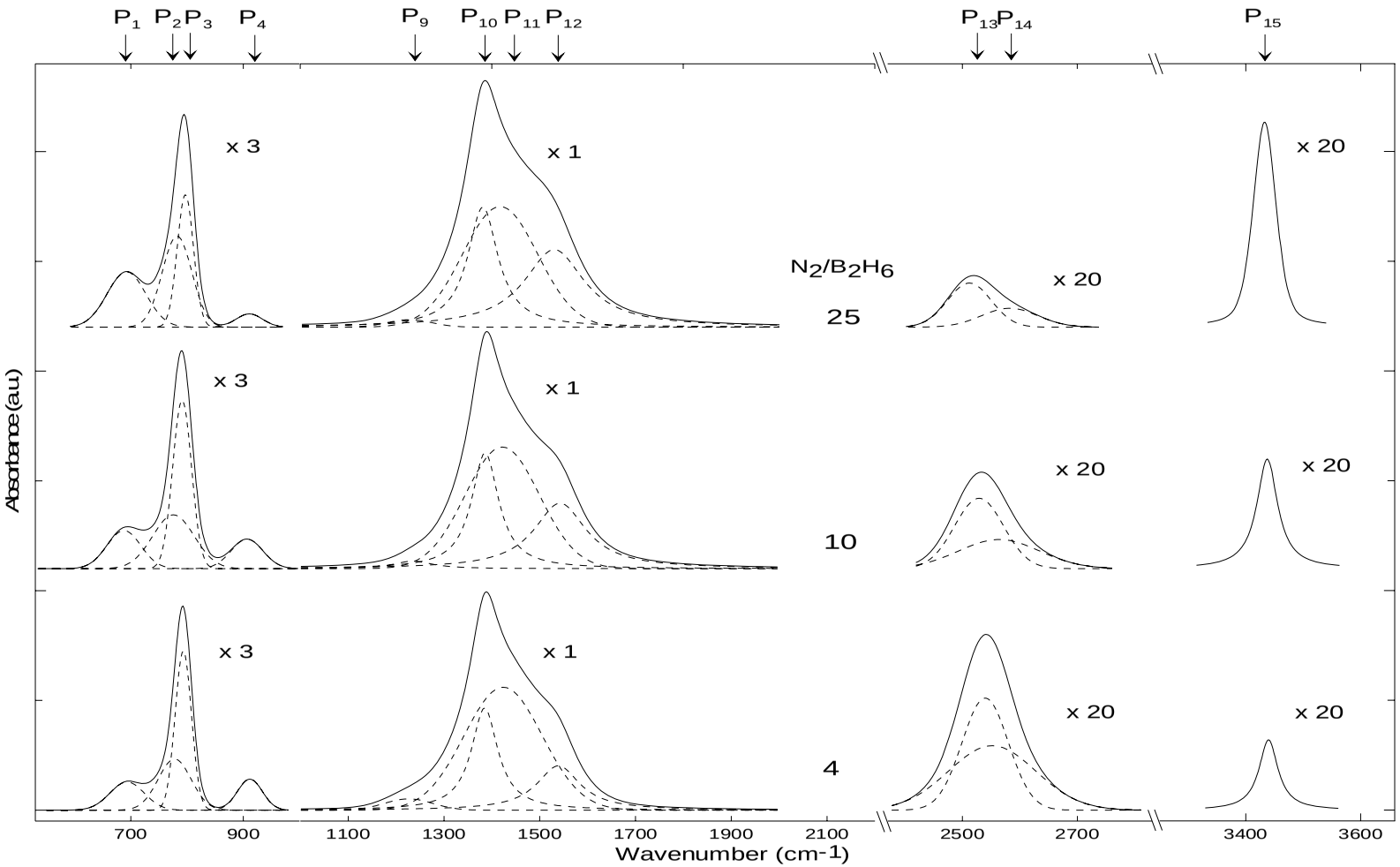

Figure 4.4: Deconvoluted FTIR spectra of as-deposited BN films with different N_2/B_2H_6 flow ratio. Absorbance is normalized to the film thicknesses.

The slight increase in LO mode around 1530 cm^{-1} with the increased *r* indicates that more planes at the edges of the h-BN clusters in films prefer to be oriented non-parallel to the plane of the sample.

Hydrogen content evaluation in the films was found by the use of the proportionality constants calculated in Chapter 3. The concentrations for B-H bending, B-H and N-H stretching bonds were determined as a function of N_2/B_2H_6 flow ratio (Fig. 4.5). The total concentration of these hydrogen containing bonds results in hydrogen atom density, which decreases with the increased *r* (Fig. 4.4). This decrease of hydrogen atom density in films can account for the decrease in total amount of dangling bonds associated with boron atoms. These bonds are saturated with nitrogen (B-N bonds) instead of hydrogen while the *r* increases, forming more hexagonal planes and increasing the cluster size. This may cause the decrease in amorphous tissue between the clusters and lead to the increase of the ordering of the films.

At this stage, it would be useful to correlate hydrogen amount with stress as was done in chapter 3. However, similar stress values with increasing *r* indicate that the amorphous layer, assumed to exist at the interface (See Section 1.1), should not be affected by the reduction of hydrogen amount. Consequently, the major variations of bond configurations should occur at the bulk of the film, not at the interface.

The FTIR measurements conducted 80 days after the deposition, resulted in the same spectra, indicates that films are stable within humid atmosphere.

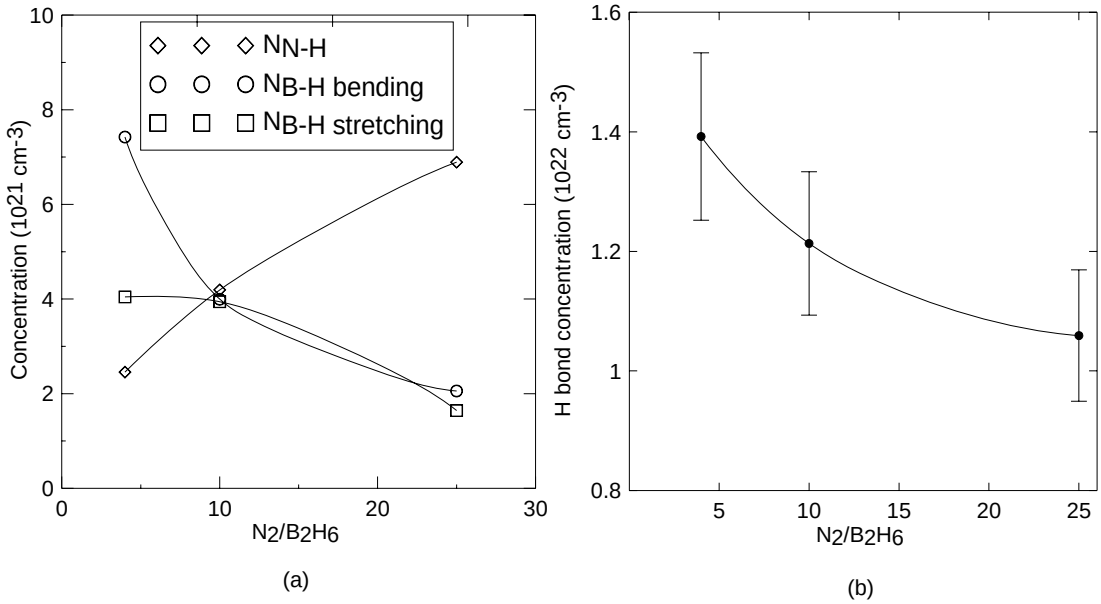

Figure 4.5: Using FTIR spectra both concentrations of various hydrogen containing oscillators (a) and total hydrogen atom concentration (b) in the BN film are plotted as a function of N_2/B_2H_6 flow ratio.

4.4.4 Plasma chemistry

Besides the r.f. voltage, negative dc bias voltage was applied to the ground electrode to further increase the acceleration of the plasma charged species. This is supposed to create ion bombardment on the surface of the film, necessary for the formation of the cubic phase. Unfortunately, by this set of conditions the formation of cubic structure in measurable fraction could not be succeeded since no proper IR signal was able to be detected in the BN films.

In the mixture of nitrogen gas with diborane no gas phase reaction results. For N_2 and B_2H_6 mixture in the presence of r.f. plasma, dissociation of diborane and creation of BH_y $(y \leq 4)$ radicals take place. No $B_xN_yH_z$ and NH_z compounds within the plasma were detected by in-situ FTIR [42]. So, it was concluded that BH_y radicals have very high plasma-film surface reactivity with the ionized molecular nitrogen. This surface reactivity mainly accounts for the film growth process [42].

For films of this work deposited under similar conditions, but replacing ammonia with nitrogen as the source gas, increases the deposition rate (almost 3 times) and increases the BH/NH peak ratio of the corresponding infrared absorption bands.

The increase of the deposition rate (for nitrogen case) may be due to the disappearance of the BN radicals (which were present for ammonia case) inside the plasma. In the case of ammonia, part of the BH_y radicals are incorporated into the reactions within the plasma to create BN radicals, whereas only the rest can take place in the film growing process near the surface. Of course, created BN radicals also can contribute to the film growth, or/and they can create BN compounds that are pumped out from the chamber. So, the film deposition rate in the case of ammonia might be slower.

The decrease in NH FTIR absorption band for the case of nitrogen, as compared to that of ammonia, can be attributed to the small concentration of NH_z $(z \leq 2)$ radicals in the plasma and low hydrogen concentration coming only from diborane source. While *r* increases, NH absorption band becomes stronger. The large increase in BH absorption band in the films grown with the nitrogen source gas, as compared to ammonia, probably is due to the greater contribution of BH_y radicals to the film growth mechanism. The decrease of B_2H_6 flow rate leads to decrease in BH absorption band, which accounts for the decrease in the concentration of BH_y radicals within the plasma.

4.4.5 UV-visible measurements

Optical gap of the films is observed to increase with increasing nitrogen gas flow rate (Fig. 4.6). According to virtual crystal approximation, the band tail states in a disordered semiconductor result in a relatively smaller band gap energy compared with the optical gap of the perfect crystal structure at $0K$ [73], [74]. These tail states are responsible for the absorption of the electromagnetic radiation between the

energy levels above the valence band and below the conduction band. The density of tail states exponentially decreases as their energies get further away from the valence or conduction band edges (Eq. 1.16). Their depth within the forbidden gap is determined by the parameter called Urbach energy. Urbach energy is a measure of disorder in the semiconductor structure caused from the bond distortions which is the origin of tail states.

In the films studied in this Chapter, Urbach energy decreases from 0.45 to 0.22 eV as the N_2 flow rate is increased. High N_2 flows, without affecting substantially the atomic content, lead to a much more ordered structure. The evolution of the linear fits in Fig. 4.7 can be interpreted that the virtual crystal of the samples is unique, whose band gap energy is 5.92 eV. This energy gap of the virtual crystal is in good agreement with the direct band gap of 5.95 eV of the single crystal h-BN [75]. Therefore, increasing N_2 flow rate not only improves the order of the films but also leads to a configuration of atomic bonds which is closer to that of the virtual crystal.

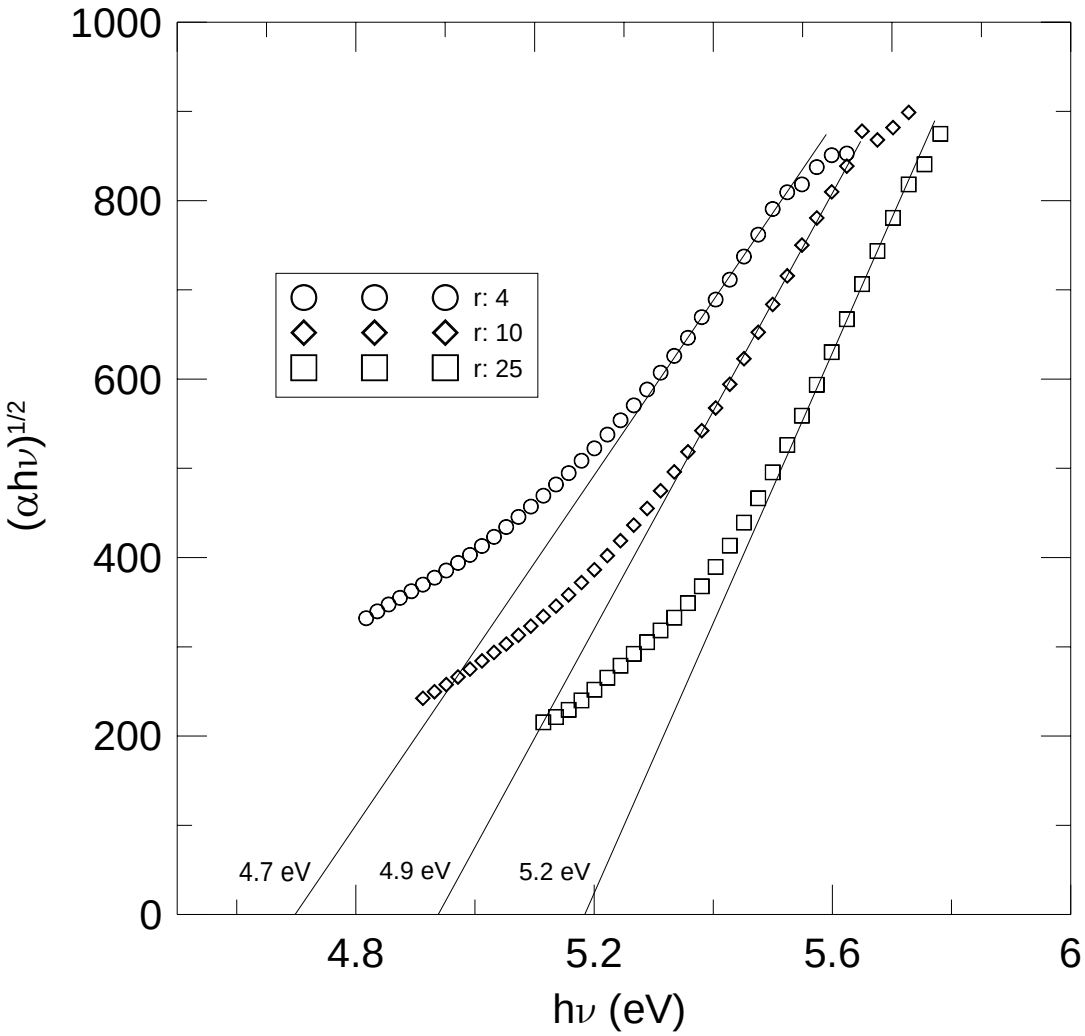

Figure 4.6: From the linear extrapolation of the $(\alpha h\nu)^{1/2}$ vs. $h\nu$ plotting (via. Eq. 1.15), the forbidden optical gap was obtained [This plotting corresponds to a band-to-band transition around the band edges for amorphous semiconductors]. The region of lower energies where the data deviates from straight line will be used to find Urbach energy, a disorder parameter.

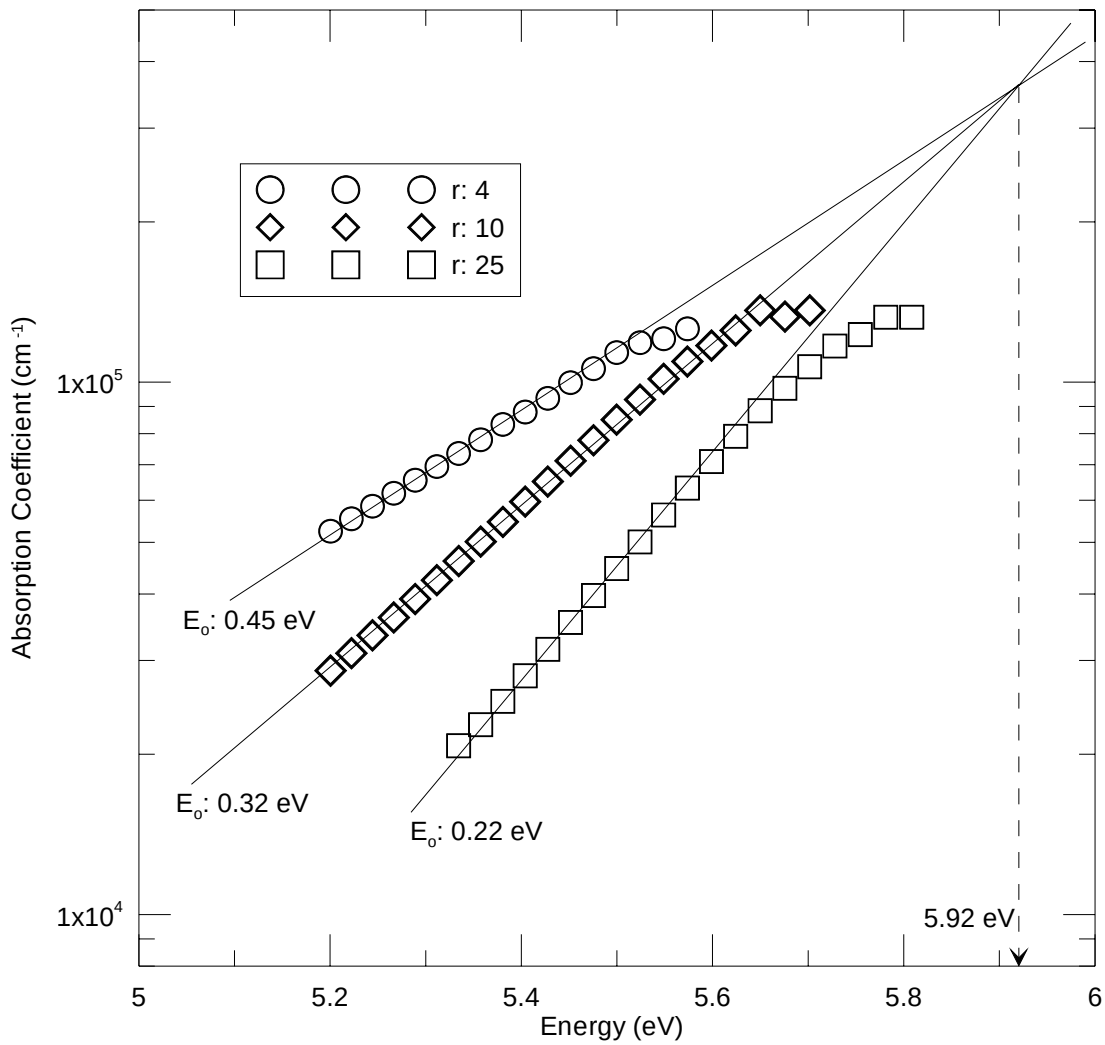

Figure 4.7: Plotting of $\ln(\alpha)$ vs. $h\nu$ where the inverse slope of the straight line fit gives out the Urbach energy. Urbach energy decreases as the nitrogen flow ratio increases. The behavior indicates that for a perfect virtual crystal, the data points will be perpendicular to the energy axis at 5.92 eV with $E_o = 0$.

4.4.6 Electrical Measurements

The microscopic structure of BN thin films, studied in this work seems to be heterogeneous as presented in Chapter 1. In other words, the $sp^2 - \sigma$ bonded hexagonal BN planar nanocrystallites of distributed sizes, more or less parallel to each other may be embedded within a disordered, boron rich, intermediate thin

phase. In this frame, the relatively ordered hexagonal "islands" of larger forbidden energy gap ($\geq 5\,\text{eV}$) are surrounded by an amorphous tissue of smaller gap ($\approx 3-4$ eV). Apparently, this short range ordered (randomly sp^2 and/or sp^3 bonded) defective matrix which may be boron rich, even contain particulates of boron phase, is more conductive than the dispersed hexagonal clusters. In this respect, the overall resistivity of the BN films should be determined by these resistive hexagonal clusters. However, this hypothesis is not confirmed by the spectral distribution of the optical absorption coefficient which has supplied an optical gap around 5 eV. This contradiction may be removed by the quantum size effect which might enlarge the smaller gap of the intermediate tissues towards or above that of the hexagonal clusters as depicted in the following diagram (Fig. 4.8). This relatively large energy gap value of about 5 eV places BN films among insulating materials, which allows the consideration of possible current transport mechanisms (described in details in Section 1.5). To estimate the resistivity of BN films at hand and investigate the current transport mechanisms, the electrical measurements are conducted with results that are presented in the following.

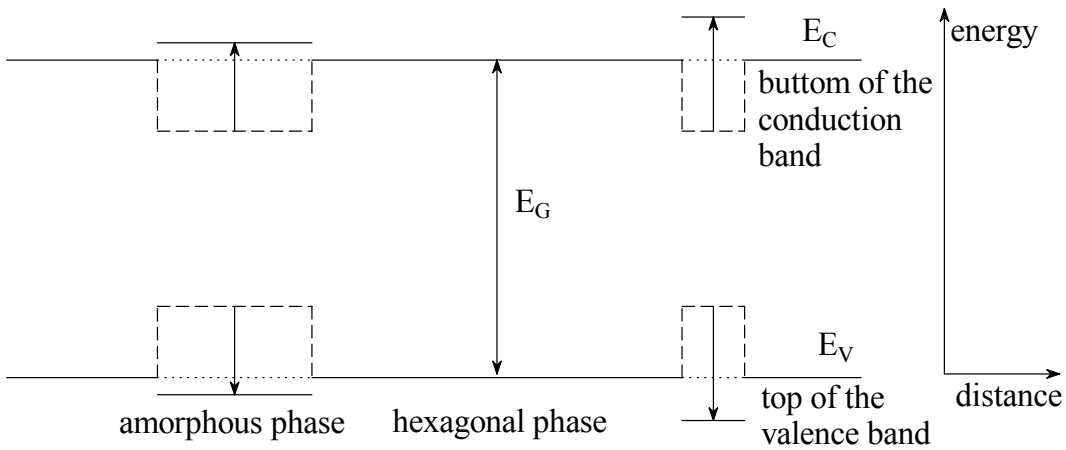

Figure 4.8: Energy band diagram of BN films, in which hexagonal clusters are surrounded by thin amorphous tissue. The small energy gap of the thin amorphous tissue is enlarged by the quantum size effect.

Electrical resistivities of the films are obtained along lateral and vertical directions by measuring current vs. voltage curves (*I-V*) by using aluminum-BN-aluminum (MIM) like devices as shown in Fig. 4.9.

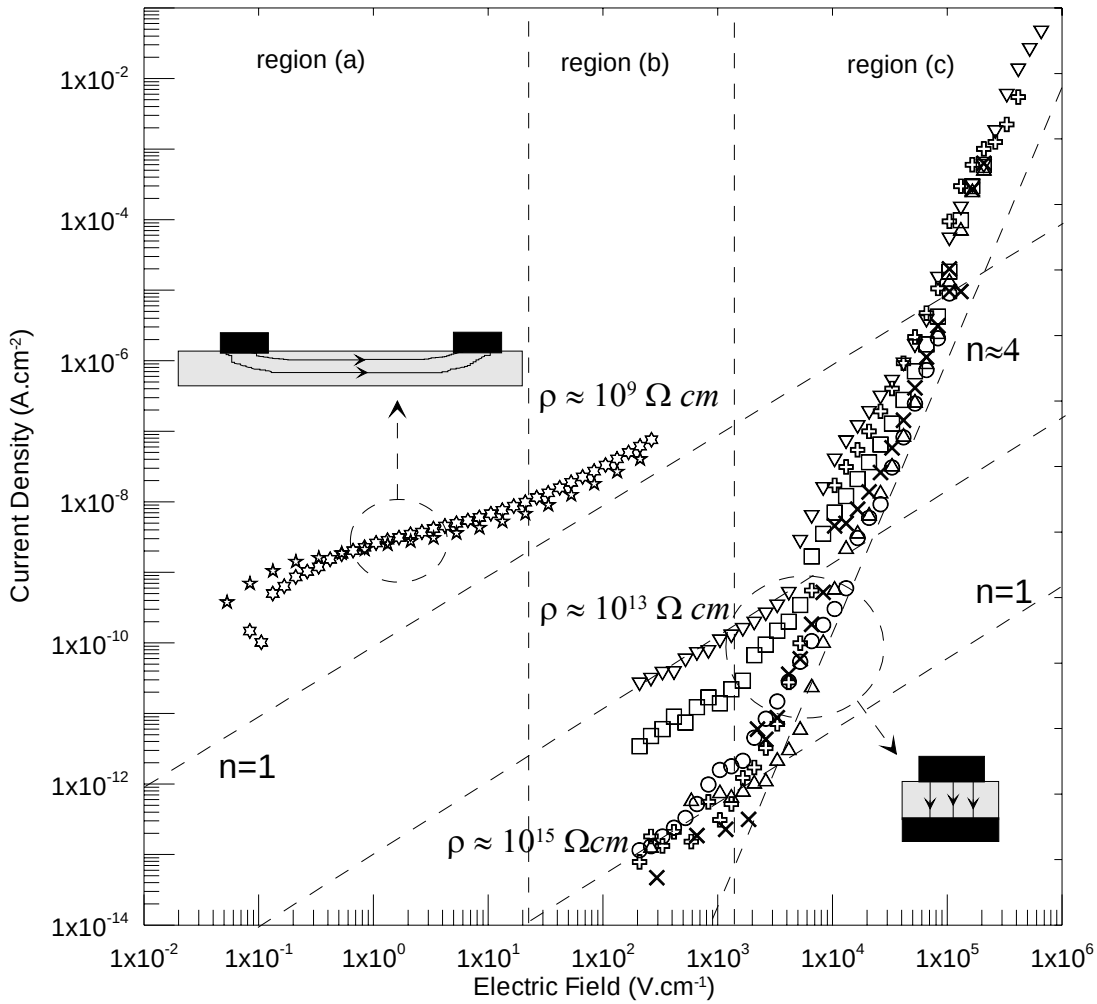

Figure 4.9: Lateral (upper group) and vertical (lower group) current-voltage (*I-V*) characteristics from BN2 sample where $I \propto V^n$ relation is considered. Region (a) low electric field $(n<1)$, region (b) ohmic region $(n=1)$, region (c) high electric field $(n>1)$.

Considering the discussion of Section 1.5, ohmic behavior in region (b) should not arise from transport of free carrier density p_0 of the insulator, since BN films at hand

are intrinsic and have wide band gap. Another possibility of ohmic behavior is expected in a defective material where a huge number of localized states is distributed across the forbidden gap. In this frame, *hopping conduction mechanism* becomes possible, that is, hopping (or tunneling) of carriers from one electrode to the opposite one through neighboring localized states (without jumping to the relevant band leads to ohmic current-voltage relation [76] (Fig. 1.18, mechanism "4"). This last ohmic mechanism seems to exist in BN thin films at hand for low voltage values (region (b)).

For vertical resistivity measurements there is also region (c) for high electric field. The space-charge-limited carrier transport mechanism b.2. of Section 1.5 indicates the constant *a* of Eq. 1.40 to be equal to 3, since current is proportional to the fourth power of the voltage (Fig. 4.9).

In the case of lateral resistivity measurements there is low electric field region (Fig. 4.9), where the current has slight voltage dependence. This can be attributed to the thermionic (Schottky) emission at the BN film and metal interface.

In the frame of this work, the ohmic region (region (b) of Fig. 4.9) was taken into account in order to estimate the resistivity properties of BN films. The lateral resistivity (of about $10^9 \Omega.cm$) is drastically (4-6 decades) lower than vertical resistivity (within the interval $10^{13} - 10^{15} \Omega.cm$) (Fig. 4.9). It points out a serious anisotropy in the electrical conductivity of the BN films at hand. This electrical anisotropy might be due to the heterogeneous structure of the films, which is speculated in the following. During the film growth, existence of a thin amorphous layer at the film-substrate interface seems possible (See Chapter 1). This highly disordered layer should contain several traps within the forbidden gap. As BN is very resistive electrically, electron transport through the traps (instead of through conduction band) might be rather more probable. Then, the equivalent lateral resistance of the film is measured to be relatively lower because the effective part of the current passes through the amorphous layer. This thin amorphous layer should not be that much effective when the voltage is applied vertically (most of the voltage

drop should occur before reaching the amorphous layer). In this respect, the equivalent resistance becomes relatively higher. Moreover, BN film might be composed of hexagonal (graphitic) planes dominantly oriented parallel to the substrate, which is consistent with the FTIR results. Such orientation of the planes may also contribute to the serious difference between lateral and vertical resistivities. To conclude, the amorphous layer model together with the preferred orientation of the hexagonal planes seems to be the underlying factor of the anisotropy in electrical resistivity.

Fig. 4.10 exhibits the lateral resistivity, optical gap and refractive index alterations with increasing *r*. As discussed above, increasing *r* from 4 to 25 decreased the density of tail states and increased the optical gap. The decrease in tail state density, which should reduce the total volume of the amorphous tissue, indicates the formation of more ordered films. Hence, increase in lateral resistivity with *r* may result from the reduction of the volume of amorphous tissue throughout the film structure. In addition, reduction of amorphous layer width through which most of the current passes seems to be another possible reason for the increase in lateral resistivity. However, stress measurements imply no significant changes at the interface; thus, second possibility seems to be less probable.

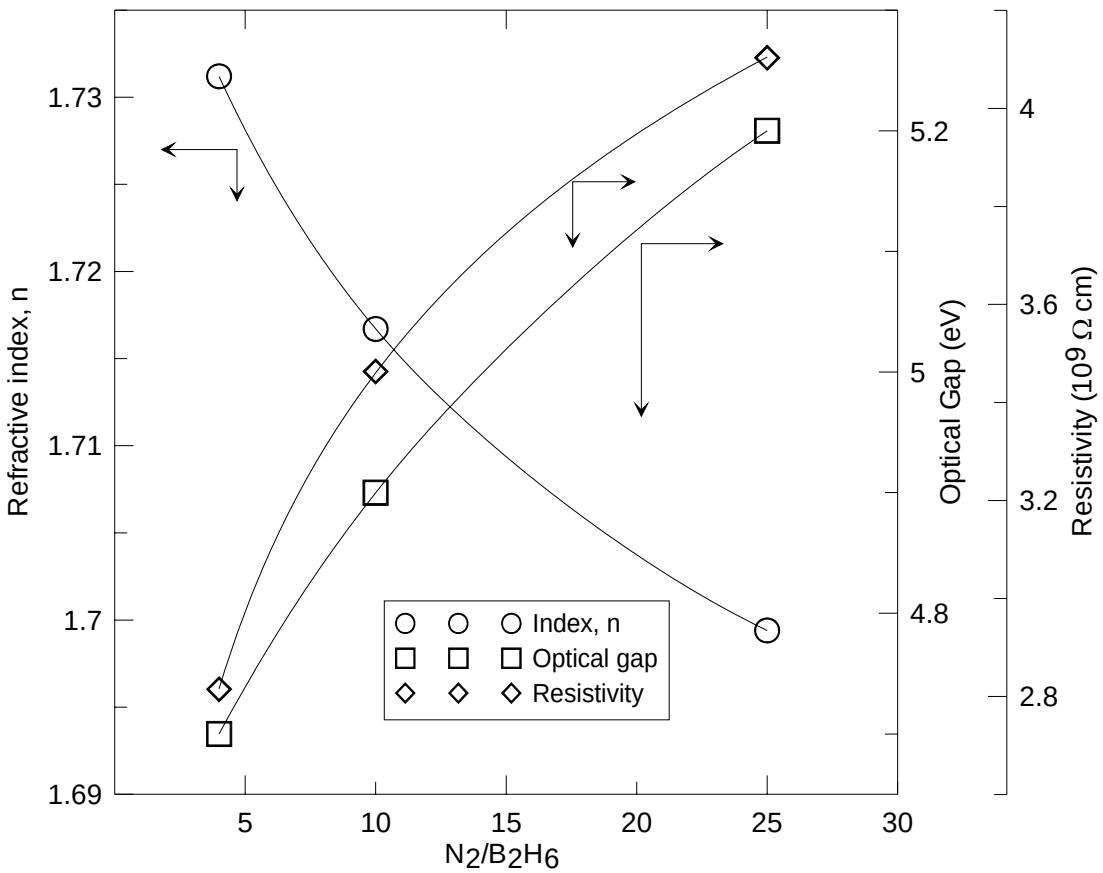

Figure 4.10: The changes in optical gap, refractive index and resistivity of BN films with increasing N_2/B_2H_6 flow ratio.

4.5 Summary

Boron nitride thin films are produced in a PECVD reactor using N_2 and B_2H_6 as the source gases. The three deposition sets include different relative flow rates of nitrogen gas: r = 4, 10 and 25.

Oxygen is homogeneously distributed throughout the film structure since no significant oxygen content difference between the surface and the bulk of the film was recognized via XPS measurements. Oxygen existence might be caused from either a leakage in the reactor or a sudden diffusion subsequent to the deposition. No infrared spectra difference is observed 80 days after the deposition, which eliminates the idea of slow oxygen diffusion from atmosphere and shows that films are stable

under humid atmosphere. Oxygen seems to be the main factor preventing to reach stoichiometric films since B-O bonds cannot be avoided. Boron centered ternary BN_yO_x structure should be effective since (N+O)/B ratio is close to stoichiometry [67]. This ratio is always slightly smaller than unity owing to the oxygen atoms bonded also to nitrogen. The effect of N_2 flow on the B/N ratio is almost negligible if the weak tendency of reaching unity is disregarded. However, an internal variation in bond configurations is observed without an intense effect on atomic concentrations. The nitrogen atom incorporation in the ternary BN_yO_x structure decreases and $B\text{-}N_3$ formation is promoted as the relative nitrogen gas flow increases.

FTIR analysis suggests that h-BN cluster size (distributed parallel to the substrate surface with some planes at the edges of the clusters oriented randomly) is increased with *r*. The decrease of total hydrogen atom density can be a result of reduction in dangling bond concentration, thus indicating the increase of cluster sizes and improvement of the film order.

The evolution of $\ln\alpha$ vs. *E* graphs for different samples showed that the films have the same virtual crystal of band gap 5.92 eV. In this respect, increase in relative N_2 flow seems to act as a catalyst of B-N bond formation in a less distorted environment.

The internal stresses of the films are almost constant, which indicates similar atomic bonds at the interface of the film/substrate composite. Thus, amorphous layer at the interface is not affected by increasing N_2/B_2H_6 flow ratio.

Besides, films seem to be anisotropic since the vertical resistivity is always drastically greater than the lateral one. In addition, the increase in lateral resistivity with increasing *r* might arise from the reduction of the volume of amorphous tissue in the bulk of the films, as suggested by decreasing Urbach energy.

CHAPTER 5

CONCLUSIONS

Boron and nitrogen are two nearest neighbors of carbon in the periodic table of elements. Therefore, boron nitride (BN) is isoelectronic with carbon. As carbon has allotropes as diamond and graphite, BN also has cubic and hexagonal phases analogically. Hexagonal boron nitride (h-BN) is the only stable form of BN in nature and cubic boron nitride (c-BN) can be produced by extensive heat or pressure treatments of the hexagonal phase.

h-BN is composed of planes of hexagonal rings with ABAB… stacking sequence (Chapter 1). In these hexagonal rings the p_z orbitals of both boron and nitrogen remain unbound and share two electrons. These electrons are not, however, shared equally between boron and nitrogen. Relatively more electronegative nitrogen mostly attracts these electrons. Hence, electrons become more or less localized in the p_z orbital of nitrogen $(p_z)_N$ leaving that of boron, $(p_z)_B$ unoccupied. In contrast to graphite being a conductor where the p_z electron wave functions are extended, h-BN is an insulator as p_z electrons are mostly localized around nitrogen atom. Tight binding calculations for band structure of h-BN revealed that the valence band maximum and conduction band minimum consist of mostly $(p_z)_N$ and $(p_z)_B$ orbitals, respectively.

The polar nature of the bonds between B and N should contribute to widening of the band gap. Being a wide band gap semiconductor h-BN expectedly exhibits negative electron affinity (NEA). This property has promising applications such as

photodetectors and cold-cathode emitters. Old era NEA devices (NEADs) highly suffered from easy contamination. On the other hand, h-BN, whose NEA was first observed in 1995, is a very inert material. Chemical inertness of h-BN is the main advantage of h-BN NEAD applications. Importance of hydrogen surface termination on NEA of h-BN should not be overlooked. Hydrogen removal from NEA h-BN results in positive electron affinity (PEA), where as hydrogen treatment of PEA surface regenerates NEA. However, the main objective of hydrogen on the h-BN surface is still in debate. One possible speculation might be that the bond energy of N-H is relatively lower than that of B-H, which means that N-H bond formation is easier. The surface of a pure h-BN crystal is neutral. In this respect, hydrogen termination should result in that the surface is mostly composed of hydrogen and boron, and then a positively charged layer is formed as the majority of H being bound to N. A charged surface layer should cause a suitable energy band bending pulling the vacuum level below the conduction band minimum.

Optical absorption coefficient is obtained by integration over all density of states near the parabolic band edges. As the density of states below the band edges is exponentially decreasing function of energy, absorption coefficient at this energy range should be proportional to the exponential of energy. This energy range corresponds to medium absorption region where tail-to-band transitions occur. The depth of the tail states into the forbidden gap is determined by Urbach energy. The films studied in this work exhibited Urbach energies of 0.2-0.5 eV, which means that the films are very defective. Thus, the optical absorption coefficient for amorphous materials is used for band gap calculations. Band gap of the films varies in the range 4.9-5.4 eV and the refractive index is found to be around 1.7 and hence the films are transparent to visible light and opaque in the ultraviolet region.

In the frame of this thesis, a mechanical stylus profilometer is installed in the laboratory and used for surface profile analysis of the samples (Chapter 2). The system allows the user to determine the thicknesses and internal stresses quite precisely. The main advantage of the device compared with optical thickness determination is that thickness profile is directly loaded to a screen. In optical

measurements, several calculations are necessary to decompose the optical path into thickness and refractive index. In addition, the software of the profilometer for stress calculation has been compared with a manual calculation on the same data. Both calculations give more or less the same stress. In this respect, experimenter is free to use any of the methods (i.e. if the curvature of the substrate surface is not smooth, manual calculation would be suitable).

FTIR and XPS are useful techniques for the observation of the film structure. For the calculation of atomic densities from FTIR spectra, the absolute response of the corresponding bond to IR (the effective charge of the bond determines its response) should be well known. Effective charges of B-H and N-H are found from the works on hydrogenated amorphous boron (a-B:H) and hydrogenated amorphous silicon nitride (a-$Si_{1-x}N_x$:H) films, respectively. Besides, BN film phase change is easily followed by FTIR. As for the XPS analysis, relative comparison of each bond concentration is possible. This method is mainly used to determine atomic concentrations of constituent elements in each sample.

Heat treatment is applied on the samples deposited with ammonia and diborane as source gases (Chapter 3). Three samples are heated up to 475, 650 and 800 ^{0}C, while one sample is kept as reference. The as-deposited film contains the largest amount of hydrogen. Hydrogen atom density gradually decreased with increasing the annealing temperature. In amorphous materials hydrogen is known to reduce the coordination defect and relax the system. The dangling bonds created as a result of intensive bond length and angle distortions are easily saturated by hydrogen and then hydrogen decreases the average coordination number of the system. As the hydrogen escapes from the sample structure with heat treatment, the relaxation of the system is reduced and the band distortions should increase. In this respect, the films are expected to become more disordered. This expectation is verified by the increase in Urbach energy and thin film stress. Film stress mainly arises from the possible lattice mismatch of the film-substrate composite. Such a mismatch should result in bent and stretched bonds at the interface. Consequently, some bonds might be broken to relax the system. In the presence of sufficient hydrogen the interface bonds might be

relaxed and then internal stress is reduced. Hydrogen escape from the system should cause the opposite, which was observed in Chapter 3.

Changing the nitrogen flow rate in the nitrogen-diborane source gas is shown to affect the physical properties of the films (Chapter 4). The change in nitrogen flow rate, however, does not affect the atomic concentrations intensively. On the contrary, bond densities of the compounds within the films are altered. The films of lowest nitrogen gas (N_2) flow rate contain the most B-B bonds. Increasing the N_2 flow rate results in the breakage of B-B bonds and the usage of resultant boron atoms in the formation of B-N and ternary $B\text{-}O_xN_y$ structures. In contrast, nitrogen corporation in the ternary structure is reduced such that nitrogen is mostly used for B-N or N-H formation. Linear fits of logarithm of absorption coefficient versus energy graph for r = 4, 10 and 25 intersect at the same energy of 5.92 eV, which corresponds to the gap of their virtual crystal. The increase in r somehow causes h-BN cluster size to increase and then more ordered films result, without changing their virtual crystal: Urbach energies decrease with increasing N_2 flow rate. The stress of these films does not change which implies the highly disordered layer neighboring the substrate is not that much affected from an increase in nitrogen flow rate. The resistivity measurements taken in both vertical and lateral directions indicate the anisotropy in the film structure.

REFERENCES

[1] Pritchard H.O., Skinner H.A., Chem. Rev., 55, 1955, 745-786.

[2] Muetterties E.L., "The chemistry of Boron and its compounds", John Wiley and Sons Inc., London, 1967.

[3] Bello I., Chong Y.M., Leung K.M., Chan C.Y., Ma K.L., Zhang W.J., Lee S.T., Layyous A., Diamond and Related Materials, 14, 2005, 1784 – 1790.

[4] Ronning C., Dreher E., Felderrnann H., Gross M., Sebastian M., Hofsass H., Diamond and Related Materials, 6 (1997), 1129-1134.

[5] Robertson J., Phys. Rev. B, 29, no:4 (1984), 2131.

[6] Hoffmann, D.M., Doll, G.L., Ekiund, P.C., Phys. Rev. B, 30, no:10 (1984), 6051-6056.

[7] Akaoglu B., Ph.D. Thesis, Optical Properties of Silicon Based Amorphous Thin Films, METU, 2004.

[8] Freund, L. B., Suresh S., Thin film materials: stress, defect formation, and surface evolution**,** Cambridge, [England]; New York: Cambridge University Press, 2003.

[9] Santes E.J.P., MacDonald N.C., IEEE IEDM, 92 (1992), 743-746.

[10] Bell R.L., Negative Electron Affinity Devices, 1972.

[11] Powers M. J., Benjamin M. C., Porter L. M., Nemanich R. J., Davis R. F., Cuomo J. J., Doll G. L., Harris S. J., Appl. Phys. Lett., 67 (26), 1995, 3912-3914.

[12] Loh K.P., Sakaguchi I., Nishitani-Gamo M., Tagawa S., Sugino T., Ando T., Appl. Phys. Lett., 74 (1), 1999, 28-30.

[13] Scheer J.J., van Laar J., Sol. State Com., vol.3, 1965, pp.189-193.

[14] Sommer A.H., J. Appl. Phys., 42 (1971), 2158.

[15] Taylor J.B., Langmuir I., Phys. Rev., vol.44 (1933), pp.437.

[16] Ishida H., Phys Rev. B, 39 (8), 1989, 5492-5495.

[17] Ning W., Kailai C., Dingsheng W., Phys. Rev. Lett., 56 (25), 1986, 2759-2792.

[18] Himpsel F.J., Knaap J.A., VanVechten J.A., Eastman D.E. Phys. Rev. B, 20 (2), 1979, 624-627.

[19] Loh K. P., Gamo-Nishitani M., Sakaguchi I., Taniguchi T., Ando T., Appl. Phys. Lett., 72 (23), 1998, 3023-3025.

[20] Li W., Gu G., Li Y., He Z., Liu L., Zhao C., Zhao Y., Appl. Surf. Sci., 242 (2005), 207-211.

[21] Sze S.M., Physics of Semiconductor Devices, New York: Wiley, c1981.

[22] Lampert M.A., Current Injection in Solids, Academic press, New York, 1970.

[23] The manual can be obtained from the website of the producer company: http://www.ambiostech.com (last accessed date: 10 July 2007).

[24] Swanepoel R., J. Phys. E: Sci. Instrum., 16, 1983, 1214-1222.

[25] Postole G., Caldararu M., Ionescu N.I., Bonnetot B., Auroux A., Guimon C., Thermochimica Acta, 434, 2005, pp. 150–157.

[26] Nose K., Oba H., Yoshida T., Appl. Phys. Lett., 89 (2006), 112124.

[27] Dubrovinskaia N., Solozhenko V.L., Miyajima N., Dmitriev V., Kurakevych O. O., Dubrovinsky L., Appl. Phys. Lett., 90, 2007, 101912.

[28] Aleixandre C.G., Essafti A., Fernandez M., Fierro J.L.G., Albella J.M., J. Phys. Chem. 1996, 100, 2148-2153.

[29] Alkoy S., Toy C., Turgay G., Tekin A., Jour. Euro. Cer. Soc., 17, 1997, 1415-1427.

[30] Watanabe K., Taniguchi T., Kanda H., Nature Materials, Vol.3, 2004, 404-409.

[31] Mohammad S.N., Sol.-State Electronics, 46, 2002, 203-222.

[32] Miyamoto H., Hirose M., Osaka Y., Jap. Jour. Appl. Phys., 22, 1983, L216-L218.

[33] Schomalla W., Hartnagel H.L., Jour. Electrochem. Soc., 129 (11), 1982, 2636-2637.

[34] Rand M.J., Roberts J.F., Jour. Electrochem. Soc., 115 (4), 1968, 423-429.

[35] Yamaguchi E., Minakata M., J. Appl. Phys., 55 (8), 1984, 3098-3102.

[36] Battiston G.A., Berto D., Convertino A., Emiliani D., Figueras A., Gerbasi R., Viticoli S., Electrochimica Acta, 50, 2005, 4600-4604.

[37] Mirkarimi P.B., McCarty K.F. and Medlin D.L., Mater. Sci. Eng., R21, 1997, 47-100.

[38] Kessler G., Bauer K.D., Pompe W., and Scheibe J.J., Thin Solid Films, 147, 1987, L45-L50.

[39] Yang T.-S., Tsai T.-H., Lee C.-H., Cheng C.-L. and Wong M.-S., Thin Solid Films, 398-399, 2001, 285-290.

[40] Rodríguez M., Kharissova O.V., Ortiz U., Rev.Adv.Mater. Sci., 7, 2004, 55-60.

[41] Thevenin P., Eliaoui M., Ahaitouf A., Soltani A., Bath A., Surf. & Coat. Technol., 200 (22-23), 2006, 6444-6448.

[42] Franz D., Hollenstein M. and Hollenstein C., Thin Solid Films, 379, 2000, 37-44.

[43] Sigaev V.N., Pernice P., Aronne A., Fanelli E., Lotarev S.V., Orlova E.V., Califano V., Champagnon B. and Vouagner D., J. Non-Cryst. Solids, 352**,** 2006, 2123.

[44] Su S., J. Molecular Structure: Theochem., 430, 1998, 137.

[45] Godet C., Schmirgeld L., Zuppiroli L., Sardin G., Gujrathi S., and Oxoron K., J. Mater. Sci., 26, 1991, 6408.

[46] Thompson P., Parsons I., Graham C. M., Jackson B., Contrib. Mineral Petrol, 130, 1998, 176-186.

[47] Soltani A., Thevenin P., Bath A., Mater. Sci. and Eng., B82, 2001, 170-172.

[48] Akkerman Z.L., Kosinova M.L., Fainer N.I., Rumjantsev Y.M. and Ysoeva N.P., Thin Solid Films, 260, 1995, 156-160.

[49] Shimizu T., Yoneyama T. and Sato S., CLEO Pacific RIM, Paper CFE2-3, Tokyo, 2005.

[50] Eyhusen S., PhD thesis, Phase formation processes in the synthesis of boron nitride thin films, Georg-August-University, 2005.

[51] Huang P.-C., Yang T.-S., Chu S.-S. and Wong M.-S., Thin solid films, 515, 2006, 973-978.

[52] Park Y. B. and Rhee S. W., J. Mater. Sci.: Mater. Electron., 12, 2001, 515.

[53] Adams A.C., Capio C.D., J. Electrochem. Soc., 127-2, 1980, 399-405.

[54] Coscia U., Ambrosone G., Lettiery S., Maddalena P., Rava P., Minarini C., Thin Sol. Films, 427, 2003, 284-288.

[55] Sobbia R., Sansonnens L., Bondkowski J., J. Vac. Sci. Technol., A 23 (4), 2005, 927-932.

[56] Akaoglu B., Gulses A., Atilgan I., Katircioglu B., Vacuum, 81 (1), 2006, 120-125.

[57] Tikhonravov A.V., Trubetskov M.K., OptiChar ©, http://www.optilayer.com (last accessed date: 10 July 2007), V 4.12, 2002.

[58] Sansonnens L., J. Appl. Phys., 97, 2005, 0633304 1-6.

[59] Howling A.A., Derendinger L., Sansonnens L., Shmidt H., Hollenstein Ch., Sakanaka E., Shmitt J.P.M., J. Appl. Phys., 97, 2005, 123308 1-13.

[60] Dollet A., Couderc J.P., Despax B., Plasma Sources. Sci. Technol., 4, 1995, 94.

[61] Kapoor V.I., Skebe G.G., Mat. Sci. Forum., Vols. 54&55, 1990, pp.353-374.

[62] Kondratiev V.N., Bond Dissociation Energies, Ionization Potentials, and Electron Affinities, Nauka, Moscow, 1974.

[63] Dietrich D., Stockel S., Marx G., Fresenius J. Anal. Chem., 361 (1998), 653-655.

[64] Goto T., Hirai T., J. Mat. Sci., 7, 1988, 548.

[65] Rivierie J.P., Pacaud Y., Cahoreau M., Thin Solid Films, 227 (1993), 44-53.

[66] Tsai P-C., Surf. & Coat. Technol., 201 (2007), 5108-5113.

[67] Guimon C., Gonbeau D., Pfister-Guillouzo G., Dugne O., Guete A., Naslain R., Lahaye M., Surf. Int. Anal., Vol. 16, 1990, pp. 440-445.

[68] Vincent H., Chassagneux F., Vincent C., Bonnetot B., Berthet M.P., Vuillermoz A., Bouix J., Mat. Sci. Eng., A340 (2003), 181-192.

[69] Sugino T., Tagawa S., Appl. Phys. Lett., 74 (1999), 889-891.

[70] Benko E., Barr T.L., Hardcastle S., Hoppe E., Bernasik A., Morgiel J., Ceramics International, 27 (2001), 637-643.

[71] Wagner C.D., Riggs W.M., Davis L.E., Moalder J.F., Muilenberg G.E., Handbook of X-Ray Photoelectron Spectroscopy, Perkin Elmer, Physical Electronics Division, Eden Prairie, MN, 1979.

[72] Matloob M.H., Roberts M.W., Phys. Scripta, Vol. 16, 1977, 420-424.

[73] Heil R.B., Aita C.R., J. Vac. Sci. Technol. A 15(1), 1997, 93-98.

[74] Cody G. D., in Hydrogenated Amorphous Silicon: Optical Properties, edited by J. I. Pankove, Academic, Orlando, FL, 1984, Vol. 21, Part B, pp. 25–42.

[75] Remes Z., Nesladek M., Haenen K., Watanabe K., Taniguchi T., Phys. Stat. Sol., A202, 2005, 2229-2233.

[76] Mott N.F., Davis E.A., Electronic Processes in Non-Crystalline Materials, Clar. press, Oxford, 1979.

[77] Landau L.D., Lifshitz E.M., Theory of Elasticity, Pergamon Press, 1959

APPENDIX A

OPTICAL ABSORPTION

A.1 Time Dependent Perturbation Theory

If the initial state of a time evolving system is initially $\left|\psi\left(t=0\right)\right\rangle_{in} = \sum c_n \left|n\right\rangle$, its final state at time t is found by the time-dependent Schrödinger equation:

$$\begin{aligned} & i\hbar \frac{\partial}{\partial t}\left|\psi\left(t\right)\right\rangle = H_0 \left|\psi\left(t\right)\right\rangle \\ & \Rightarrow \\ & \left|\psi\left(t\right)\right\rangle = \sum c_n e^{-i\frac{E_n}{\hbar}t} \left|n\right\rangle \end{aligned} \tag{A.1}$$

Here, $\left|n\right\rangle$ denotes the eigenstate of Hamiltonian H_0. When the Hamiltonian is time dependent, as it is in the case of exposure to electromagnetic radiation, c_n should also be time dependent. Thus, in the presence of W, when the Hamiltonian is $H_0 + W$, the state becomes,

$$\left|\psi\left(t\right)\right\rangle = \sum c_n\left(t\right) e^{-i\frac{E_n}{\hbar}t} \left|n\right\rangle \tag{A.2}$$

Thus, the probability of finding the system in a state $\left|n\right\rangle$ at time t is found by projecting that state onto $\left|n\right\rangle$:

$$\left\langle n\middle|\psi\left(t\right)\right\rangle = \sum c_m\left(t\right) e^{-i\frac{E_m}{\hbar}t} \left\langle n\middle|m\right\rangle \tag{A.3}$$

Since $\langle n|m\rangle = \delta_{nm}$, the probability is given by

$$\left|c_n(t)\right|^2 = \left|\langle n|\psi(t)\rangle\right|^2 \tag{A.4}$$

The weight functions $c_n(t)$ can be determined by the consideration of time dependent Schrödinger equation for the case of electromagnetic perturbation, W:

$$\begin{aligned}
\left\langle n\left|i\hbar\frac{\partial}{\partial t}\psi(t)\right.\right\rangle &= \langle n|H\psi(t)\rangle \\
e^{-\frac{i}{\hbar}E_n t}\cdot i\hbar\frac{\partial}{\partial t}c_n(t) &= \sum_m \langle n|W|m\rangle\langle m|\psi(t)\rangle \\
\frac{\partial}{\partial t}c_n(t) &= -\frac{i}{\hbar}\sum_m e^{\frac{i}{\hbar}(E_n-E_m)t}W_{nm}(t)c_m(t)
\end{aligned} \tag{A.5}$$

A.2 Dyson Series to Obtain Transition Probability

Exact solutions to the above differential equation (A.5) are usually not available especially for problems of more than two dimensions. Therefore, an approximate way should be followed to reach the weight functions $c_n(t)$, whose absolute square gives the transition probability. If $c_n(t)$ is expanded into power series,

$$c_n(t) = c_n^{(0)}(t) + c_n^{(1)}(t) + c_n^{(2)}(t) + \ldots \tag{A.6}$$

is obtained. These components of weight function $c_n(t)$ can be easily obtained by the introduction of time development unitary operator here:

$$\begin{aligned}
U(t+dt,t) &= I - \frac{i}{\hbar}Hdt \\
U(t+dt,t_0) &= U(t+dt,t)U(t,t_0) \\
&= U(t,t_0) - \frac{i}{\hbar}HU(t,t_0)dt
\end{aligned} \tag{A.7}$$

Since dt is an infinitesimal time element Eq. A.7 can be reduced to the form:

$$i\hbar\frac{\partial}{\partial t}U\left(t,t_0\right)=HU\left(t,t_0\right) \tag{A.8}$$

If the Hamiltonian is time dependent the integration to obtain the time development operator is of the form:

$$U\left(t,t_0\right)=I-\frac{i}{\hbar}\int_{t_0}^{t}dt^{'}H\left(t^{'}\right)U\left(t^{'},t_0\right) \tag{A.9}$$

At this step, Dyson-Wick iteration procedure may be applied (Here, Interaction picture, where $\hat{U}(t,t_o)=U_o^{\dagger}(t)U(t,t_o)U_o(t)$ with $U_o=e^{-\frac{i}{\hbar}H_o(t-t_o)}$,is used):

- Zeroth order approximation:

$\hat{U}^{(0)}\left(t,t_0\right)=I$ (dropping $\int$ term)

- First order approximation:

$$\begin{aligned}\hat{U}^{(1)}\left(t,t_0\right)&=I-\frac{i}{\hbar}\int_{t_0}^{t}dt^{'}H\left(t^{'}\right)\hat{U}^{(0)}\left(t^{'},t_0\right)\\&=I-\frac{i}{\hbar}\int_{t_0}^{t}dt^{'}H\left(t^{'}\right)\end{aligned} \tag{A.10}$$

- Second order approximation:

$$\begin{aligned}\hat{U}^{(2)}\left(t,t_0\right)&=I-\frac{i}{\hbar}\int_{t_0}^{t}dt^{'}H\left(t^{'}\right)\hat{U}^{(1)}\left(t^{'},t_0\right)\\&=I-\frac{i}{\hbar}\int_{t_0}^{t}dt^{'}H\left(t^{'}\right)+\left(\frac{i}{\hbar}\right)^2\int_{t_0}^{t}dt^{'}\int_{t_0}^{t^{'}}dt^{''}H\left(t^{'}\right)H\left(t^{''}\right)\end{aligned}$$

As the time development operator is obtained, a state ket $\left|\psi\left(t\right)\right\rangle$ can be expressed in terms of a state of an earlier time $\left|i\right\rangle$:

$$\left|\psi\left(t\right)\right\rangle=U\left(t,t_0\right)\left|i\right\rangle \tag{A.11}$$

The transition weight function $c_n(t)$ can be obtained by the bra-ket operation:

$$c_n(t) = \langle n | \hat{U}(t, t_0) | i \rangle \tag{A.12}$$

Equation Eq. A.10 of Dyson series and expansion of weight function in Eq. A.12 give out the following results for weight functions up to first order approximation:

- $c_n^{(0)} = \langle n | I | i \rangle = \delta_{in}$ (independent of time)
- $c_n^{(1)}(t) = -\frac{i}{\hbar} \int_0^t dt' e^{\frac{i}{\hbar}(E_n - E_i)t} \langle n | W | i \rangle$ (A.13)

For a transition from an initial state to a different final state, zeroth order time independent term vanishes. Thus, the transition probability from state $|i\rangle$ to state $|n\rangle$ under the action of perturbation W is given by

$$\left| c_n^{(1)} \right|^2 = \frac{1}{\hbar^2} \left| \int_0^t \langle n | W | i \rangle e^{\frac{i}{\hbar}(E_n - E_i)t} dt' \right|^2 \tag{A.14}$$

and the transition rate is defined by the transition probability per unit time:

$$M_{in} = \frac{d}{dt} \left| c_n^{(1)}(t) \right|^2 \tag{A.15}$$

A.3 Absorption Process

A vector potential $\vec{A}$ (along the direction of the unit vector $\hat{\varepsilon}$) of a monochromatic plane wave of angular frequency ω, amplitude A_0 can be represented by

$$\vec{A} = A_0 e^{i\frac{\omega}{c}\hat{n}.\vec{x} - i\omega t} \hat{\varepsilon} \tag{A.16}$$

then, the perturbation operator can be written as

$$W = \left[-\frac{e}{mc} A_0 e^{i\frac{\omega}{c}\hat{n}.\vec{x}} \left(\hat{\varepsilon}.\vec{p} \right) \right] e^{-i\omega t} \tag{A.17}$$

Using equations (A.14), (A.15) and (A.17), the transition probability at time t is

$$\left| c_n^{(1)} \right|^2 = \frac{1}{\hbar^2} \left| \upsilon_{in} \right|^2 \frac{\sin\left(\frac{E_n - E_i}{\hbar} - \omega \right) t}{\left(\frac{E_n - E_i}{\hbar} - \omega \right)} \tag{A.18}$$

from which the rate can be obtained. Here, $\upsilon_{in} = -\langle n | \frac{eA_0}{mc} e^{i\frac{\omega}{c}\hat{n}.\vec{x}} \left(\hat{\varepsilon}.\vec{p} \right) | i \rangle$. (A.19)

As $t \to \infty$, expression A.18 approaches to Dirac δ-function which grows proportional to t. As a result, the transition rate becomes,

$$M_{in} = \frac{2\pi}{\hbar} \frac{e^2 A_0^2}{m^2 c^2} \left| \upsilon_{in} \right|^2 \delta\left(E_n - E_i - \hbar\omega \right) \tag{A.20}$$

Therefore, transition is possible when the absorbed energy is equal to the energy difference between the final and the initial states.

Furthermore, equation for υ_{in} in (A.19) gives a non-zero result only if $\vec{k}_n = \vec{k}_i$ (where k_n and k_i are crystal momenta of electron in states $|n\rangle$ and $|\mathrm{i}\rangle$, respectively) assuming that the momentum of the photon h/λ is much smaller than the crystal momentum h/a, where a is a few angstroms. Thus, the equality of initial and final momenta of the electron should also be included in (A.20):

$$M_{in} = \frac{2\pi}{\hbar} \frac{e^2 A_0^2}{m^2 c^2} \left| \upsilon_{in} \right|^2 \delta\left(E_n - E_i - \hbar\omega \right) \delta_{k_i k_n} \tag{A.21}$$

A.4 Optical absorption coefficient, $\alpha(\hbar\omega)$

Absorption coefficient is a measure of the amount of energy absorbed by a particle per unit length. It is proportional to the absorption probability of unit flux by a single center, σ, to the density of these centers, dn_i, and to the density of available states for the electron after transition, dn_f, such that;

$$\alpha = \iint \sigma dn_i dn_f \tag{A.22}$$

Flux of radiation is defined by the intensity per photon energy. Intensity can be expressed by the average electromagnetic energy per unit area per unit time which is $\varepsilon \upsilon E_0^2 / 8\pi$. Converting the electric field amplitude to the amplitude of vector potential by $E_0 = (\omega/c) A_0$, flux can be written as:

$$F = \frac{\varepsilon A_0^2 \omega}{8\pi n c \hbar} \tag{A.23}$$

after which the absorption probability of unit flux (effective cross section for absorption) is obtained with absorption probability rate of (A.21):

$$\sigma = \frac{M_{if}}{F} = \frac{8\pi n c \hbar}{\varepsilon \omega A_0^2} M_{if} \tag{A.24}$$

Density of states calculation will be done assuming all the lower states are filled and all the upper states are empty, a condition correct for intrinsic semiconductors at $0\ \mathrm{K}$. Using Heisenberg's uncertainty $\Delta x \Delta k_x = 2\pi$, the volume of uncertainty in momentum space is $\tau_k = 8\pi^3 / \tau_v$. Each τ_k may contain 2 electronic states as spin up and down, hence, the density of states in the volume element $d\tau_k$ is

$$dn_i = \frac{d\tau_{k_i}}{4\pi^3} \text{ and } dn_f = \frac{d\tau_{k_f}}{4\pi^3} \tag{A.25}$$

Using equations (A.21)-(A.25) gives out the absorption coefficient in terms of known parameters:

$$\alpha = \frac{e^2}{\pi^4 c m^2 n \omega} \int_{\tau_k} \left| \upsilon_{if} \right|^2 \delta\left(E_f\left(k_i\right) - E_i\left(k_i\right) - \hbar\omega \right) d\tau_{k_i} \tag{A.26}$$

A.5 Absorption in Direct Band Semiconductors

In direct band gap semiconductors phonon absorptions are not considered since the conduction band minimum is just over the valence band maximum (Fig. A.1). The momentum expectation value, to be altered by the radiation, is assumed to remain the same as $k_i = k_f = 0$ in this case. Therefore, υ_{if} of Eq. A.19 should be taken as constant with zeroth order approximation:

$$\upsilon_{if}\left(k_i\right) = \upsilon_{if}\left(0\right) + \frac{d\upsilon_{if}}{dk_i} k_i + \ldots \cong \upsilon_{if}\left(0\right) \tag{A.27}$$

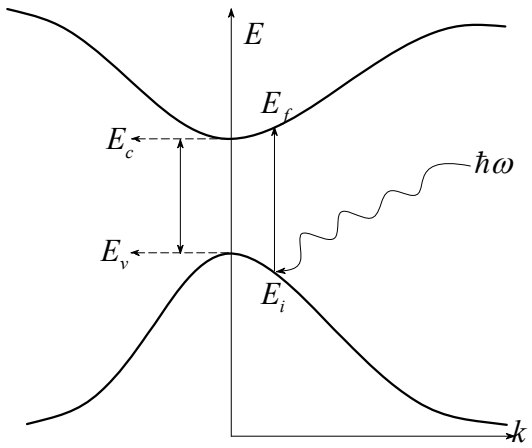

Figure A.1: Direct band gap semiconductor in which the extrema of valence and conduction bands have the same momentum.

The energy values of the initial and final states can be written from Fig. A.1 as

$$E_i\left(k_i\right)=E_v-\frac{\hbar^2k_i^2}{2m_h^*}$$
$$E_f\left(k_i\right)=E_c+\frac{\hbar^2k_i^2}{2m_e^*} \tag{A.28}$$

and the volume element is written by using the parabolic approximation at the edges of the bands as $d\tau_{k_i}=4\pi k_i^2dk_i$. Hence, Eq. A.26 for α becomes:

$$\alpha=\frac{e^2}{\pi^4cm^2n\omega}\int_{\tau_k}\left|\upsilon_{if}\left(0\right)\right|^2\delta\left(\hbar\omega-E_G-\frac{\hbar^2k_i^2}{2m_{red}^*}\right)4\pi k_i^2dk_i$$
$$=\frac{2e^2\left|\upsilon_{if}\left(0\right)\right|^2\left(2m_{red}^*\right)^{3/2}}{\pi^3cm^2n\hbar^2}\frac{\left(\hbar\omega-E_G\right)^{1/2}}{\hbar\omega} \tag{A.29}$$

If the absorption coefficient is obtained from optical transmission data, $(\alpha\hbar\omega)^2$ versus $\hbar\omega$ plot should give a straight line in the strong absorption region. The energy axis intercept of the linear fit of that straight line gives out the band gap energy of the semiconductor.

A.6 Absorption in Indirect Band Semiconductors

When the transition takes place with a change in the momentum as well as a change in the energy, a double step process is necessary since the photon momentum is not enough to change the momentum of an electron. Momentum is, instead, conserved via interaction with lattice vibrations (Fig. A.2). The quantum of lattice vibrations is called phonon. At room temperature, there is a broad spectrum of phonons. However, only the phonons with required momentum are usable. These phonons have characteristic energies represented by $E_{ph}=\hbar\omega_{ph}$, where ω_{ph} is the phonon vibration frequency. The transition might occur by either absorption or emission of a phonon:

$$\hbar\omega_a = E_f - E_i - E_{ph}$$
$$\hbar\omega_e = E_f - E_i + E_{ph} \tag{A.30}$$

A similar procedure with the case of direct transitions can be followed. The distinction in indirect transitions is that any occupied state of valence band can make a transition to any empty state of the conduction band. The density of states in the valence band at E_i is

$$N(E_i) = \frac{1}{2\pi^2\hbar^3}\left(2m_h^*\right)^{3/2}\left|E_i\right|^{1/2} \tag{A.31}$$

and the density of states in the conduction band at E_f is

$$N(E_f) = \frac{1}{2\pi^2\hbar^3}\left(2m_e^*\right)^{3/2}\left(E_f - E_G\right)^{1/2} \tag{A.32}$$

Using Eq. A.30, Eq. A.32 becomes

$$N(E_f) = \frac{1}{2\pi^2\hbar^3}\left(2m_e^*\right)^{3/2}\left(\hbar\omega - E_G \mp E_{ph} - E_i\right)^{1/2} \tag{A.33}$$

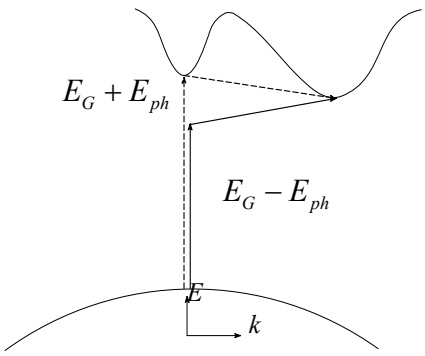

Figure A.2: Indirect band structure and the compensation of insufficiency of photon energy by phonons.

The absorption coefficient is proportional to the product of density of states integrated over all possible energy values separated by $\hbar\omega \pm E_{ph}$ and to the electron interaction probability with phonons, N_{ph}, which is the average number of phonons of energy E_{ph}, which is given by Bose-Einstein statistics:

$$N_{ph} = \frac{1}{e^{\frac{E_{ph}}{kT}} - 1} \tag{A.34}$$

Therefore, with A being a constant,

$$\alpha(\hbar\omega) = AN_{ph}\int_0^{-(\hbar\omega - E_G \mp E_p)} |E_i|^{1/2} \left(\hbar\omega - E_G \mp E_{ph} + E_i\right)^{1/2} dE_i \tag{A.35}$$

The integration together with Eq. A.34 gives out the absorption coefficient as

$$\alpha(\hbar\omega) = \frac{A\left(\hbar\omega - E_G \mp E_{ph}\right)^2}{e^{\frac{E_{ph}}{kT}} - 1} \tag{A.36}$$

For amorphous semiconductors absorption coefficient is related to the photon energy through the following formula[7]:

$$\alpha(\hbar\omega) = \frac{B\left(\hbar\omega - E_g\right)^2}{\hbar\omega} \tag{A.37}$$

The plot of $\sqrt{\alpha\hbar\omega}$ vs. $\hbar\omega$ should give a straight line in the strong absorption region. Extrapolation of this line reveals the optical gap of the semiconductor at the *energy-axis* intercept (Fig. 4.6).

Band gap energy reflects the energy required for band-to-band transitions. However, tail states are created as a result of the variations of bond angles and bond lengths.

Then, transitions from tail states to the band states or vice versa are also possible. In the photon energy region where tail-to-band transitions occur, absorption coefficient is an exponential function of energy [73]:

$$\alpha_{TB} = Ce^{-\frac{E_g - E}{E_o}} \tag{A.38}$$

where C is a constant depending on the material. E_o in Eq. A.38 is a disorder parameter called Urbach energy. It is almost zero for crystals and takes higher values as the material disorder increases. E_g is the band gap energy of a virtual crystal of perfect structure at 0 K. To find E_o, medium absorption region of the transmission data is used to plot $\ln\alpha$ vs. E.

APPENDIX B

BACKGROUND OF THIN SOLID FILM STRESS

B.1 Strain tensor for small deformations

Materials experience several alterations in their shape when they are exposed to some external forces. The relative change in the distances of the particles within a body in any direction with respect to its original form is called strain. These shape differences should occur in definite directions according to the directions and magnitudes of the applied forces. Therefore, strain concept takes the form of a tensor to overcome any misunderstanding in the type of deformation.

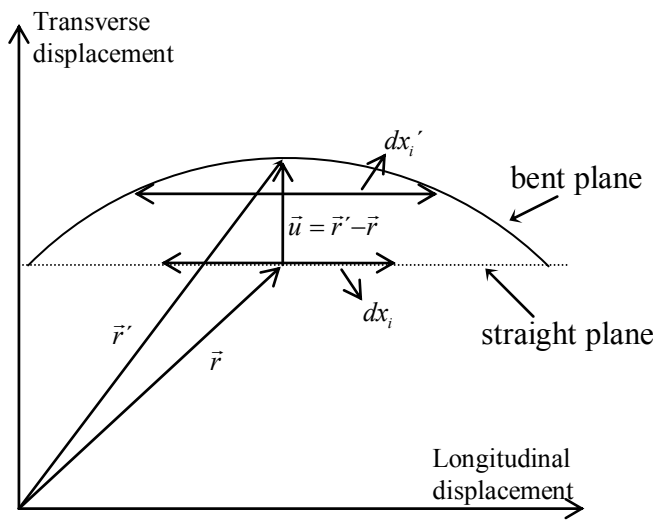

Figure B.1: Schematic of deformation and corresponding displacement vectors. Bent and straight planes represent the deformed and undeformed body, respectively.

Now, consider a point in a body which is deformed as seen in Fig. B.1. The change in its position vector is $u_i = x_i' - x_i$ and the differences in the position vectors between two points in the plane before and after the deformation are, respectively, dx_i and dx_i'. The coordinates x_i' is, of course a function of x_i, then u_i is also a function of x_i. Thus, if $\vec{u}(x_i)$ is obtained, the deformation of the body can be said to be fully determined. For this aim, let us write the infinitesimal lengths $|dx_i|$ and $|dx_i'|$ as $dl = \sqrt{dx_1^2 + dx_2^2 + dx_3^2}$ and $dl' = \sqrt{dx_1'^2 + dx_2'^2 + dx_3'^2}$, the squares of which are $dl^2 = dx_i^2$ and $dl'^2 = dx_i'^2 = (dx_i + du_i)^2$. Here, we should change du_i using its functionality of x_i as $du_i = (\partial u_i / \partial x_k) dx_k$. Hence; one can get closer to the strain tensor by writing:

$$dl'^2 = dl^2 + 2dx_i du_i + du_i^2 = dl^2 + 2(\partial u_i / \partial x_k) dx_i dx_k + (\partial u_i / \partial x_k)(\partial u_i / \partial x_l) dx_k dx_l$$

Interchanging necessary suffixes $(\partial u_i / \partial x_k) dx_i dx_k = (\partial u_k / \partial x_i) dx_i dx_k$ results in $dl'^2 = dl^2 + 2u_{ik} dx_i dx_k$ where the strain tensor u_{ik} for a deformed body is:

$$u_{ik} = \frac{1}{2}\left(\frac{\partial u_i}{\partial x_k} + \frac{\partial u_k}{\partial x_i} + \frac{\partial u_l}{\partial x_k}\frac{\partial u_l}{\partial x_i} \right) \text{ with } u_{ik} = u_{ki} \tag{B.1}$$

This symmetrical tensor may be diagonalized with principle values $u^{(1)}$, $u^{(2)}$ and $u^{(3)}$. In almost all cases, the strains are fairly small. That is, the distance change is small relative to the distance itself. On the other hand, the deformation vector u_i may be large in some cases. i.e. for a long thin rod, although the deformation is large especially at the ends, the extensions or compressions in the rod itself will be small. Except for special cases, it is assumed that a three-dimensional body cannot be intensively deformed unless it is highly extended or compressed. Therefore, the expression for the strain tensor (B.1) is reduced to, omitting the last term as being second order in smallness:

$$u_{ik} = \frac{1}{2}\left(\frac{\partial u_i}{\partial x_k} + \frac{\partial u_k}{\partial x_i}\right) \tag{B.2}$$

As the infinitesimal volume elements before and after the deformation (dV and dV') are the products $dx_1 dx_2 dx_3$ and $dx_1' dx_2' dx_3'$, respectively. Hence, $dV' = dV\left(1+u^{(1)}\right)\left(1+u^{(2)}\right)\left(1+u^{(3)}\right)$. Neglecting higher order terms for small deformations reveals $dV' = dV\left(1+u^{(1)}+u^{(2)}+u^{(3)}\right) = dV\left(1+u_{ii}\right)$. It is seen that the sum of diagonal components of strain tensor give the relative change in the volume,

$$\frac{dV' - dV}{dV} = \sum u^{(i)} \tag{B.3}$$

B.2 Stress tensor

All parts of a non-deformed body are in mechanical equilibrium; in other words, the resultant of the forces on any portion is zero. A deformation on this body, by changing the configuration of its molecules, put it out of thermal equilibrium. As a result, forces, which are called internal forces, arise to repel the body to equilibrium. These deformation induced internal forces are called internal stresses.

In the theory of elasticity, the microscopic forces causing the internal stresses are "near-action" forces which act from any point only to neighboring points; consequently the forces exerted on any portion of a body by surrounding parts act only to the surface of the portion.

To reach stress tensor, let us first consider a force $\vec{F}$ on the unit volume and $\vec{F}dV$ on the volume element dV of a body. Total force on the body is then, $\int \vec{F}dV$. The forces acting within the volume element of the body portion should cancel due to Newton's third law, leaving only the contributions from the surroundings of the

portion along its surface. Thus, the resultant force can be represented as the sum of all surface forces.

The 3 components $\int F_i dV$ of the total force may be represented in terms of a surface integral applying Green's theorem where the vector F_i must be the divergence of a tensor of rank two defined as $F_i = \sum_k \partial\sigma_{ik} / \partial x_k$. Then, the force on any volume can be formulated as an integral over a closed surface bounding that volume:

$$\int_V F_i dV = \oint_S \sigma_{ik} df_k \tag{B.4}$$

where df_k is the components of surface element vector $\vec{df}$ and σ_{ik} is the stress tensor. The directional correspondence of the stress tensor is shown in Fig. B.2. The above expression (B.4) is the force exerted on the volume V of surface(s), by the surrounding parts of the body. The force exerted by this volume on the surrounding surface is equal and opposite.

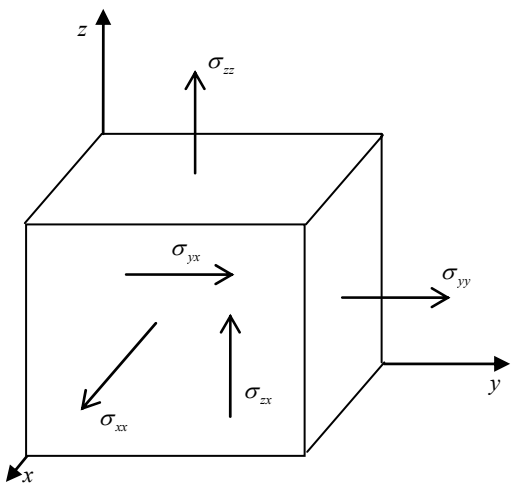

Figure B.2: Tensor of rank two is necessary to completely describe the stress of a body. Each direction having three stress components, stress tensor forms a 3×3 matrix.

The moment of the forces on a portion of the body, which might lead a sample to gain a curvature can be found considering the cross product of force and the arm length $\vec{F} \times \vec{r} = F_i x_k - F_k x_i$ and integrating over the whole volume,

$$M_{ik} = \int \left(F_i x_k - F_k x_i \right) dV = \int \left(\frac{\partial \sigma_{il}}{\partial x_l} x_k - \frac{\partial \sigma_{lk}}{\partial x_l} x_i \right) dV \tag{B.5}$$

which can be separated as:

$$\begin{aligned} M_{ik} &= \int \frac{\partial \left(\sigma_{il} x_k - \sigma_{kl} x_i \right)}{\partial x_l} dV - \int \left(\sigma_{il} \frac{\partial x_k}{\partial x_l} - \sigma_{kl} \frac{\partial x_i}{\partial x_l} \right) dV \\ &= \oint \left(\sigma_{il} x_k - \sigma_{kl} x_i \right) df_l - \int \left(\sigma_{ik} - \sigma_{ki} \right) dV \end{aligned} \tag{B.6}$$

If M_{ik} is to be an integral over surface only, the second term should be identically zero and then within the body leading to the symmetry of the stress tensor $\sigma_{ik} = \sigma_{ki}$. Thus,

$$M_{ik} = \oint \left(\sigma_{il} x_k - \sigma_{kl} x_i \right) df_l \tag{B.7}$$

B.3 Thermodynamics of deformation

The internal stress does a work δR per unit volume when the displacement vector u_i of a deformed body changes by a small amount δu_i, where $\delta R = F_i \delta u_i = \left(\partial \sigma_{ik} / \partial x_k \right) \delta u_i$. Then, total work done over the whole volume is

$$\int \delta R dV = \int \left(\frac{\partial \sigma_{ik}}{\partial x_k} \right) \delta u_i dV = \oint_S \sigma_{ik} \delta u_i df_k - \int_V \sigma_{ik} \left(\frac{\partial \delta u_i}{\partial x_k} \right) dV \tag{B.8}$$

If an infinite medium is considered where the surface integration tends to infinity unless $\sigma_{ik} = 0$, the first integral should be equal to zero. The symmetry of the tensor u_{ik} leads to;

$$\int \delta R dV = -\frac{1}{2}\int_V \sigma_{ik}\left(\frac{\partial \delta u_i}{\partial x_k} + \frac{\partial \delta u_k}{\partial x_i}\right) dV = -\frac{1}{2}\int \sigma_{ik}\delta\left(\frac{\partial u_i}{\partial x_k} + \frac{\partial u_k}{\partial x_i}\right) dV = \int \sigma_{ik}\delta u_{ik} dV$$

$$\Rightarrow \delta R = -\sigma_{ik}\delta u_{ik} \tag{B.9}$$

which gives the work in terms of the change in strain tensor.

For fairly small deformations, the body returns to its original undeformed state when the external forces causing the deformation are removed. Such deformations are called elastic. On the other hand, in the case of relatively intensive deformations the return to undeformed state does not occur, leaving a residual deformation. Such deformations are called plastic.

Practically, the process of deformation may be assumed thermodynamically reversible and first law of thermodynamics states that an infinitesimal change $d\xi$ in the internal energy ξ equals to the difference between the work done by the system (here by the internal stresses) and the amount of heat $dQ = TdS$ (with $S = entropy$) received by the system from the surrounding:

$$d\xi = TdS - dR = TdS + \sigma_{ik} du_{ik} \tag{B.10}$$

which is the thermodynamical relation for a deformed body.

Introducing Helmholtz Free Energy, $F = \xi - TS$, dF may be expressed by using (B.10) as:

$$dF = -SdT + \sigma_{ik} du_{ik} \tag{B.11}$$

The components of the stress tensor can be obtained by differentiating F or ξ with respect to the components of the strain tensor for constant T or S, respectively [77]:

$$\sigma_{ik} = \left(\frac{\partial F}{\partial u_{ik}} \right)_T = \left(\frac{\partial \xi}{\partial u_{ik}} \right)_S \tag{B.12}$$

B.4 Hooke's Law

To obtain the stress of any physical system, it is necessary to relate stress to strain which is directly measurable. This is possible if the free energy of the body is known as a function of the strain tensor, which can be easily obtained by the expansion of free energy in powers of u_{ik} in what follows.

Let us now consider a system of constant temperature to exclude any effect caused by thermal expansion. For the simplest case, the undeformed body where $u_{ik} = 0$ experiences no external force, thus having $\sigma_{ik} = 0$. To satisfy this condition in $\sigma_{ik} = \left(\partial F / \partial u_{ik} \right)_T$ free energy should contain no linear term in the power expansion of u_{ik}. Therefore, free energy should be second order in strain tensor to keep only the first non-vanishing power accounting for the smallness of the deformation. Since two independent scalars of u_{ik} in second degree can be formed, free energy should contain them both with corresponding scalar constants, giving the general expression for the free energy of a deformed body,

$$F = \frac{1}{2} \lambda u_{ii}{}^2 + \mu u_{ik}{}^2 \tag{B.13}$$

here, λ and μ are Lamé coefficients.

It is known that the sum of diagonal components of strain tensor, u_{ii} gives the change in the volume caused by deformation. If this sum is zero, the volume of the

body means to be unchanged. Such deformations are called pure shear. On the contrary, the volume of the body may change while its shape is constant, where only the diagonal terms of strain tensor should survive, $u_{ik} = constant \times \delta_{ik}$. Such deformations are called hydrostatic compression. Being two independent scalars, the sum of a pure shear and a hydrostatic compression is enough to define the deformation by the help of the identity:

$$u_{ik} = \left(u_{ik} - \frac{1}{3}\delta_{ik}u_{ll} \right) + \frac{1}{3}\delta_{ik}u_{ll} \tag{B.14}$$

Since $\delta_{ik} = 3$, first term in parenthesis is a pure shear having no diagonal component and second term is a hydrostatic compression having only the diagonal terms. Hence, free energy (B.13) can also be expressed by the sum of the second degrees of a pure shear and a hydrostatic compression as,

$$F = \mu\left(u_{ik} - \frac{1}{3}\delta_{ik}u_{ll} \right)^2 + \frac{1}{2}Ku_{ll}{}^2 \tag{B.15}$$

where K and μ are the modulus of hydrostatic compression and modulus of rigidity, respectively. By a simple calculation it can be found that,

$$K = \lambda + (2/3)\mu \tag{B.16}$$

The thermodynamic equilibrium of a deformed body can be reached if the deformation is removed relaxing the system and increasing its entropy, S. If no external forces are present in the system, the body will return to its thermodynamic equilibrium, thus, $u_{ik} = 0$. Decreasing u_{ik} decreases the modulus of the free energy. Therefore, the quadratic form for the free energy should be positive to reach its minimum when u_{ik} is zero. A necessary and sufficient condition is that moduli of hydrostatic compression and rigidity be positive;

$$K > 0 \text{ and } \mu > 0 \tag{B.17}$$

Free energy is now obtained as a function of strain tensor which allows us to determine stress tensor by the relation (B.12). To calculate this derivative, let us first write the total differential dF for constant temperature,

$$dF = Ku_{ll}du_{ll} + 2\mu\left(u_{ik} - \frac{1}{3}\delta_{ik}u_{ll}\right)d\left(u_{ik} - \frac{1}{3}\delta_{ik}u_{ll}\right) \tag{B.18}$$

The second term gives zero when the parenthesis is multiplied by δ_{ik}. Moreover, as du_{ll} can be written as $du_{ik}\delta_{ik}$, the total differential of free energy becomes,

$$dF = \left[Ku_{ll}\delta_{ik} + 2\mu\left(u_{ik} - \frac{1}{3}\delta_{ik}u_{ll}\right)\right]du_{ik} \tag{B.19}$$

Stress tensor is, then written as,

$$\sigma_{ik} = Ku_{ll}\delta_{ik} + 2\mu\left(u_{ik} - \frac{1}{3}\delta_{ik}u_{ll}\right) \tag{B.20}$$

This expression, finally, gives the stress tensor as a function of strain tensor. Note that, if the deformation is one of pure shear or hydrostatic compression, stress is directly proportional only to the corresponding deformation with the proportionality constants μ and K, respectively.

The converse formula for the strain tensor in terms of stress tensor may be easily obtained. The sum of the diagonal terms of stress tensor is $u_{ii} = \sigma_{ii}/3K$. Then,

$$\sigma_{ik} = K\frac{\sigma_{ll}}{3K}\delta_{ik} + 2\mu\left(u_{ik} - \frac{1}{3}\delta_{ik}\frac{\sigma_{ll}}{3K}\right) \tag{B.21}$$

and solving for u_{ik} reveals,

$$u_{ik} = \frac{1}{9K}\delta_{ik}\sigma_{ll} + \frac{1}{2\mu}\left(\sigma_{ik} - \frac{1}{3}\delta_{ik}\sigma_{ll}\right) \tag{B.22}$$

It is seen by this formula that the deformation is linearly proportional to the applied forces. This law, applicable for small deformations, is called Hooke's Law.

B.5 Homogeneous Deformations

The simple case such that the strain tensor u_{ik} is constant within the volume of the body is called homogeneous deformation, i.e. hydrostatic compression. To analyze this type of deformation, first consider the extension of the rod in Fig. B.3. The pulling force $\vec{p}$ per unit area is applied along the symmetry axis of the rod from each end.

The external forces acting on the surface of the body are the general sources of deformation. Thus, they should be involved in the boundary conditions of equations of equilibrium. If $\vec{P}$ is the external force per unit area, $\vec{P}df$ is the force on the surface element df. Consequently, this force is to be balanced by the forces $-\sigma_{ik}df_k$ of the stresses on that element, that is, $P_i df - \sigma_{ik}df_k = 0$. If $\hat{n}$ is the outward normal unit vector, it is found that,

$$\sigma_{ik}n_k = P_i \tag{B.23}$$

For the rod in Fig. B.3, no force is acted on the sides, $\sigma_{ik}n_k = 0$. Using the fact that σ_{ik} is constant within the volume and that it is a symmetric tensor, only σ_{zz} component survives,

$$\sigma_{zz} = p \tag{B.24}$$

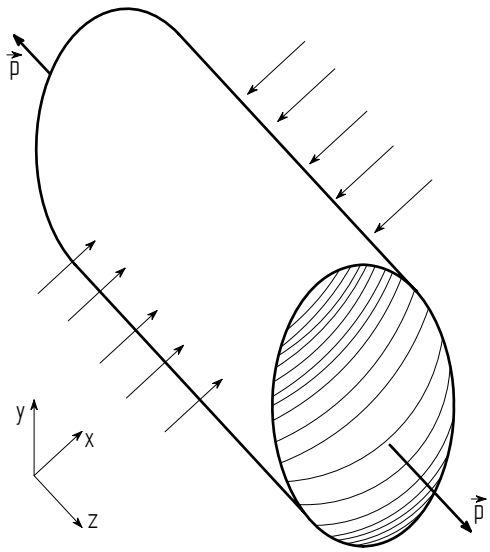

Figure B.3: Force per unit area $\pm\vec{p}$ stretches the rod longitudinally and squeezing occurs in the transverse components.

Now, the components of the strain tensor can be written in terms of σ_{zz}, using (B.22):

$$u_{xx} = u_{yy} = \left(\frac{1}{9K} - \frac{1}{6\mu}\right)p \tag{B.25}$$

$$u_{zz} = \left(\frac{1}{9K} + \frac{1}{3\mu}\right)p \tag{B.26}$$

where u_{zz} gives the relative lengthening of the rod and the coefficient of p is the coefficient of extension whose reciprocal is called Young's Modulus, E,

$$u_{zz} = p/E \tag{B.27}$$

and

$$E = \frac{9K\mu}{3K + \mu} \tag{B.28}$$

where as u_{xx} and u_{yy} gives the relative compression in the transverse direction. The ratio of transverse compression to the longitudinal extension is called Poisson's ratio, ν_S,

$$u_{xx} = -\nu_S u_{zz} \tag{B.29}$$

with,

$$\nu_S = \frac{1}{2}\left(\frac{3K - 2\mu}{3K + \mu}\right) \tag{B.30}$$

Poisson's ratio should vary between *-1* $(K = 0)$ and *1/2* $(\mu = 0)$ due to the condition (B.17),

$$-1 \le \nu_S \le \frac{1}{2} \tag{B.31}$$

However, in practice ν_S vary only between 0 and *1/2* because materials known do not expand transversely when stretched longitudinally. It should also be mentioned here that the values of ν_S close to *1/2* infer higher modulus of compression compared to the modulus of rigidity.

Stretching the rod changes its volume relatively by,

$$u_{ii} = p/3K \tag{B.32}$$

in which only the modulus of compression is involved.

To obtain the free energy of a stretched rod, which would be helpful to obtain Hooke's relations (B.22) for generalized homogeneous deformations may be obtained as follows. It is known that the free energy is second power in u_{ik}, then, Euler's theory can be used,

$$F = \frac{1}{2} u_{ik} \frac{\partial F}{\partial u_{ik}} \tag{B.33}$$

Since only the σ_{zz} component exists in this case, $F = (1/2)\sigma_{zz} u_{zz}$,

$$F = \frac{p^2}{2E} \tag{B.34}$$

The quadratic equation for the free energy in terms of strain tensor is commonly used not with the constants μ and K, but with E and ν_S. Thus, the modulus of rigidity and modulus of compression should be, by a simple calculation, expressed in terms of Young's modulus and Poisson's ratio as

$$\mu = \frac{E}{2(1+\nu_S)} \text{ and } K = \frac{E}{3(1-2\nu_S)} \tag{B.35}$$

Free energy, then, takes the form,

$$F = \frac{E}{2(1+\nu_S)} \left(u_{ik}{}^2 + \frac{\nu_S}{1-2\nu_S} u_{ll}{}^2 \right) \tag{B.36}$$

whose derivative with respect to u_{ik} gives the stress tensor in terms of strain tensor for a general homogeneous deformation,

$$\sigma_{ik} = \frac{E}{1+\nu_S} \left(u_{ik} + \frac{\nu_S}{1-2\nu_S} u_{ll} \delta_{ik} \right) \tag{B.37}$$

The strain tensor in terms of stress tensor can be found by using $u_{ii} = \sigma_{ii}/3K$ and substituting into the above equation to solve for u_{ik};

$$u_{ik} = \frac{1}{E} \left\{ (1+\nu_S)\sigma_{ik} - \nu_S \delta_{ik} \sigma_{ll} \right\} \tag{B.38}$$

Let us now consider a thick plane to be deformed by an external force along the z direction. If the deformation is very small along the x and y directions, the deformation can be said to be only along the z axis. Then, only u_{zz} component of the strain tensor is different than zero. Such a deformation is called unilateral deformation, which, in what follows, reveals the transverse stresses σ_{xx} and σ_{yy} as biaxial stresses. Again, $\sigma_{zz} = p$, this time gives the results;

$$\begin{aligned} \sigma_{xx} = \sigma_{yy} &= \frac{E}{(1+\nu_S)(1-2\nu_S)} u_{zz} \\ \sigma_{zz} = p &= \frac{E(1-\nu_S)}{(1+\nu_S)(1-2\nu_S)} u_{zz} \end{aligned} \tag{B.39}$$

The transverse stress components σ_{xx} and σ_{yy} can be written in terms of the longitudinal stress σ_{zz} , that is the applied force per unit area, as

$$\sigma_{xx} = \sigma_{yy} = \frac{p}{(1 - \nu_S)} \tag{B.40}$$

which is a useful relation for the consideration of unilateral deformation caused by biaxial stresses σ_{xx} and σ_{yy} .

The free energy of unilateral deformation may also be written here,

$$F = \frac{p^2 (1+\nu_S)(1-2\nu_S)}{2E(1-\nu_S)} \tag{B.41}$$